2016

Numerical Simulations of Wind Effects on Wave Nonlinearity and Hurricane-Induced Sediment Transport on Louisiana Coast

Ke Liu
Louisiana State University and Agricultural and Mechanical College

NUMERICAL SIMULATIONS OF WIND EFFECTS ON WAVE NONLINEARITY AND HURRICANE-INDUCED SEDIMENT TRANSPORT ON LOUISIANA COAST

A Dissertation

Submitted to the Graduate Faculty of the
Louisiana State University and
Agricultural and Mechanical College
in partial fulfillment of the
requirements for the degree of
Doctor of Philosophy
in

The Interdepartmental Program in
Engineering Science

by
Ke Liu
B.Eng., Sichuan University, 2008
August 2016

ACKNOWLEDGMENTS

First of all, I would like to express my sincere appreciation to my major professor, Dr. Qin J. Chen, for his aspiring guidance and support throughout my Ph.D. study. I thank Dr. Haosheng Huang, Dr. Xiaoliang Wan, and Dr. Kehui Xu for serving on my dissertation committee and providing valuable advice. I thank Dr. Luis Escobar for serving as Deans representative for my general and final exams. My dissertation research benefits greatly from discussions with Dr. Kelin Hu on numerical modeling. Dr. Eugene Turners provided us with his measurement data for sediment deposition after Hurricane Gustav. Dr. Robert Twilley also gave me many constructive suggestions for my modeling research.

I would like to acknowledge Dr. Hongqing Wang and Brady Covillion of USGS who provided the vegetation distribution data and shared a lot of valuable knowledge on wetland ecology. I also want to thank Dr. Lixia Wang, Dr. Chunyan Li and Dr. Justic Dubravko for providing the DEM and LIDAR data in Barataria Bay and Terrebonne Bay. My studies at LSU were supported by the LSU Economic Development Assistantship, Sea Grant, and National Science Foundation (SEES-1427389).

I thank Dr. Arash Karimpour, Dr. Jian Tao, Dr. Haihong Zhao, Dr. Ranjit Jadhav, who gave me much help in my study and research. I am grateful to my friends and colleagues Ling Zhu, Agnimitro Chakrabarti, Cody Johnson, Thomas Everett, and Guoji Xu, who shared with me their knowledge and have been very supportive.

Last but not least, I am grateful to my grandparents, my parents, and everyone in my big family for their love through my study. Special thanks to Dianhuan for bearing with me when I was devoted to fulfilling my determination.

Whatever I accomplished here, “is not the end. It is not even the beginning of the end. But it is the end of the beginning”.

TABLE OF CONTENTS

ABSTRACT

The objective of this study is to model wind effects on wave nonlinearity and the sediment suspension, transport and redistribution caused by hurricanes. The following questions are addressed through numerical simulations: (1) How do winds affect wave triad interactions and wave shape in the shallow water? (2) What is the role of hurricanes in coastal landscape evolution? Do they create more erosion or deposition? (3) Where does the observed post-hurricane deposition on coastal wetlands come from?

First, wind effects were incorporated into a Boussinesq-type wave model, and evolution equations were derived for triad interactions with winds. Second, a coupled modeling system for hurricane waves, storm surge, and sediment transport was developed for the Louisiana coast. Third, the modeling system was extended to three dimensions (3D), and the impact of barrier islands on hurricane-induced sediment redistribution was evaluated using the 3D model.

The Boussinesq model and the evolution equations together illustrated why following (opposing) winds can enhance (suppress) triad interactions and how the wave shape varies due to the nonlinear wave-wave interactions. The process-based modeling system for coastal Louisiana demonstrated that a major hurricane event has the ability to deliver a considerable amount of sediment to the coastal wetlands, and estimated that Hurricane Gustav (2008) delivered 25.6 million metric tons of sediment to the wetlands in the Terrebonne and Barataria Basins, and most of the observed sediment accretion (97.3% for Terrebonne and 99.8% for Barataria) came from the estuaries. The net deposition on wetlands was 21% smaller in the 3D model than the results from the 2D model using the same sediment properties, while the finding that the hurricane-induced deposition came from erosion in the coastal bays held true regardless of the dimensionality of the model. The deterioration of barrier islands affected the maximum surge level, wave heights and sediment transport in the protected estuaries, but the net effect on sediment fluxes from the continental shelf to the bays and from the bays to wetlands varied by

location. Numerical experiments suggested that the contribution from marine sediment to wetland deposition would still be very small even when the barrier islands were severely degraded.

CHAPTER 1 INTRODUCTION

1.1 Background

1.1.1 A crisis of land loss

Over the last two hundred years, twenty-two states in the United States have lost 50% of their original wetlands, among which Louisiana has the highest rate (Mitsch and Gosselink, 1993). Although wetland building and deterioration have been naturally occurring in southeast Louisiana as the Mississippi River switched from one delta lobe to another for thousands of years, in the last century, the wetland erosion became much faster than the natural building process and could not be balanced anymore.

The coastal wetlands in Louisiana are fragile and valuable natural resources to the state and the nation. Wetlands protect the coastal community by buffering the storm surge and waves during hurricanes and storms. According to Costanza et al. (1989), if Terrebonne wetlands receded by one mile, the expected property loss due to storm and wind damage in a four-parish area would increase by $5,752,816 annually. Louisiana's fishery industry produces 25% of all the seafood in America and contributes over three billion dollars each year to the state's economy. If the wetlands disappear, so will the fishery. The wetland ecosystem also provides a good habitat to many birds and marine animals including some rare and endangered species, such as the bald eagle and the brown pelican. In addition, 80% of the nation's offshore oil and gas is produced off the Louisiana coast. The related business and job opportunities all depend on a healthy and sustainable wetland system in the coastal zone.

The increased human activities sped up wetland erosion and broke the natural balance between land building and erosion on the Louisiana coast. The upstream dams on the Mississippi River and its tributaries decreased sediment load in the river, and the levee system along the river channel further prevented the coastal wetlands from receiving riverine water, nutrients and

sediment that are critical to coastal wetland survival (Kesel, 1988, 1989; Kesel et al., 1992; Mossa, 1996).

The current rate of land loss in Louisiana varies in different areas, from 64 acres per year in the Atchafalaya Basin to 7,104 acres per year in the Barataria Basin (Couvillion et al., 2011). If the land loss continues at the current rate, Louisiana will have lost more than one million acres of wetlands, an area larger than the state of Rhode Island, by the year 2040.

1.1.2 A history of frequent hurricanes and storms

Louisiana is one of the states with the most frequent hurricanes in America, only behind Florida and Texas, according to the National Hurricane center (available at: `http://www.nhc.noaa.gov/paststate.shtml`). On average, since 1851, a tropical storm or hurricane is expected to strike Louisiana's coast about once a year with a hurricane possible once every three years (Roth, 2010). Several well-known hurricanes in Louisiana include Audrey (1957), Besty (1965), and Katrina (2005). Audrey (1957), a Category 4 hurricane with winds up to 150 mph, came ashore with a 12 ft storm surge topped by 20 ft waves, and it destroyed the town of Cameron. Besty (1965) flooded the city of New Orleans and claimed 58 lives in Louisiana. Katrina (2005) was the most expensive natural disaster in America of all time. The property damage was estimated to be at least 108 billion dollars in addition to the human cost of 1836 lives lost and over one million people displaced.

1.1.3 A debate on the role of hurricanes in the evolution of coastal landscapes

The question whether an extreme event like a hurricane or storm causes sediment deposition or erosion on coastal wetlands has been discussed since a half century ago. In one of the pioneering studies, Morgan et al. (1958) reported large masses of clay deposited on beaches as mud arcs after Hurricane Audrey (1957). Chamberlain (1959) also found a widely distributed deposition in the marsh region in Southeast Louisiana after Audrey, and suggested that the de-

posited sediment might originate from bottom materials suspended in shallow lakes or from subsurface layers beneath stands of vegetation.

Stumpf (1983) studied sediment deposition at the Holland Glade Marsh near Lewes, Delaware, and analyzed the relation between observed sedimentation and water flow on the marsh surface. The data showed that if all the sediment lost from the water flowing over the levee was deposited on the surface of the marsh, normal tides could not provide enough sediment to maintain the accretion of marsh surface. A 2 to 5 mm mud layer observed on the back marsh also indicated the dominance of storm deposition over normal deposition. Rejmanek et al. (1988) used feldspar clay marker horizons to measure sediment accumulation in four marsh communities near Atchafalaya Bay. The author found that Hurricane Danny in mid-August 1985 brought more than 2 cm of material in that area. Reed (1989) evaluated the relative contribution to marsh sedimentation of each flooding event from 1985 to 1986 in Terrebonne Bay, and the results indicated a strong association between the increase of sediment deposition on the marsh and the passage of winter cold fronts.

After Hurricane Andrew in 1992, Nyman et al. (1995) found a significant deposition four to eleven times as thick as the annual accretion rate at twelve sites in the Mississippi Delta Plain. An analysis of sediment composition, bulk density, sand percentage and texture revealed that the deposition was most likely from the bottom of the local bay rather than from the Gulf of Mexico or marsh soil. Also for Hurricane Andrew, Cahoon et al. (1995) studied both short-term and long-term effects of the hurricane on sedimentation and erosion on Louisiana coastal marshes. Sediment traps were used to record bi-week deposition, and feldspar marker horizons were deployed to measure the change in the marsh elevation at Terrebonne Bay, Barataria Bay and the Pontchartrain basin over two years. The authors found that the short-term deposition rate increased significantly during the passage of Hurricane Andrew, and the area of influence reached as far as the south shore of Lake Pontchartrain, although the hurricane made landfall

at Atchafalaya Bay. The sedimentation rate remained at a high level until the first winter cold front arrived three months later.

Turner et al. (2006) measured the sediment accumulation after Hurricanes Katrina and Rita passed through the Louisiana coast in 2005. Sediment samples were collected from 198 locations from all coastal watersheds in Louisiana and seven sites in east Texas, and sediment deposition and density were measured at each site. Calculating the total amount of newly deposited sediment on the tidal marsh using average sediment accretion and wetland area, Turner et al. (2006) estimated that the minimum amount of inorganic sediment brought in by these two hurricanes was 131 Million Metric Tons (MMT), which was the first quantitative estimate of the total deposition on Louisianas coastal wetlands caused by a major hurricane event. As an extension of this study, Tweel and Turner (2012) measured and analyzed sediment deposition following Hurricane Katrina (2005), Rita (2005), Gustav (2008) and Ike (2008). The estimated total deposition was 68, 48 and 21 MMT for Hurricane Katrina, Rita and Gustav, respectively. Based on a statistical model, Tweel and Turner (2014) further estimated that the annual deposition on the marsh surface on Louisiana coast from category 1 or higher hurricanes was 5.6 MMT.

The above-mentioned studies seem to all lead to a conclusion that hurricanes and storms have the ability to bring sediment to the coastal wetlands. On the other hand, however, hurricanes and storms have been widely recognized as an erosional forcing and evidence for hurricane-related erosion was also reported in the literature (Ritchie and Penland, 1988; Morton and Sallenger Jr, 2003; Sallenger Jr, 2000; Houser et al., 2008; Wang et al., 2006). Since in this dissertation we are mainly concerned about the large-scale sediment balance rather than local morphological changes or detailed erosion patterns, such as beach erosion and washover deposition, the following literature review briefly covers the evidence for large-scale marsh erosion and land loss due to hurricanes.

The elevation change of marsh surface in response to storm events provides direct evidence for marsh erosion, and storm-induced erosion has been studied by measuring the change of marsh surface elevation (Cahoon et al., 1998, 1999; Cahoon, 2003). Via lithostratigraphy analysis, van de Plassche et al. (2006) also found that hurricane activity caused marsh erosion in southern New England. Louisiana is rich in hurricane history and data archives. Morton and Barras (2011) examined a 60-year record of aerial photographs and a 30-year record of satellite images together with field observations, and identified major storm-generated morphological features in southern Louisiana. According to Morton and Barras (2011), many erosional and deformational features caused by storms and hurricanes could be found in the Mississippi Delta. Among them were orthogonal-elongate ponds, amorphous pond, pond expansion, and so on, in the order of decreasing severity. Another group of features involved the destruction of vegetation and marsh mat. Hurricanes could strip aboveground vegetation with only plant stubble and roots left, and convert a densely vegetated wetland into a mud flat. Marsh compression occurred as marsh mats were folded and formed ridges and troughs. Many marsh compressions and displacements were observed near adjacent open water bodies, indicating the importance of water bodies in marsh erosions.

As we can imagine, there might be no simple "Yes" or "No" answer to whether the net effect of a hurricane is deposition or erosion on coastal wetlands. It is more likely that multiple processes happen simultaneously or in a certain order and the net effect depends on the relative strength of erosion and deposition. For instance, the suspended sediment could be transported and settle down at another location, and the local erosion might be filled in by deposited material very quickly. Furthermore, the existence of vegetation and the small ponds and lakes on wetlands further complicate the situation.

1.2 Problem Statement

So far, most of our knowledge on the influence of hurricane on sediment dynamics along the Louisiana coast and its impact on the coastal wetlands is based upon field measurements. We still lack a quantitative understanding of large-scale sediment transport under hurricane conditions. The ongoing efforts to protect the valuable coastal resource and restore the coastal wetlands also highlight the need for a process-based, comprehensive numerical model for hurricane-induced sediment transport to guide engineering practices.

In this dissertation, we will demystify the role of a hurricane in sediment transport, especially in the sediment balance of coastal wetlands on Louisiana coast through numerical simulations. As an accurate prediction of storm surge, current, and waves is a prerequisite for modeling the hurricane-induced sediment suspension and redistribution, we will address this problem from both the hydrodynamic and the sedimentary perspective through multi-scale modeling. In the laboratory scale, we will study the wind effects on wave nonlinearity, including the triad interactions and wave skewness and asymmetry, in shallow water. This is important not only for wave energy distribution in the coastal area but also for onshore sediment transport. In the regional scale, we will develop an integrated modeling system for storm surge, waves and sediment transport using Delft3D and apply it to simulate hurricane-induced sediment transport.

With this modeling system, we will be able to answer some basic but important scientific questions, such as (1) What are the effects of hurricanes in coastal landscape evolution? Do they create more erosion or deposition? (2) Where does the observed deposition come from? In addition, our simulations will shed light on the large-scale sediment dynamics in the inner shelf-bay-wetland system during hurricanes and storms, and improve our understanding of the natural sediment redistribution process, which is important for the sediment balance of the receding wetland. And hopefully, we can provide some useful hints for the planning and design of coastal restoration projects.

1.3 Hypotheses and Research Questions

In this study, we will test some long-existing hypotheses using the numerical model:

1) The strong hydrodynamic forcing during a hurricane is able to cause a significant amount of deposition on coastal wetlands;

2) The deposition on wetlands mainly originates from the open shallow bays;

3) The deterioration of barrier islands could enhance the sediment transport from the continental shelf to the coastal wetlands.

The following research questions will be addressed in this study: (1) Does wind enhance or suppress triad interactions among different wave harmonics in shallow water? How does wind affect wave shape in the shoaling process? (2) How do hurricane waves propagate from offshore deep water to nearshore shallow water and attenuate over vegetated wetland? (3) How can we effectively model storm surge reduction due to vegetation in a large-scale simulation while eliminating the side effects on sediment transport modeling? How well can a model predict the surge level at inland marshes? (4) What accuracy can a depth-averaged sediment transport model achieve in terms of morphological change after hurricanes? (5) How do we use the model to identify the source of sediment deposited on wetlands in the model? (6) Do different formulations in the 2D and 3D models affect the prediction of sediment suspension and deposition? (7) How do barrier islands affect hurricane-induced sediment transport?

1.4 Objectives and Outline

In order to answer the above questions, the following objectives are formulated:

1) Model wind effects in a Boussinesq wave model, and compare the wave nonlinearity under different wind speeds and directions;

2) Simulate hurricane hydrodynamics with storm surge and wave models running in a fully coupled manner;

3) Validate the hydrodynamic model by comparing predicted storm surge and waves with observation data;

4) Couple a sediment transport model with the hydrodynamic model and validate the model with the observed post-hurricane deposition on wetlands;

5) Apply the coupled storm surge, wave and sediment transport modeling system to estimate the net deposition/erosion on coastal wetlands during a hurricane event and analyze the source of possible deposition on wetlands;

6) Extend the coupled modeling system into a three dimensional one and compare the consequences of model formulation (2D depth-averaged versus 3D) with all the parameters for major physical processes kept the same;

7) Investigate the impact of deterioration of barrier islands on coastal wetland sedimentation and hurricane-induced sediment fluxes in the shelf-bay-wetland system using the 3D modeling system.

In Chapter 2, the evolution equations for the first three wave harmonics are derived for an ideal flat bottom scenario. In addition, a representation of wind is implemented in a Boussinesq-type wave model. Then wind effects on wave nonlinearity are studied using a combination of evolution equations and the numerical model.

In Chapter 3, a fully-coupled hydrodynamic model for storm surge and waves is developed using Delft3D. The wave model is validated through the comparison of model results with the observations of wave heights, periods and directions at offshore wave buoys. The storm surge model and the coupling of surge and wave models are validated by comparing the modeled storm surge level and nearshore waves with observations at a number of stations along the Louisiana coast.

In Chapter 4, a sediment transport model is coupled with the hydrodynamic model. The coupled modeling system is validated using the observed sediment accretion on wetlands after

Hurricane Gustav (2008), and then applied to evaluate the sediment fluxes in the inner shelf-estuary-wetland system and predict the deposition/erosion on coastal wetlands.

In Chapter 5, the depth-averaged modeling system is extended into three dimensions. The 3D model is calibrated so that it can achieve similar accuracy for storm surge and wave predictions. Then the modeled sediment transport during Gustav from Chapter 4 is re-verified using the 3D model. The effect of the possible deterioration of barrier islands is also evaluated.

Finally, all the findings and conclusions are summarized in Chapter 6.

CHAPTER 2 MODELING WIND EFFECTS ON SHALLOW WATER WAVES [1]

2.1 Introduction

As ocean waves propagate from deep to shallow water, nonlinear interactions generate high harmonics and sub-harmonics of the primary wave frequency, and energy can be transferred across the spectrum over a relatively short distance. Triad interactions, namely the interactions between the primary wave and two high harmonics, take place as long as near resonant conditions are satisfied in shallow water. Triad interactions have long been noticed in practice. Hansen and Svendsen (1974) showed that in shallow and intermediate water depth, the waves generated by a sinusoidal-motion piston wave maker can be decomposed into a second-order Stokes wave and a free second harmonic wave. In terms of energy dissipation in shallow water, Battjes and Beji (1992) suggested that wave-wave nonlinear interactions are responsible for spectrum evolution, while wave breaking only extracts energy approximately in proportion to the local spectral density. Later, Eldeberky and Battjes (1995) derived a parameterization to represent the average effect of triad interactions for phase-averaged wave model based on observation data. Field data reported by Boczar-Karakiewicz et al. (1986) and Boczar-Karakiewicz and Davidson-Arnott (1987) also indicated a possible association between nonlinear interactions and the formation of longshore sand bar in Lake Huron. Triad interactions for regular waves have also been studied analytically. Evolution equations, which express the variation of amplitude and phase of each harmonic, can be obtained on the basis of Boussinesq or KdV equations (Mei and Unluata, 1972; Bryant, 1973; Madsen and Sørensen, 1993; Dingemans, 1997). Freilich and Guza (1984), Elgar et al. (1990) and Kaihatu (2009) further investigated the evolution of wave spectra in wave shoaling.

[1] This chapter has appeared in "Journal of Waterway, Port, Coastal, and Ocean Engineering". Liu, K., Chen, Q., and Kaihatu, J. M. (2015). Modeling Wind Effects on Shallow Water Waves. *Journal of Waterway, Port, Coastal, and Ocean Engineering*, 142(1), 04015012. It is reprinted with permission from ASCE.

Moreover, Chen et al. (1999) and Kaihatu (2009) considered current effects in wave nonlinear interactions. Chen et al. (1999) found the triad interactions are enhanced by a following current and hindered by an opposing current. Using a wave spectrum, Kaihatu (2009) had similar finding when Ursell number is small. But with a large Ursell number, wave spectra broaden rapidly. Another environmental factor, wind, could affect triad interactions substantially too. Wind can increase wave height, and potentially increase wave nonlinearity; however, the role of wind in modifying nonlinear wave processes is still unexplored. For example, it is yet unclear whether wind will amplify or suppress triad interactions and if wind influence energy transfer among different frequencies.

Wave shape is indicative of wave nonlinearity in shallow water. High order statistics, such as wave skewness and asymmetry, describe asymmetry of wave profile with respect to the horizontal or vertical line. They have demonstrated a significant role in nearshore sediment transport. For example, Elgar et al. (2001) suggested onshore sand bar position could be related to wave asymmetry. Later Hoefel and Elgar (2003) found that acceleration skewness is a key factor in driving cross-shore sediment movements and thus important for predicting sandbar location. By analyzing laboratory data of shoaling and breaking waves, Kaihatu et al. (2007) also found a correlation between the location of maximum skewness and the location of maximum energy dissipation due to wave breaking. Therefore, in order to correctly predict morphological evolution of a beach, a good understanding of wave shape change in shallow water is highly desirable. In coastal areas, wind is commonly present and could affect wave shape as wave shoals, let alone the extremely strong wind during a hurricane or storm. However, little attention was given to wind effects on shape change of shallow water waves.

In order to simulate wind-wave interplay, we need to model air flow and the mechanism of momentum/energy exchange between air and water in addition to water wave motion. Different approaches have been adopted in numerical models for wind-wave dynamics. The first

category is to solve wave equations with well-designed boundary conditions to represent wind effects (Kharif et al., 2008; Chambarel et al., 2010; Yan and Ma, 2011). For instance, Chambarel et al. (2010) solved the potential flow equation for water waves and modeled the wind-induced pressure using the formula in Jeffreys (1925). The second category uses multi-phase models to solve a set of coupled equations for air and water. As an example, Xie (2014) solved Reynolds-averaged Navier-Stokes equations for air and water simultaneously to study the wind effects on solitary wave breaking. Unlike Navier-Stokes equations, Boussinesq models reduce the problem to two-dimension by depth integration. Due to the improved computation efficiency and the adequate physics, they have become favoured tools for coastal engineering community in the last decades. For a detailed review on the Boussinesq-type wave models, readers are refered to review papers by Madsen and Schaffer (1999), Kirby (2003) and Brocchini (2013). As an attempt to incorporate wind into Boussinesq models, Chen et al. (2004) parameterized wind effect as a flux term in momentum equation, and obtained reasonably good prediction of wave growth. The effects of wind on the higher order characteristics of waves, however, have not been considered in Chen et al. (2004).

This chapter is organized as follows: First, we develop a representation of wind effects in a Boussinesq-type wave model, and derive a set of evolution equations for the first three harmonics. Then, we solve the evolution equations numerically and validate the solution with experiment data. Next, wind effects on triad interactions are investigated with the Boussinesq model in conjunction with the evolution equations with wind effects. The influence of wind on wave shoaling on a mild beach is also studied. Finally, we summarize the findings.

2.2 Wave Triad Interactions and Evolution Equations

2.2.1 Derive evolution equations for Boussinesq-type wave model with winds

Despite the various forms of expressions, Boussinesq equations with wind can be written in general as

$$\eta_t + \nabla M = 0, \tag{2.1}$$

$$u_{\alpha,t} + (u_\alpha \nabla) u_\alpha + g\nabla\eta + V = S_{wind} \tag{2.2}$$

where η is the water surface elevation, u_α is the horizontal velocity at a reference depth, M is the horizontal volume flux, and V represents dispersive terms. S_{wind} is a source term representing wind effects. According to Jeffreys (1925), wind induced pressure at water surface can be related to local wave shape in the following way:

$$p_w = \rho_a s (U_{10} - c)^2 \frac{\partial \eta}{\partial x} \tag{2.3}$$

where ρ_a is air density, U_{10} is the wind speed at $10\,\mathrm{m}$ elevation, and c is the wave celerity. Coefficient s is the sheltering coefficient, and it is a measure of the resistance of wave form to wind.

The surface pressure p_w appears as an extra term in the dynamic boundary condition, and eventually in Boussinesq equations the wind source term becomes

$$S_{wind} = -\frac{\partial p}{\partial x}\frac{1}{\rho_w} = -\frac{\rho_a}{\rho_w} s |U_{10} - c| (U_{10} - c) \eta_{xx} \tag{2.4}$$

Special features of equation (2.4) are worth noting: First, wind effects become significant only when wind speed exceeds some critical value (Jeffreys, 1925; Chambarel et al., 2010). And thus in this paper, only results with large wind speed are discussed, which are all greater than wave celerity c. Secondly, this expression is valid for wind of different directions. When the wind blows in a direction opposite to wave propogation, S_{wind} changes sign and acts as a momentum

sink. Thirdly, the sheltering coefficient s is related to wind drag coefficient C_d based on the assumption that the phase-averaged momentum source due to wind-induced pressure should be equal to that originating from wind shear stress in other literatures. And the expression for C_d in Chen et al. (2004) is used since it has been verified with a large number of formulations. Therefore, s is a function of wind speed, wave height and wave number, and it could vary case by case.

Following the method of Jeffreys (1925), we incorporate wind effects into a fully nonlinear Boussinesq model, which is based on the FUNWAVE (Kirby et al., 1998). The Boussinessq Model with Wind (BMWW) serves as a numerical platform to study triad interactions under different wind conditions.

To analyze triad interactions, we also derive a set of EVolution equations for the first Three Harmonics (EVTH). Due to the limited accuracy of the dispersion property of the BMWW, we only consider the interactions of the first three harmonics instead of the whole spectrum. The multi-scale expansion is used to obtain the EVTH. And for simplicity, the equations in Madsen et al. (1991) are chosen as the starting point. The one-dimensional version of the model on a horizontal bed reads

$$\eta_t + hu_x + (\eta u)_x = 0 \tag{2.5}$$

$$u_t + uu_x + g\eta_x - \left(\frac{1}{3} + b\right) h^2 u_{xxt} - bgh^2\eta_{xxx} = -\frac{\rho_a}{\rho_w} s|U_{10} - c|\,(U_{10} - c)\,\eta_{xx} \tag{2.6}$$

where u is the depth-averaged velocity, and $b = 1/5$ for best dispersion property.

Assuming that the wave form modulation due to nonlinear interactions of wave components is much slower than the spatial variation of the free surface, we consider two scales: x and $X = \epsilon x$,

$$u(x, X; t)_x = u_x + u_X X_x = u_x + \epsilon u_X \tag{2.7}$$

Then continuity and momentum equations become

$$\eta_t + hu_x + \epsilon hu_X + (\eta u)_x + \epsilon(\eta u)_X = 0 \tag{2.8}$$

$$\begin{aligned} u_t + uu_x + \epsilon uu_X + g\eta_x + g\epsilon\eta_X - \left(\frac{1}{3}+b\right)h^2 u_{xxt} - 2\left(\frac{1}{3}+b\right)\epsilon h^2 u_{xXt} - bgh^2\left(\eta_{xxx} + 3\epsilon\eta_{xxX}\right) \\ = -\frac{\rho_a}{\rho_w} s|U_{10}-c|\left(U_{10}-c\right)\left(\eta_{xx} + 2\epsilon\eta_{xX}\right) \end{aligned} \tag{2.9}$$

Variables η and U can be expanded as power series with respect to ϵ:

$$\eta(x, X; t) = \epsilon\eta_1(x, X; t) + \epsilon^2\eta_2(x, X; t) + ... \tag{2.10}$$

$$u(x, X; t) = \epsilon u_1(x, X; t) + \epsilon^2 u_2(x, X; t) + ... \tag{2.11}$$

Substituting them into equation (2.8) and (2.9) gives

$$\epsilon(\eta_{1t} + hu_{1x}) + \epsilon^2\left[\eta_{2t} + hu_{2x} + hu_{1X} + (\eta_1 u_1)_x\right] = 0$$

$$\begin{aligned} \epsilon\left[u_{1t} + g\eta_{1x} - \left(\frac{1}{3}+b\right)h^2 u_{1xxt} - bgh^2\eta_{1xxx}\right] + \\ \epsilon^2\left[u_{2t} + u_1 u_{1x} + g\eta_{2x} + g\eta_{1X} - \left(\frac{1}{3}+b\right)h^2 u_{2xxt} - 2\left(\frac{1}{3}+b\right)h^2 u_{1xXt} - bgh^2\left(\eta_{2xxx} + 3\eta_{1xxX}\right)\right] \\ = -\frac{\rho_a}{\rho_w} s|U_{10}-c|(U_{10}-c)(\epsilon\eta_{1xx} + \epsilon^2\eta_{2xx} + 2\epsilon^2\eta_{1xX}) \end{aligned}$$

In a matrix form, the first-order equations can be expressed by

$$\begin{pmatrix} m_{11} & m_{12} \\ m_{21} & m_{22} \end{pmatrix}\begin{pmatrix} \eta_1 \\ u_1 \end{pmatrix} = 0 \tag{2.12}$$

where

$$\begin{aligned} m_{11} &= \frac{\partial}{\partial t}, & m_{12} &= h\tfrac{\partial}{\partial x}, \\ m_{21} &= g\frac{\partial}{\partial x} - bgh^2\frac{\partial^3}{\partial x^3}, & m_{22} &= \tfrac{\partial}{\partial t} - \left(\tfrac{1}{3}+b\right)h^2\tfrac{\partial^3}{\partial x^2\partial t} \end{aligned}$$

We assume that the wind source term is of the the magnitude of ϵ^2, and it belongs to the second-order equations which read

$$\begin{pmatrix} m_{11} & m_{12} \\ m_{21} & m_{22} \end{pmatrix} \begin{pmatrix} \eta_2 \\ u_2 \end{pmatrix} = \begin{pmatrix} f_1 \\ f_2 \end{pmatrix} \tag{2.13}$$

where

$$f_1 = -hu_{1X} - (\eta_1 u_1)_x,$$
$$f_2 = -\left[u_1 u_{1x} + g\eta_{1X} - 2\left(\frac{1}{3}+b\right)h^2 u_{1xXt} - 3bgh^2\eta_{1xxX} + \frac{\rho_a}{\rho_w}s|U_{10}-c|(U_{10}-c)\frac{\eta_{1xx}}{\epsilon}\right]$$

The requirement of a bounded second-order solution gives the so-called "solvability condition" as the following:

$$f_1 m_{22} - f_2 m_{12} = 0 \tag{2.14}$$

$$f_2 m_{11} - f_1 m_{21} = 0 \tag{2.15}$$

Equation (2.14) and (2.15) are essentially identical. If we choose equation (2.15), we have

$$\begin{aligned} & f_2 m_{11} - f_1 m_{21} \\ =& -\frac{\partial}{\partial t}\left[u_1 u_{1x} + g\eta_{1X} - 2\left(\frac{1}{3}+b\right)h^2 u_{1xXt} - 3bgh^2\eta_{1xxX} + \frac{\rho_a}{\rho_w}s|U_{10}-c|(U_{10}-c)\frac{\eta_{1xx}}{\epsilon}\right] \\ & + \left(g\frac{\partial}{\partial x} - bgh^2\frac{\partial^3}{\partial x^3}\right)(hu_{1X} + (\eta_1 u_1)_x) \end{aligned} \tag{2.16}$$

Three components are considered for η_1 and u_1:

$$\begin{aligned} \eta_1 &= \sum_{j=1}^{3} a_j(X)e^{i\phi_j} + C.C. \\ u_1 &= \sum_{j=1}^{3} P_j a_j(X)e^{i\phi_j} + C.C. \end{aligned} \tag{2.17}$$

where $P_j = w_j/(k_j h)$, $\phi_j = k_j x - w_j t$ for $j = 1, 2, 3$, and $C.C.$ denotes complex conjugate.

Expression (2.17) can be substituted into the solvability condition. For equation (2.15) to be valid for each harmonic, the following conditions need to be satisfied:

$$\frac{da_1}{dX} = -i\frac{A_1}{S_1}\bar{a_1}a_2 e^{i(\phi_2 - 2\phi_1)} - i\frac{B_1}{S_1}\bar{a_2}a_3 e^{i(\phi_3 - \phi_2 - \phi_1)} + \frac{K_{w1}}{S_1} \tag{2.18}$$

$$\frac{da_2}{dX} = -i\frac{A_2}{S_2}a_1^2 e^{i(2\phi_1 - \phi_2)} - i\frac{B_2}{S_2}\bar{a_1}a_3 e^{i(\phi_3 - \phi_2 - \phi_1)} + \frac{K_{w2}}{S_2} \tag{2.19}$$

$$\frac{da_3}{dX} = -i\frac{A_3}{S_3}a_1 a_2 e^{i(\phi_1 + \phi_2 - \phi_3)} + \frac{K_{w3}}{S_3} \tag{2.20}$$

with the coefficients

$$S_j = 2w_j g - 2\left(\frac{1}{3} + b\right) h w_j^3 + 4bgw_j k_j^2 h^2, j = 1, 2, 3 \tag{2.21}$$

$$A_1 = \frac{w_1 w_2}{h^2}(w_1 - w_2)\left(\frac{1}{k_2} - \frac{1}{k_1}\right) + \frac{g}{h}\left(\frac{w_1}{k_1} + \frac{w_2}{k_2}\right)(k_1 - k_2)^2 + bgh\left(\frac{w_1}{k_1} + \frac{w_2}{k_2}\right)(k_1 - k_2)^4 \tag{2.22}$$

$$B_1 = \frac{w_2 w_3}{h^2}(w_2 - w_3)\left(\frac{1}{k_3} - \frac{1}{k_2}\right) + \frac{g}{h}\left(\frac{w_2}{k_2} + \frac{w_3}{k_3}\right)(k_2 - k_3)^2 + bgh\left(\frac{w_2}{k_2} + \frac{w_3}{k_3}\right)(k_2 - k_3)^4 \tag{2.23}$$

$$A_2 = \frac{2w_1^3}{k_1 h^2} + 4g\frac{w_1 k_1}{h} + 16bghw_1 k_1^3 \tag{2.24}$$

$$B_2 = \frac{w_1 w_3}{h^2}(w_1 - w_3)\left(\frac{1}{k_3} - \frac{1}{k_1}\right) + \frac{g}{h}\left(\frac{w_1}{k_3} + \frac{w_3}{k_3}\right)(k_1 - k_3)^2 + bgh\left(\frac{w_1}{k_1} + \frac{w_3}{k_3}\right)(k_1 - k_3)^4 \tag{2.25}$$

$$A_3 = \frac{w_1 w_2}{h^2}(w_1 + w_2)\left(\frac{1}{k_2} + \frac{1}{k_1}\right) + \frac{g}{h}\left(\frac{w_1}{k_1} + \frac{w_2}{k_2}\right)(k_1 + k_2)^2 + bgh\left(\frac{w_1}{k_1} + \frac{w_2}{k_2}\right)(k_1 + k_2)^4 \tag{2.26}$$

$$K_{wj} = \frac{\rho_a}{\epsilon \rho_w} s a_j \left(k_j^2 w_j\right) |U_{10} - c|(U_{10} - c), j = 1, 2, 3 \tag{2.27}$$

Again, the expression of K_{wj} is valid for opposing wind as well, for which U_{10} becomes negative. We should also notice that K_{wj} depends on the perturbation parameter ϵ, and the influence of ϵ on the solution of evolution equations will be discussed in the next section.

2.2.2 Numerical solution and validation of evolution equations

The evolution equations are solved by applying a fourth-order Runge-Kutta method. As initial condition, all the energy is concentrated at the primary wave. The set of complex-variable differential equations can be treated in different ways: they can be split into amplitude and phase, into real and imaginary parts, or solved for complex variable directly. Our experiments show that the solutions from these three methods are nearly indistinguishable. We thus solve the complex-variable equations directly as an intuitive choice.

We choose the experiments of Chapalain et al. (1992) for validation. In these experiments, sinusoidal waves were generated and allowed to evolve on a flat bottom. The amplitude of the first three harmonics were measured along the tank for different wave conditions. One case with 40 cm water depth, 2.5 s wave period, and 4.2 cm wave amplitude is chosen as the validation for the numerical solution of equation (2.18) to (2.20). A spatial resolution of 0.05 m is used for the Runge-Kutta method, and the comparison between numerical solution and the data is plotted in Figure 2.1. Although the amplitude of the experimental data shows obvious decay along the tank due to bottom friction, within the first fifteen meters, the beat length and the amplitude of the primary wave and second harmonic match fairly well with the numerical solution of evolution equations.

One point worth mentioning here is the role of perturbation parameter ϵ in evolution equations. In literature, this parameter is commonly set to be wave amplitude parameter, since it is a small number for most shallow water cases. However, the multi-scale method does not pose any restrict on this perturbation parameter as long as it is small compared with the magnitude of other terms. We test a group of different values of ϵ, and they turn out to affect the beat length and the amplitude of second harmonic. Here $\epsilon = 0.43$ is used for best agreement.

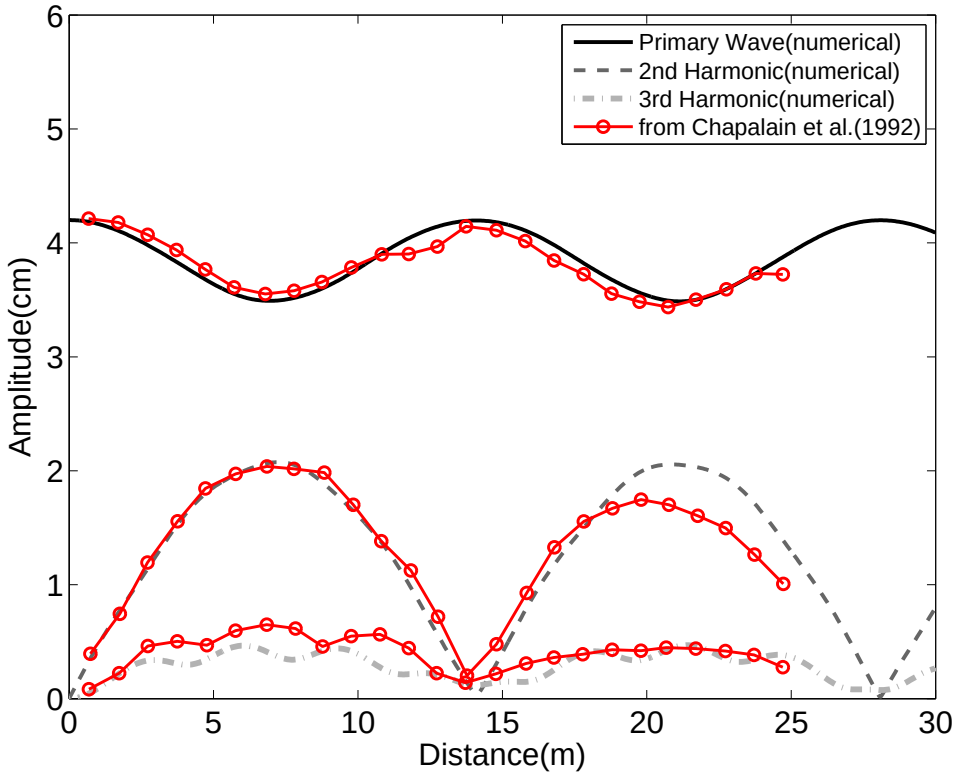

FIGURE 2.1: Numerical Solution of the EVTH from Fourth-Order Runge-Kutta Method versus the Experiment of Chapalain et al. (1992)

2.3 Wind Effects on Triad Interactions

2.3.1 Evolution equations with wind effects

With wind effects included in the evolution equations, we are able to not only obtain the evolution of each harmonic, but also predict the triad interactions under various wind conditions. Starting with the same conditions as the test case in the previous section, we added a

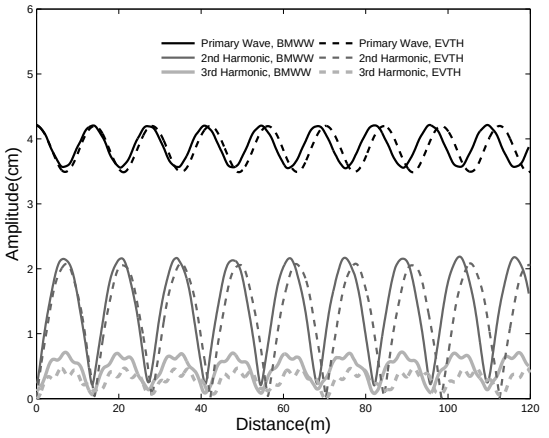

(a) No wind

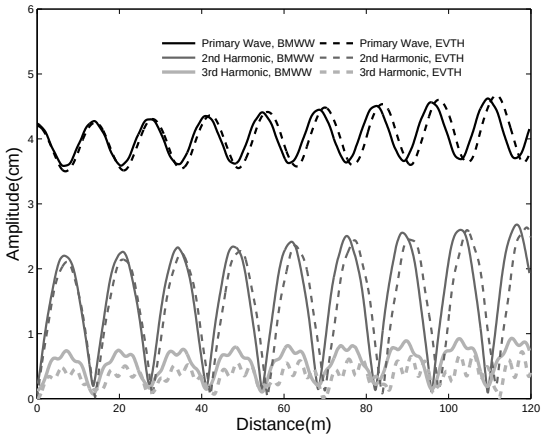

(b) Following Wind with Speed U=10 m/s

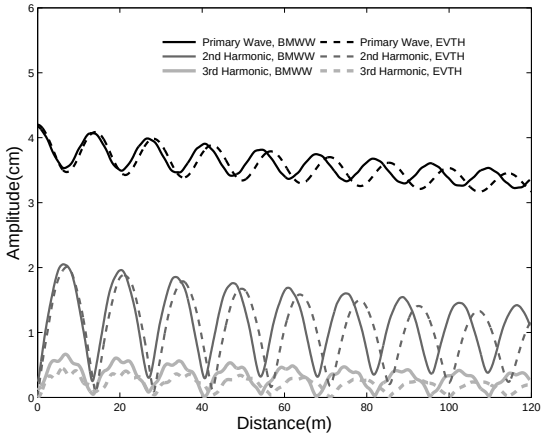

(c) Opposing wind with speed U= -10 m/s

FIGURE 2.2: Variation of the Three Harmonics under Different Wind Conditions (Solid Lines: from the BMWW; Dashed Lines: from the EVTH)

10 m/s following and opposing wind respectively on the numerical wave tank. The sheltering coefficient in this experiment is 0.07. Grid size and time step for the BMWW are 12 cm and 0.01 s respectively.

In the solution of the EVTH, the following wind apparently increases the amplitude of all the harmonics (Figure 2.2b). However, a question regarding the reason for the growth of high harmonics is yet to be answered. It may be due to the wind directly, or simply a result of primary wave growth causing more energy transfer. As a benchmark, we design another experiment of pure wave, with the amplitude equal to that at the end of wind fetch in the following wind case.

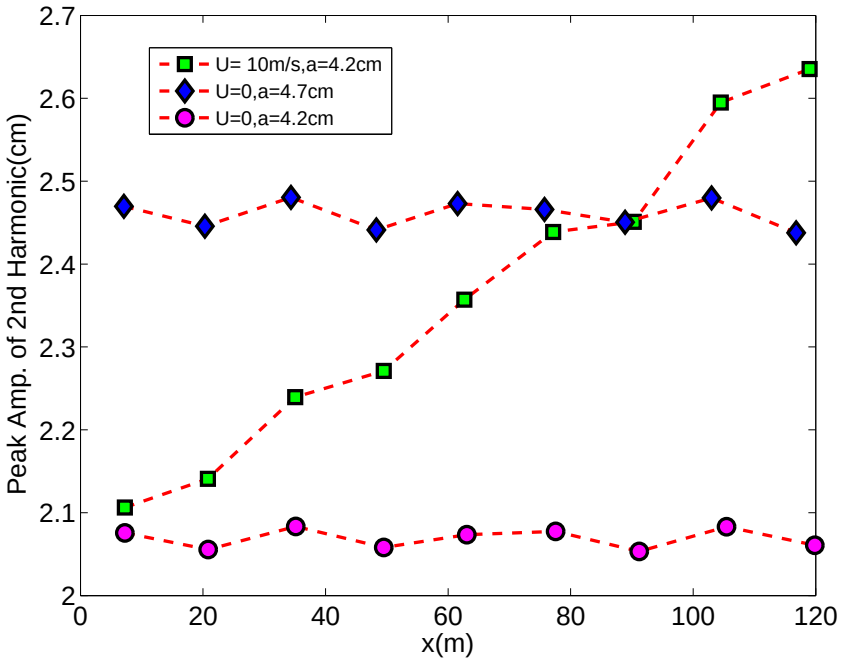

(a) Following wind

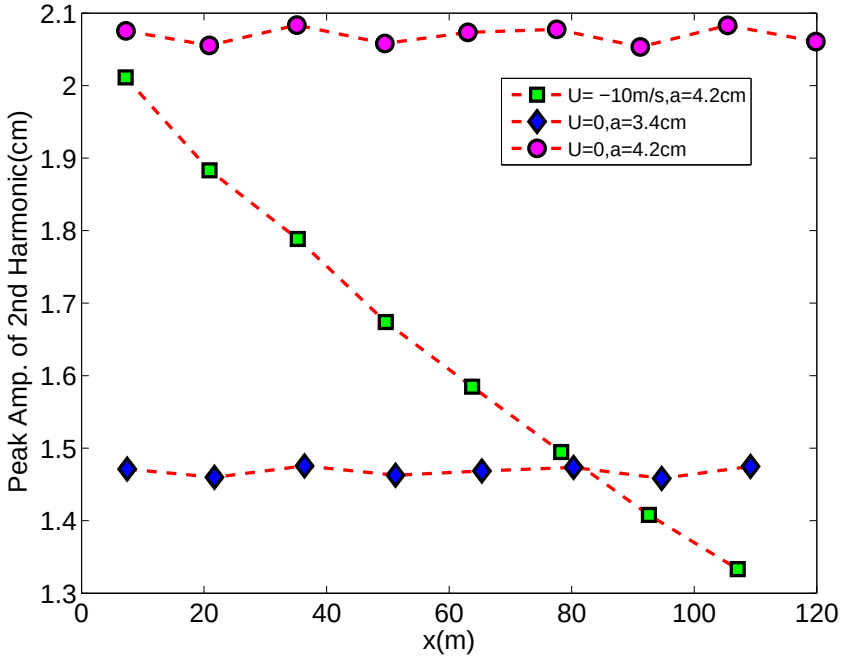

(b) Opposing wind

FIGURE 2.3: Second Harmonic Change due to Wind

Although the primary wave amplitudes are the same in the two cases, the second harmonic in pure wave case does not reach an amplitude as high as that under following wind (Figure 2.3a). Therefore, it is evident that the wind effects can amplify triad interactions by direct forcing into high harmonics; otherwise the second harmonic should also match between the two cases. This is not surprising if we look back into the evolution equations (2.18 to 2.20). The changing rate of high harmonics, i.e. a_2 and a_3 in equations, depends on not only a_1, but also the wind source term directly. In contrast, the opposing wind could reduce amplitude of all the harmonics, and suppress triad interactions by taking energy away directly from high harmonics(Figure 2.2c and 2.3b).

2.3.2 Boussinesq-type wave model with wind effects

Phase-resolving wave model, such as the BMWW, is able to predict the evolution of each single wave. Figure 2.4 presents the nonlinear wave envelope generated by the BMWW, with the same wave parameters as used in the EVTH. It also shows that the shallow water wave height raises gradually under $10\,$m/s following wind. Spectrum analysis of surface elevation time series further reveals the impact of wind on the energy transfer among different harmonics. Within the domain, the wind increases/decreases the amplitude of three harmonics to nearly the same degree as they do in the EVTH, though some differences exist (Figure 2.2). Compared with the EVTH, the BMWW gives smaller oscillation in primary wave and shorter beat length. Considering the fact that evolution equations are derived from weakly nonlinear Boussinesq equations while the BMWW solves the fully nonlinear ones, and the validity of evolution equations depends on the assumptions in multi-scale expansions, these differences should be acceptable.

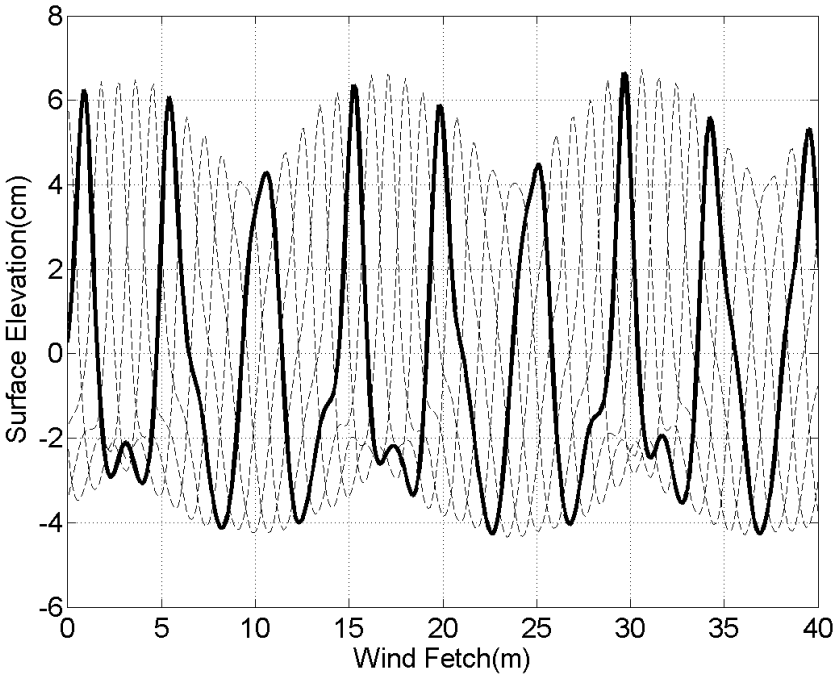

FIGURE 2.4: Wave Envelope with 10 m/s Following Wind Generated by the BMWW (Solid Lines: t = 279.2T; Dashed Lines: t = 279.4T, 279.6T, 279.8T, 280.0T)

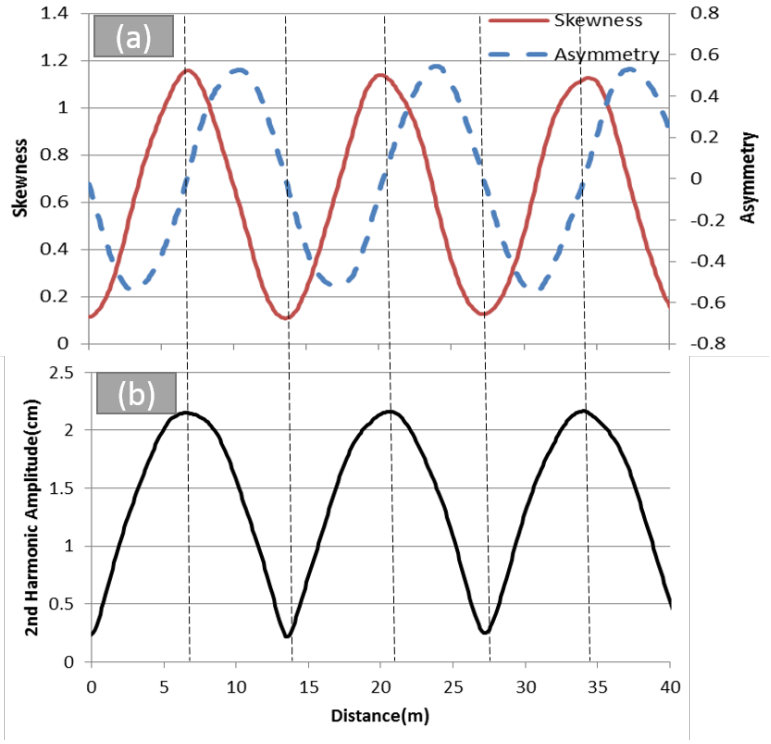

FIGURE 2.5: Skewness and Asymmetry Variation (a) in Relation to the Second Harmonic (b)

Triad interactions influence wave shape as well. In our test case, wave skewness and asymmetry vary in space with the same period as beat length(Figure 2.5). Maximum skewness, which corresponds to the most peaked crest, occurs where the second harmonic gains the largest energy, while the largest asymmetry happens when the second harmonic is neither largest nor smallest. We also observe that following wind increases the amplitude of skewness and asymmetry, but the variation pattern due to triad interactions is maintained.

2.4 Wind Effects on Wave Shoaling

When waves propagate from deep water to shallow water, shoaling often occurs under wind. Although the EVTH is derived for flat bottom, the BMWW is capable of modeling wave propagation in varying water depth and thus allows us to investigate wind effects on wave shoaling. To our knowledge, no controlled laboratory experiments has been conducted to investigate wave shape change during shoaling with different wind conditions, with the exception of Feddersen and Veron (2005).

In this section, we apply the BMWW to model wave shoaling on a mild slope (1/100) with both 15 m/s onshore (positive speed) and offshore (negative speed) winds, under which the sheltering coefficient is 0.096. The water depth at the toe of the slope is 1m, and we generate a wave train with 6 cm wave height and 2.5 s wave period. The time step and grid size in the simulations are 0.01 s and 12 cm, respectively. The wave shape change and the corresponding nonlinear effect before wave breaking will be discussed based on our simulation.

In wave shoaling, wave height usually goes up as water depth decreases. This trend is enhanced by the onshore winds as shown in Figure 2.6. Moreover, Fourier analysis reveals that energy input is concentrated at the harmonics, which is consistent with the observation in Feddersen and Veron (2005). The offshore winds, on the contrary, hinder wave growth on the slope. If offshore wind is strong enough, it is even able to reduce the overall wave height.

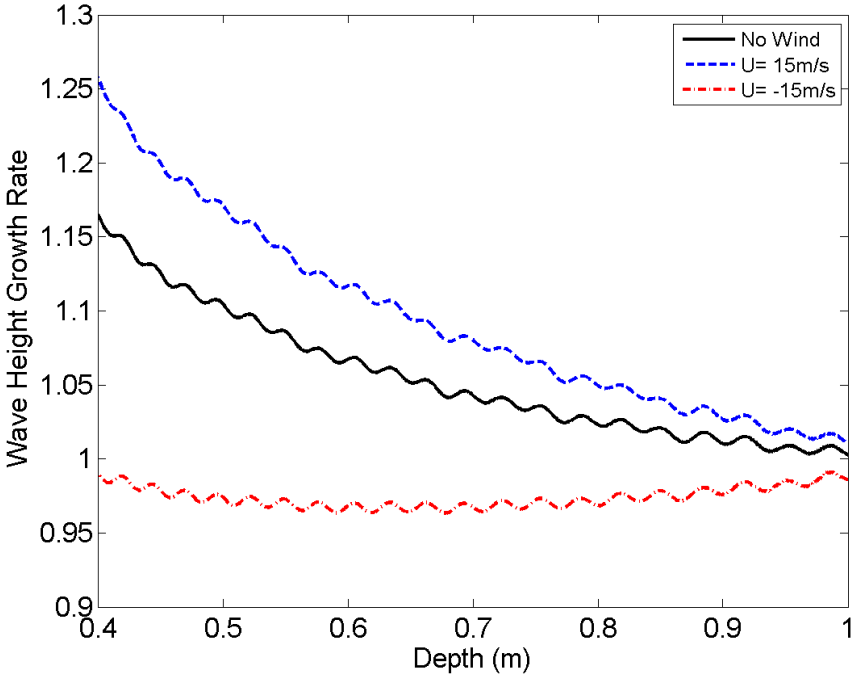

FIGURE 2.6: The Wave Height Variation under Different Wind Conditions on a 1/100 Mild Slope

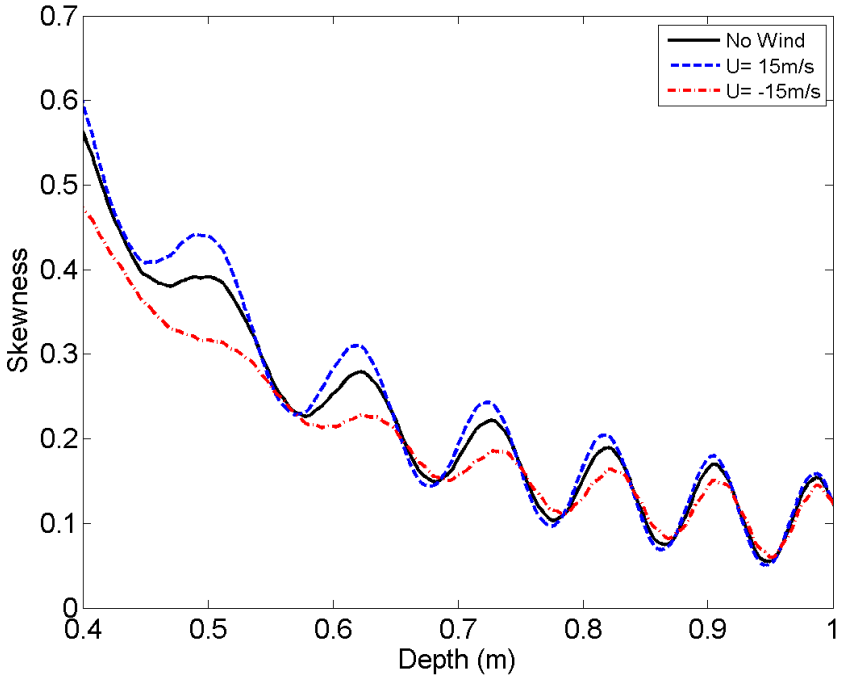

FIGURE 2.7: The Wave Skewness Variation on the Same Slope as Figure 2.6

In general, shoaling process raises wave skewness as waves propagate from deep to shallow water as in Figure 2.7. In the mean time, the absolute value of asymmetry also increases, although asymmetry has a negative sign because most of the time the wave profile skews into the direction opposite to the one defined as positive (Figure 2.8). As an evidence of the BMWW's capability to predict shape change under wind, the BMWW has been used to model wave propagation with a 1/8 slope, the same as the experiment in Feddersen and Veron (2005). With onshore winds, wave becomes peaky and skewed forward(Figure 2.9), similar to the observation in Feddersen and Veron (2005).

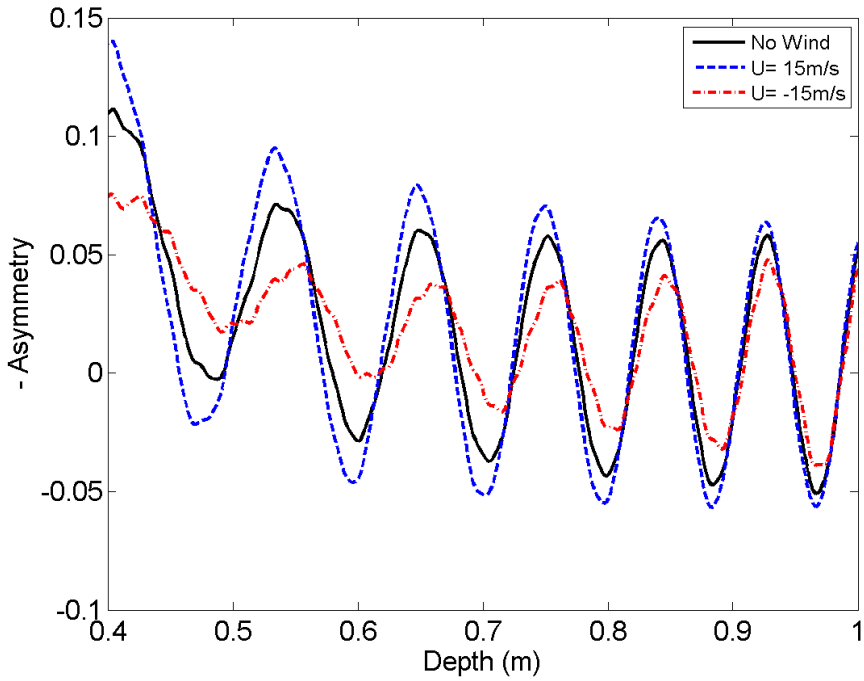

FIGURE 2.8: The Wave Asymmetry Variation on the Same Slope as Figure 2.6

It should be noticed that neither skewness nor asymmetry increases monotonically on the slope. For example, some degree of oscillation is present in wave skewness during shoaling (Figure 2.7), and that oscillation is related to the periodic variation of second harmonic (Figure 2.10b) in the same manner as the flat bottom cases discussed previously. With onshore

winds, the oscillation of skewness/asymmetry is amplified and the oscillation period is slightly modified, which can be attributed to the enhanced triad interactions under onshore winds. Further more, due to this oscillation, wave skewness or asymmetry does not increase with wind speed at all locations. For instance, wave asymmetry with wind is greater than that without wind at the depth of 0.63 m, while they are almost indistinguishable at the depth of 0.65 m. This may explain why Feddersen and Veron (2005) found wave shape to be sensitive to wind speed at the shallow location while it is not the case at the deep location. Therefore wave shape change with wind depends not solely on water depth but also controlled by triad interactions in shallow water.

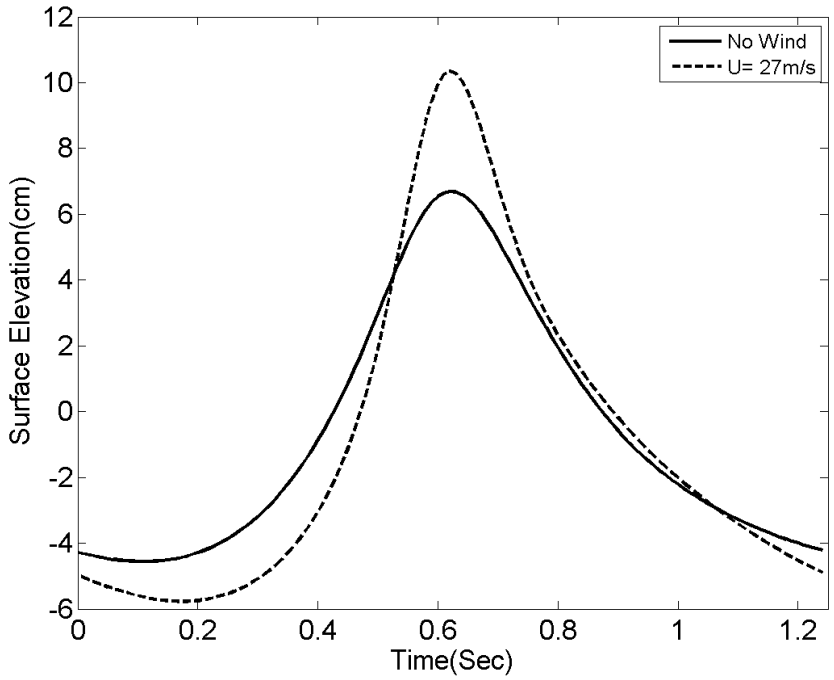

FIGURE 2.9: Simulated Wind-induced Change in Mean Wave Profile at Location II in Feddersen and Verron(2005) (Solid line: U=0; Dashed line: U=27 m/s)

Although wave breaking is not involved, our results indicate some interesting features for wave breaking under wind conditions. With onshore wind, waves become larger and the most asymmetric waves along the slope are further distorted. Therefore it is not surprising that an

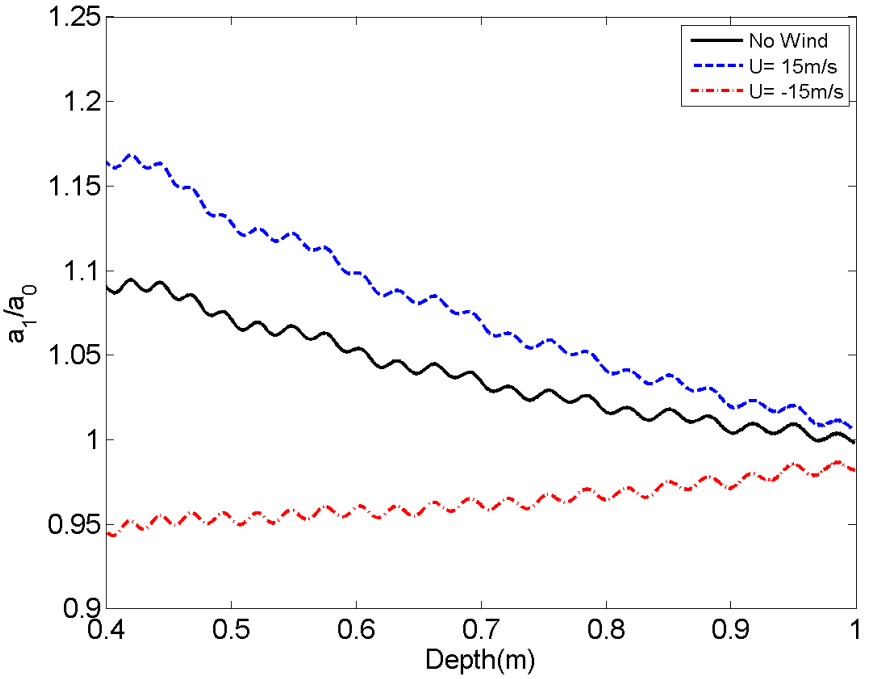

(a) The first harmonic

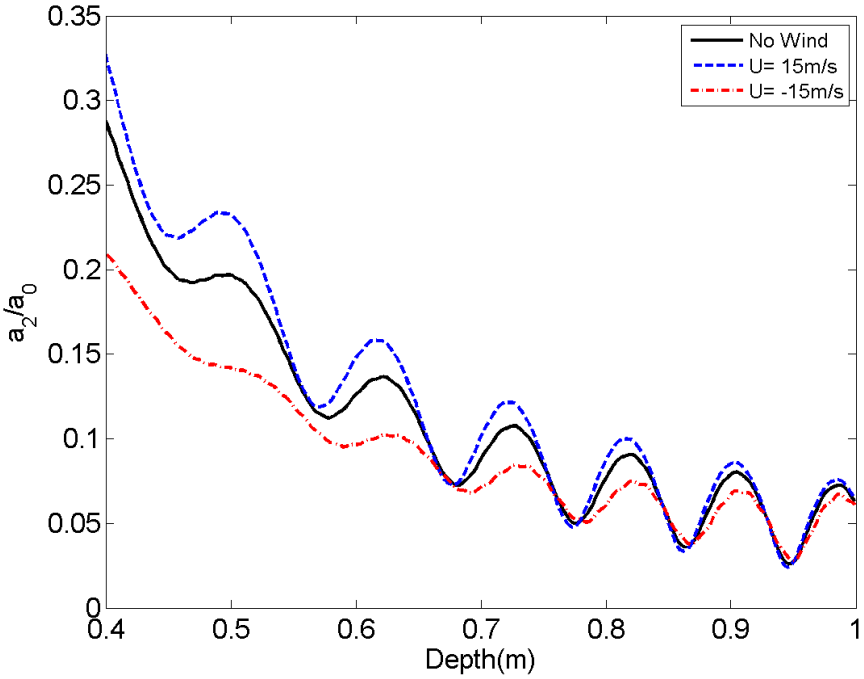

(b) The second harmonic

FIGURE 2.10: The Variation of Amplitude of the First Two Harmonics on the Same Slope as Figure 2.6

onshore wind would cause the waves to break earlier as in Douglass (1990), Chen et al. (2004) and Xie (2014). Boussinesq equations do not include the physics of wave breaking directly, but other models, such as Navier-Stokes equations, have been applied to model the broken waves in the surfzone (Bradford, 2000; Xie, 2014). Considering the effects of onshore winds, Xie (2014) suggested that the potential and kinetic energy of water waves were increased and the energy transfer between water and air was altered during wave breaking. The maximum run-up after wave breaking was also increased as a result of onshore winds.

2.5 Conclusions

In this paper, wind effects as pressure variation on water surface following the sheltering mechanism by Jeffreys (1925) are included in a Boussinesq-type wave model. Based on the obtained Boussinesq Model With Wind (BMWW), EVolution equations for the first Three Harmonics (EVTH) are derived for constant water depth with one-dimensional winds. We solve the evolution equations using fourth order Runge-Kutta method, and the solution is validated against the laboratory measurement of Chapalain et al. (1992). Both the amplitude of harmonics and beat length agree well with the measurement.

We then apply the EVTH and the BMWW to study the wind effects on triad interactions. Results from both methods consistently show that following (opposing) winds tend to increase (decrease) the amplitude of all the harmonics. Moreover, a fast growth of second harmonic suggests that following winds infuse energy directly into high harmonics, in addition to raising the primary wave and growing higher harmonics through energy transfer from the primary wave to free triads.

During wave shoaling, both bounded and free high harmonics are generated. The BMWW predicts the increased wave height and wind-induced shape change, similar to the observation in laboratory wave flume by Feddersen and Veron (2005). In general, onshore winds amplify triad interactions while offshore winds do the opposite. Another interesting result in simulation

is that wave skewness and asymmetry are not only controlled by water depth, but also affected by triad interactions. That might explain the difference in the wave shape sensitivity to winds at different locations reported by Feddersen and Veron (2005).

In conclusion, the EVTH provides an analytical tool to understand wind effects on wave triad interactions in shallow water. The BMWW allows us to take wind into account when simulating nearshore processes, which is highly needed under some extreme conditions such as hurricanes and storms.

One possible future direction would be to incorporate the wind generation mechanism into a phase-resolving nonlinear frequency domain model (Kaihatu and Kirby, 1995; Agnon and Sheremet, 1997). These models would serve as generalizations of the evolution equations derived herein, as they simulate the evolution and interaction of a spectrum of freely-propagating waves.

CHAPTER 3 HURRICANE HYDRODYNAMICS DURING GUSTAV (2008)

3.1 Introduction

The contribution of frequent hurricanes and storms to the delivery of sediment to the coastal wetlands on Louisiana coast has been discussed in many literature (Morgan et al., 1958; Chamberlain, 1959; Roberts et al., 1987; Rejmanek et al., 1988; Reed, 1989; Nyman et al., 1995; Cahoon et al., 1995; Turner et al., 2006; McKee and Cherry, 2009). Some researchers attributed this large-scale transport to the work of storm surge and waves. For example, in one of the pioneering study by Chamberlain (1959), the author hypothesized that most of the observed materials in the marsh region were carried onshore by the storm surge and laid down as receding water encountered a barrier. Reed (1989) evaluated the relative contribution to marsh sedimentation of each flooding event from 1985 to 1986 in Terrebonne Bay. The author found an association between the increased deposition rate and the passage of storm events and explained this association with the raising water level and increased sediment transport during storms.

The above-mentioned studies point to the fact the exact amount and spatial distribution of sediment deposition on coastal wetlands will depend notably on the spatial range, time and duration of flooding caused by storm surges. In addition, if the deposited material comes from the hurricane-driven suspension, as suggested in some literature (Roberts et al., 1987; Rejmanek et al., 1988), hurricane waves could be another important factor in determining the amount of suspended material and thus the available sediment for deposition.

This chapter is devoted to the development and validation of a fully-coupled storm surge and wave model using Delft3D. First, the hydrodynamic model is briefly reviewed in Section 3.2. The study area and Hurricane Gustav (2008) are introduced in Section 3.3. Then model configuration for some key processes and the coupling between the flow model and the wave model are described in Section 3.4. The performance of wave model in the stand-alone mode

is validated by comparing the prediction of offshore wave with the measurements at NDBC stations in Section 3.5. The accuracy of modeled storm surge and nearshore waves is evaluated with multiple datasets in Section 3.6. A summary is given in Section 3.7.

3.2 Hydrodynamic Models

3.2.1 Flow module

Delft3D is a multi-dimensional (2D or 3D) finite difference hydrodynamic model capable of simulating non-steady flow and transport phenomena in coastal areas, estuaries, rivers and lakes, and it has been calibrated and applied to storm surge modeling for a number of hurricane cases (Vatvani et al., 2012; Mulligan et al., 2014; Hu et al., 2015). Delft3D is able to model not only flow problem, but also multiple physical processes related to transport phenomena, including surface waves (by coupling the spectral wave model SWAN as a wave module), water density stratigraphy, and turbulence mixing. All of these features make it a good candidate for modeling hurricane-induced sediment transport and morphological changes.

Although a three-dimensional model has the advantage in better resolving the vertical flow structure, vegetation effects and some physical processes in sediment transport (Lapetina and Sheng, 2015), it has been shown that a carefully calibrated 2-D model can achieve similar accuracy in the prediction of tidal current and bed deposition at a tidal mangrove with much greater computational efficiency (Horstman et al., 2013, 2015). Moreover, the water body is probably well mixed in the inner shelf and estuaries during high-energy events such as a hurricane (Chen et al., 2008). Considering our focus is depth-integrated sediment fluxes in the shelf-bay-wetland system and sediment mass accumulations on wetlands instead of the bottom boundary layer details, the 2-D version of Delft3D model was used in this chapter.

The storm surge and tides were simulated by solving the nonlinear shallow water equations using a finite-difference method in Delft3D-FLOW. The vertically integrated governing equations in a Cartesian coordinate (ξ, η) read

$$\frac{\partial \zeta}{\partial t} + \frac{\partial[(d+\zeta)u]}{\partial \xi} + \frac{\partial[(d+\zeta)v]}{\partial \eta} = Q \tag{3.1}$$

$$\frac{\partial u}{\partial t} + u\frac{\partial u}{\partial \xi} + v\frac{\partial u}{\partial \eta} - fv = -\frac{P_\xi}{\rho_0} + F_\xi + M_\xi \tag{3.2}$$

and

$$\frac{\partial v}{\partial t} + u\frac{\partial v}{\partial \xi} + v\frac{\partial v}{\partial \eta} + fu = -\frac{P_\eta}{\rho_0} + F_\eta + M_\eta \tag{3.3}$$

where d is the local water depth, ζ is the free-surface elevation above mean-sea level, Q is the discharge or withdrawal of water, precipitation and evaporation, f is the Coriolis coefficient, P_ξ and P_η are the pressure gradient, F_ξ and F_η are the turbulent momentum flux in ξ or η direction, M_ξ and M_η represent other source and sink terms in the momentum equations including the free-surface wind stress and bottom shear stress.

Vegetation plays a unique role in coastal protection by attenuating strong winds, waves and storm surge. In our model, the flow resistance caused by vegetation drag was modeled as a sink term, $-\lambda u^2$, in the momentum equation, and it was strictly separated from the bed friction itself (without vegetation) to avoid unrealistic exaggeration of bed shear stress for sediment transport (Baptist, 2005). For emergent plant,

$$\lambda = C_D m D \tag{3.4}$$

For submerged vegetation,

$$\lambda = C_D m D \frac{h_v}{h}\frac{C_b^2}{C^2} \tag{3.5}$$

and

$$C = C_b + \frac{\sqrt{g}}{K}\ln\left(\frac{h}{h_v}\right)\sqrt{1 + \frac{C_D m D h_v C_b^2}{2g}} \tag{3.6}$$

where C_D is the vegetation drag coefficient, C_b is the roughness of the bed without vegetation, m is the number of stems per unit area, D is the vegetation stem diameter, h and h_v are the local water depth and vegetation height, and K is the von Karman constant.

3.2.2 Wave module

Simulate WAve Nearshore (SWAN) is a third-generation phase-averaged wave model for simulating surface waves in deep, intermediate and shallow waters and it has been incorporated into the Delft3D modeling suite as the wave module. The governing equation in SWAN is the wave action balance equation:

$$\frac{\partial N}{\partial t} + \frac{\partial C_{gx} N}{\partial x} + \frac{\partial C_{gy} N}{\partial y} + \frac{\partial C_{g\sigma} N}{\partial \omega} + \frac{\partial C_{g\theta} N}{\partial \theta} = \frac{S}{\omega} \tag{3.7}$$

where t represents time; (x, y) are the horizontal coordinates; ω denotes the intrinsic angular frequency; θ represents the propagation direction of the wave component; N is the wave action and defined as $N(x, y; \sigma, \theta) = E(x, y; \sigma, \theta)/\sigma$ where $E(x, y; \sigma, \theta)$ stand for the wave energy density. C_{gx}, C_{gy}, $C_{g\omega}$ and $C_{g\theta}$ are the speed of energy propagation in $x-$, $y-$, $\omega-$, and $\theta-$ space, respectively.

The right hand side of Equation (3.7) symbolizes a sum of energy source and sink terms, such as the energy input from winds, the energy dissipation due to wave breaking, bottom friction, white-capping and nonlinear wave-wave interactions. The balance equation in both Cartesian and spherical coordinates and their solutions are given in details by Booij et al. (1999). The propagation scheme in the curvilinear version of SWAN has been formulated on a general curvilinear grid, which is advantageous for a geographic domain with a complex lateral boundary.

The vegetation effect on wave height reduction was modeled by means of Madsen et al. (1988)'s formulation, where the roughness length was related to the local water depth h and

vegetation-enhanced Manning's coefficient n in the following way:

$$z_0 = h \exp\left[-\left(1 + \frac{Kh^{\frac{1}{6}}}{n\sqrt{g}}\right)\right] \tag{3.8}$$

where g is the gravitational acceleration and K is the von Karman constant. At each SWAN time step, z_0 was updated using the computed water level from the storm surge model.

3.3 Study Area and Hurricane Gustav (2008)

Our study area is in the wetland-bay-shelf system in the Terrebonne-Barataria Basins. The Terrebonne-Barrataria Basins are located in south Louisiana, between the Mississippi River and the Atchafalaya River, open to the Gulf of Mexico to the south. This region encompasses a large area and a wide variety of marshes and swamps, from freshwater marsh to brackish marsh and saline marsh, and it has been experiencing severe marsh erosion and land loss with the highest rate in Louisiana. According to Couvillion et al. (2011), the total land loss from 1932 to 2010 is 421.71 square miles in Barataria and 459.99 square miles in Terrebonne.

This region was affected by multiple major hurricanes in the last decade, including Katrina and Rita in 2005, Gustav and Ike in 2008 and Isaac in 2012. In this study, we chose Hurricane Gustav as an example. Hurricane Gustav was the first major hurricane to track through southeast Louisiana since Katrina in 2005. It formed on August 25, 2008 in Haiti, and rapidly strengthened into a hurricane. Gustav gradually weakened to Category 2 when it entered the Gulf of Mexico and made landfall on September 1 near Cocodrie, Louisiana. Despite its weakened strength, the large outreach and the long duration of its impact on the coastal system created a wide swath of destruction to Louisiana that was surpassed only by Katrina.

3.4 Model Setting

3.4.1 Model domain and nested Mesh

In order to better resolve the complex geometry of the Louisiana coast, a nested two-layer curvilinear mesh was designed (Figure 3.1). The Gulf of Mexico (GoM) mesh covered the Gulf of Mexico, the Caribbean Sea and part of the western North Atlantic Ocean to capture the

development of the fast-moving hurricane and provide accurate surge level and current velocity to the detailed domain. The nested domain (LA mesh) extended from Galveston Bay (TX) to the west, to the Mobile Bay (AL) to the east, covering the entire Louisiana coast.

The GoM mesh had a grid resolution varying from 50 km in Atlantic Ocean to about 10 km near the Louisiana coast. The grid size of the LA mesh was 1-3 km on the continental shelf, 200-500 m in coastal wetlands and lakes, and 60-80 m across the Mississippi River.

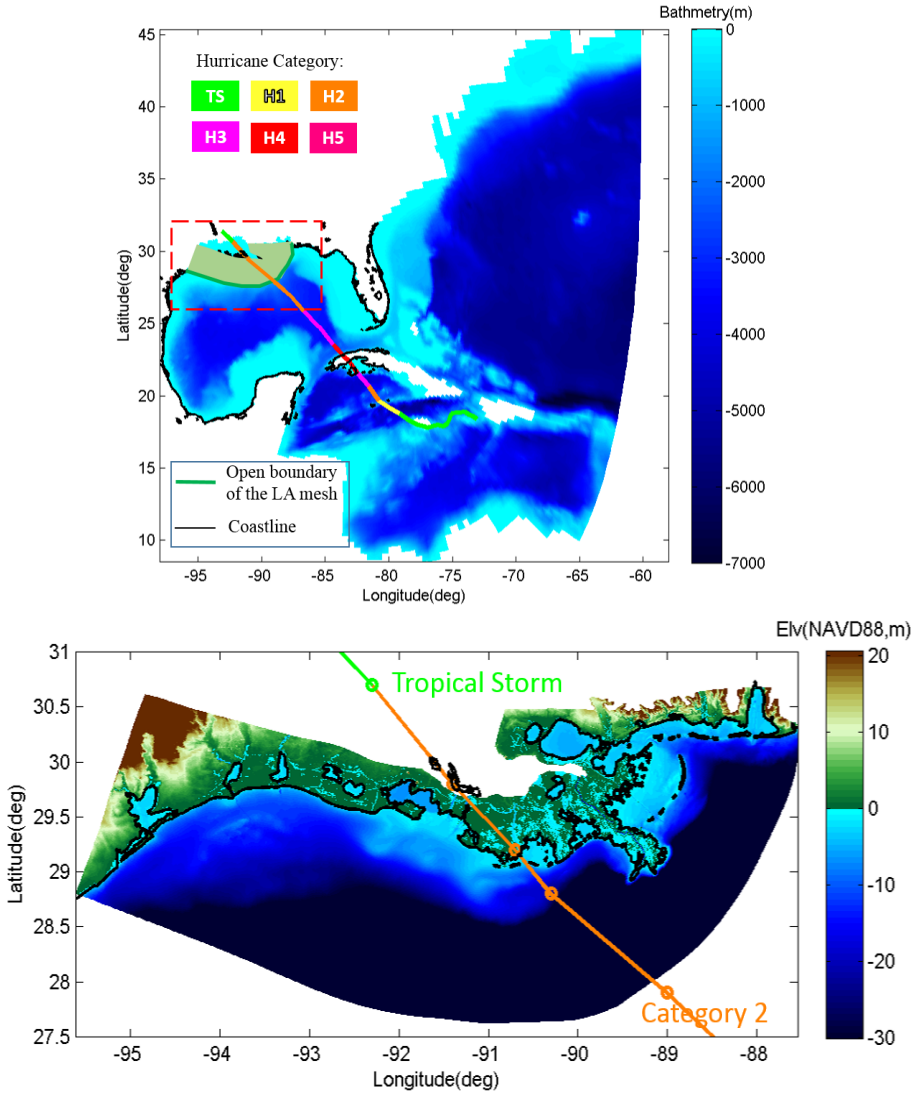

FIGURE 3.1: Bathymetry for the nested domain (Top: GoM mesh; Bottom: LA mesh)

3.4.2 Bathymetry and land cover

The bathymetric data from the SL16 mesh (Dietrich et al., 2011) was used for the entire GoM mesh and a large part of the LA mesh. The digital elevation model (DEM) output from the Wetland and Barrier Shoreline Morphology models (Couvillion et al., 2013; Hughes et al., 2012) and LIDAR data from the national elevation dataset (NED, `http://nationalmap.gov/elevation.html`) were further applied for marshes and bayous in the Breton Sound estuary, Barataria Bay and Terrebonne Bay.

In our model, the spatial distribution of vegetation types was determined according to a coastal-wide aerial survey by the U.S. Geological Survey (USGS) in 2007 (Sasser et al., 2008). Totally eleven vegetation types were included in the model. The corresponding physical properties, namely vegetation height, stem diameter and vegetation density, were specified based on USDA Natural Resources Conservation (NRCS) herbaceous plant online database (`http://plants.usda.gov/java/factSheet`) and other literature (Visser, 2007). The vegetation-enhanced Mannings value in the wave model was generated for each of the eleven vegetation types following the same way as in Dietrich et al. (2011).

3.4.3 Offshore boundary and tidal conditions

The storm surge can be considered as a combination of a pure wind-driven surge and astronomical tides, and thus a reasonable boundary condition for the magnitude and phase of tides is the first step to an accurate prediction of storm surge. In our model, tidal variation of water level from TPXO 7.2 (`http://volkov.oce.orst.edu/tides/global.html`) was forced at the offshore boundary. TPXO is a global tides model considering eight primary (M2, S2, N2, K2, K1, O1, P1, Q1), two long period (Mf and Mm) and three nonlinear (M4, MS4, MN4) harmonic constituents. The methods used to compute the model can be found in Egbert et al. (1994) and Egbert and Erofeeva (2002).

River inflows were specified for the Mississippi River using the water discharge time series at Baton Rouge, obtained from USGS National Water Information System (`http://maps.waterdata.usgs.gov/mapper/index.html`). Although an increasing river discharge can be expected during the hurricane, our experiments showed that the impact of river discharge on surge level was very limited during Gustav.

3.4.4 Hurricane wind and pressure

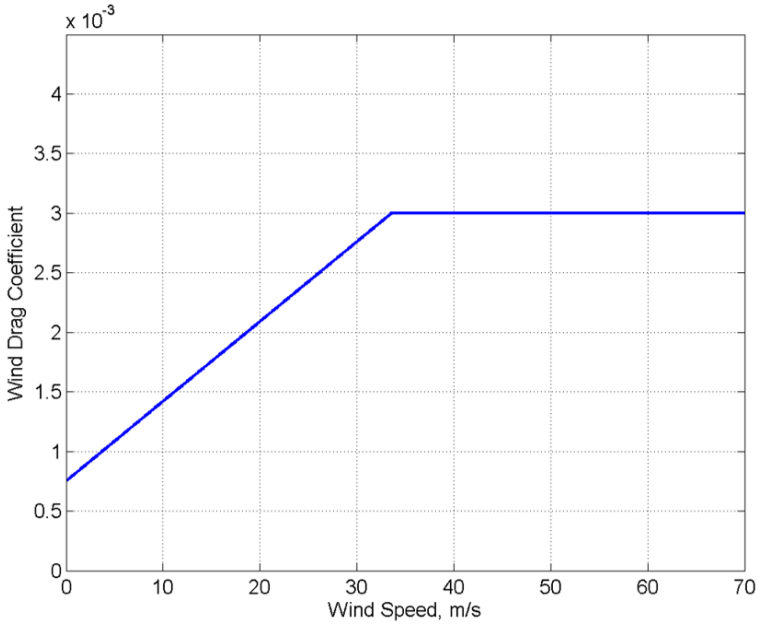

FIGURE 3.2: The wind drag coefficient increasing with wind speed

An improved parametric wind model for asymmetric hurricanes (Hu et al., 2012) was used to simulate the wind field and air pressure during Hurricane Gustav. Storm parameters were obtained from the National Hurricane Center (NHC)'s best track data (`http://www.nhc.noaa.gov/data/`). The large-scale background wind provided by the National Center for Environmental Prediction (NCEP) was also merged with the hurricane winds. The wind drag coefficient was set to be a linear increasing function of wind speed with a cap of 0.003 according to Garratt(1977) (Figure 3.2).

3.4.5 Spectral wave model

The wave model, SWAN, used the same mesh as the flow model. The wave directions were discretized into 36 directional bins with a constant width of 10 degree. The GoM mesh had a frequency range of 0.03 to 0.55 Hz on a logarithmic scale discretized in 29 frequency bins, and the LA mesh had a frequency range of 0.05 to 1.0 Hz discretized in 24 bins. In shallow water, depth-induced wave breaking was computed with the breaking index $\gamma = 0.73$. The dissipation due to white-capping was based on van der Westhuysen et al. (2007). Triad interactions in shallow water were activated with $\alpha = 0.1$ and $\beta = 2.2$. Diffraction was disabled. Hot-start files were used to better utilize the results from the previous time step and save computation time.

3.4.6 Coupling wind, surge and wave models

In this study, the hurricane wind, surge and wave models were running in a fully coupled manner (Figure 3.3). The surge model provided surge level and current velocity to the wave computation. The wave model computed the radiation stresses that would further elevate surge level and drive nearshore current.

For Hurricane Gustav, the simulation time was eight days from August 28 to September 5, 2008, following a one-month spin-up time. The time step for the storm surge simulation was 0.5 minute, while the wave model ran in the non-stationary mode with a 60-minute interval. The coupling interval was 60 minutes.

3.5 SWAN Model and Offshore Waves

3.5.1 Data description

The National Data Buoy Center (NDBC) operates wave buoys across the Gulf of Mexico. Wave spectral energy parameters, including significant wave height, peak and mean period, and mean direction, are obtained from the measurements (`http://www.ndbc.noaa.gov/`).

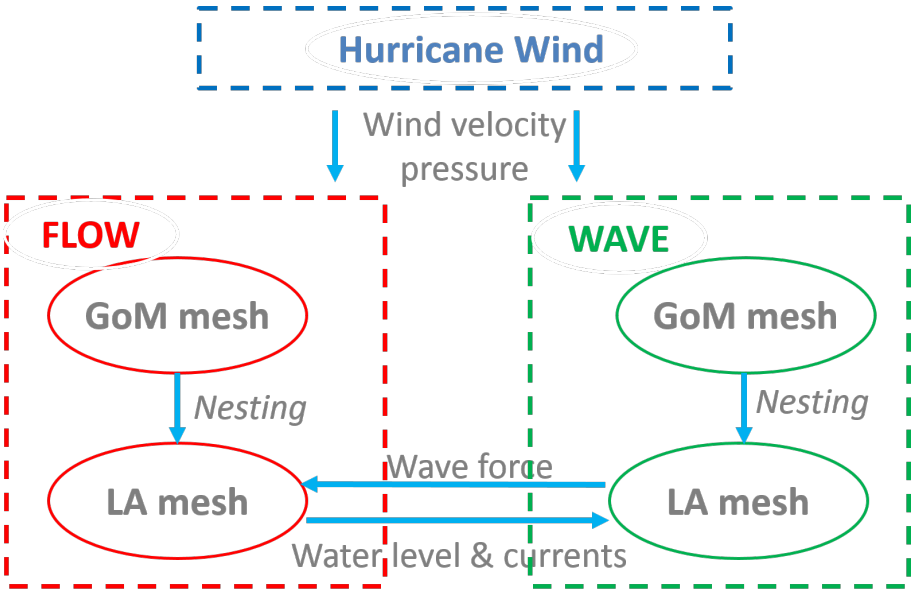

FIGURE 3.3: Data flow and mesh layer in the coupled flow and wave model

We collected data for Hurricane Gustav at nine gauges in the Gulf of Mexico (Figure 3.4), and they will be compared to results from wave model SWAN.

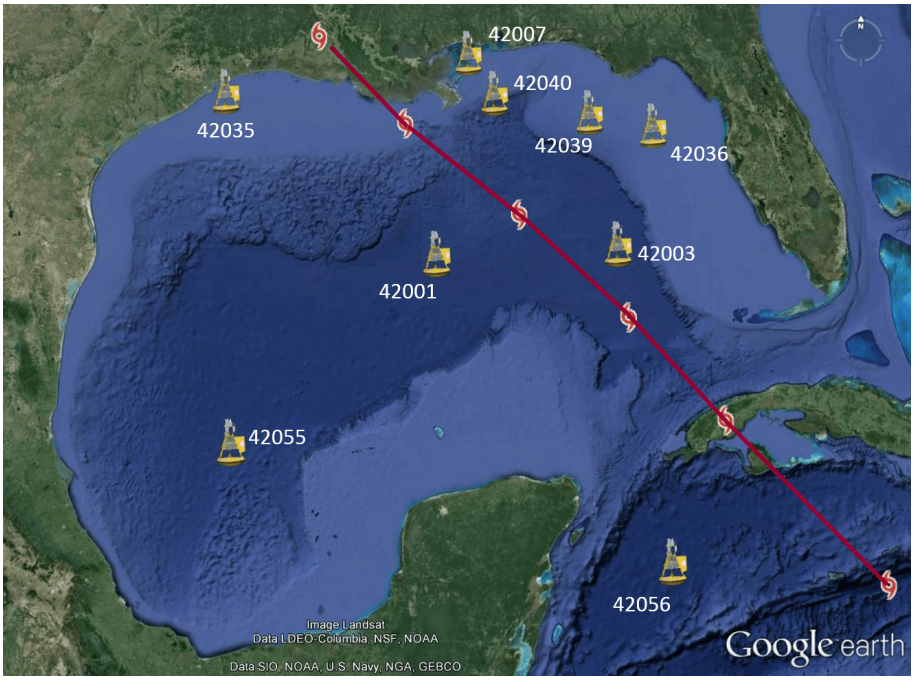

FIGURE 3.4: The locations of NDBC wave gauges in the Gulf of Mexico (red line: the track of Hurricane Gustav)

3.5.2 Model results

In the Gulf of Mexico, waves propagated as swells and wave height increased significantly as the hurricane passed (Figure 3.5). The maximum wave height exceeded 10 m at Station 42040 and 42003 and decreased with the distance to the track of Gustav. To the east of the track, the peak value decreased from about 12 m (42040) to about 5 m (42036) close to Florida. On the west side, it decreased from 6 m (42001) to 2 m (42035) near Texas. The wave periods also increased as the wave grew (Figure 3.6), and the wave directions experienced a dramatic change when the hurricane passed (Figure 3.7). For the GoM mesh, the wave model and the flow model were not coupled as the wave and surge interactions were not important in deep water. The wave model SWAN ran in a stand-alone mode, and the good agreement of model results to the measurements at NDBC suggested that the hurricane wind was represented correctly and the wave model was capable of modeling wave growth under wind.

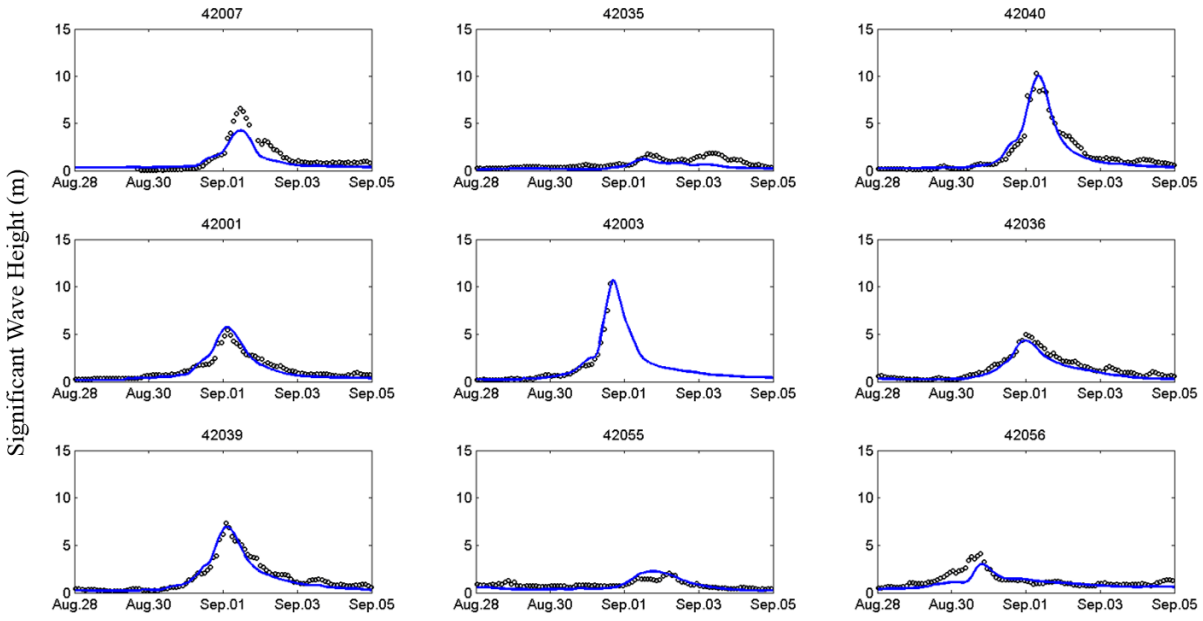

FIGURE 3.5: Comparison of modeled wave heights (blue lines) with the observations at NDBC stations (black circles)

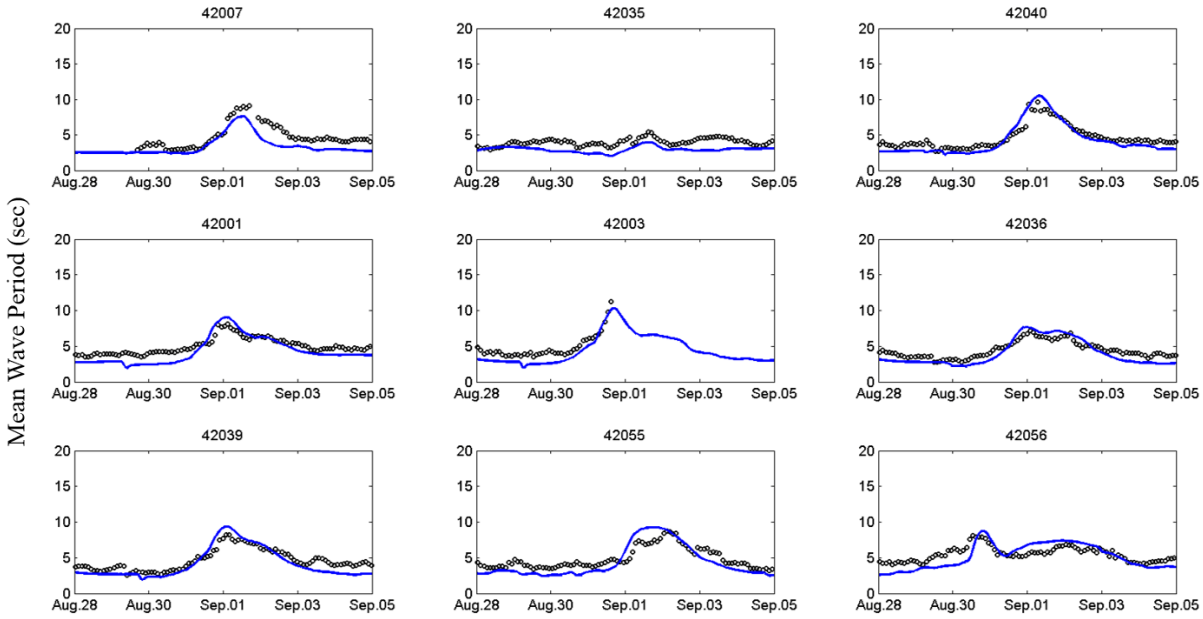

FIGURE 3.6: Comparison of modeled wave periods (blue lines) with the observations at NDBC stations (black circles)

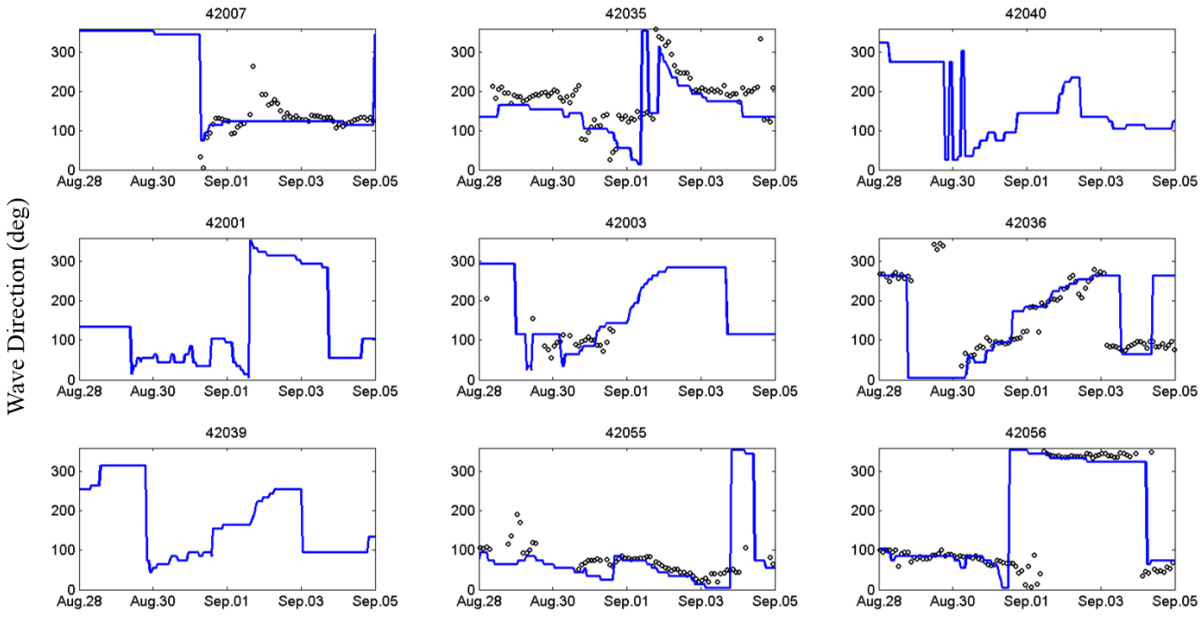

FIGURE 3.7: Comparison of modeled wave directions (blue lines) with the observations at NDBC stations (black circles)

3.6 Nearshore Wave-Surge Interactions

3.6.1 Data Description

The following sections describe the measurement data along the coast line, which offered a valuable description of the evolution of storm surge and waves along the Louisiana coast during Hurricane Gustav.

a. NOAA tides and currents:

NOAA operates a national-wise network of tides and currents stations. The measured water levels during Gustav were compared to our model results at eleven stations within the detailed domain from Dauphin Island (8735180) to Galveston Pleasure Pier (8771450) (Figure 3.8). The measured water levels are relative to MSL.

b. Wave gauges by Kennedy et al. (2010):

Sixteen gauges deployed by Kennedy et al. (2010) provided a record of the nearshore wave behavior during Gustav. Waves and water levels were measured using bottom-mounted pressure sensors recording continuously at 1 Hz (Kennedy et al., 2010). Wave heights were computed through standard spectral methods, and surge levels were obtained by applying a low-pass filter to water levels. Among all the gauges, six of them were located within the region of our interest and served as bench marks for the modeled wave heights and wave periods (Figure 3.8).

c. Surge level at CRMS:

The Coastwide Reference Monitoring System (CRMS) is a joint effort by the Louisiana Coastal Protection and Restoration Authority (CPRA) and USGS to address the needs to monitor and evaluate the effectiveness of implemented coastal projects. A total of 390 monitoring sites are operated within nine coastal basins, covering the whole Louisiana coast. 108 stations have records of surge levels during Gustav within the Barataria-Terrebonne Basins. After removing the gauges with incomplete or obviously inconsistent records near the peak of the storm, we compared the observed peak surge at 87 stations with model predictions (Figure 3.9).

3.6.2 Model Results

The strong winds during Gustav caused large swells exceeding 10 m significant wave height to the southeast of the Louisiana coast (Figure 3.10). As the long waves approached the shoreline, they broke and dissipated quickly due to the shallow continental shelf and the bottom friction. At nearshore wave station 1, 8, and 9 (Kennedy et al., 2010) outside of Terrebonne Bay, where the local water depth was 7 to 10 m, the maximum significant wave heights were 3 to 5 m, while at station 11 in the southeast corner of Barataria Bay, the local water depth was 3.5 m and the peak wave height was less than 2 m. The peak periods at all these stations were between 15 and 20 s. Station 13 and 14 were located on the Caernarvon Marsh. The vegetation further attenuated wave energy, and the wave height decreased with the inland distance. The wave model over-estimated the wave height at station 14, which may be explained by the limited spatial resolution for the biophysical properties of marsh vegetation and a lack of calibration for the vegetation-induced energy dissipation. The peak period was under-estimated at station 13 by the model, and the inaccurate topography might have contributed to the error of the wave period. Nevertheless, the wave growth and energy dissipation were generally well simulated by the wave model.

To quantify the agreement between the modeled and the observed hydrodynamic processes, the normalized bias and the Scatter Index (SI) of the time series were defined as the following:

$$Bias = \frac{\frac{1}{N}\sum_{i=1}^{N} E_i}{\frac{1}{N}\sum_{i=1}^{N} |O_i|} \tag{3.9}$$

and

$$SI = \frac{\sqrt{\frac{1}{N}\sum_{i=1}^{N}(E_i - \bar{E})^2}}{\frac{1}{N}\sum_{i=1}^{N} |O_i|} \tag{3.10}$$

where N is the number of observation points in the time series, $E_i = S_i - O_i$ is the difference between the model result S_i and the observation O_i. By definition, the normalized bias describes the mean error. SI, the standard deviation of E_i, indicates how much the predicted variation

pattern is deviated from the observed one. A smaller SI means more similarity between the simulated and the observed time series. Because the model resolution was not high enough to resolve the marsh surface, the inland station 14 was excluded from the computation of model error and the resultant bias for wave heights was 0.10. The bias for water level and peak periods at all the stations in Kennedy et al. (2010) were 0.07 and 0.17, respectively (Figure 3.11 and Table 3.1).

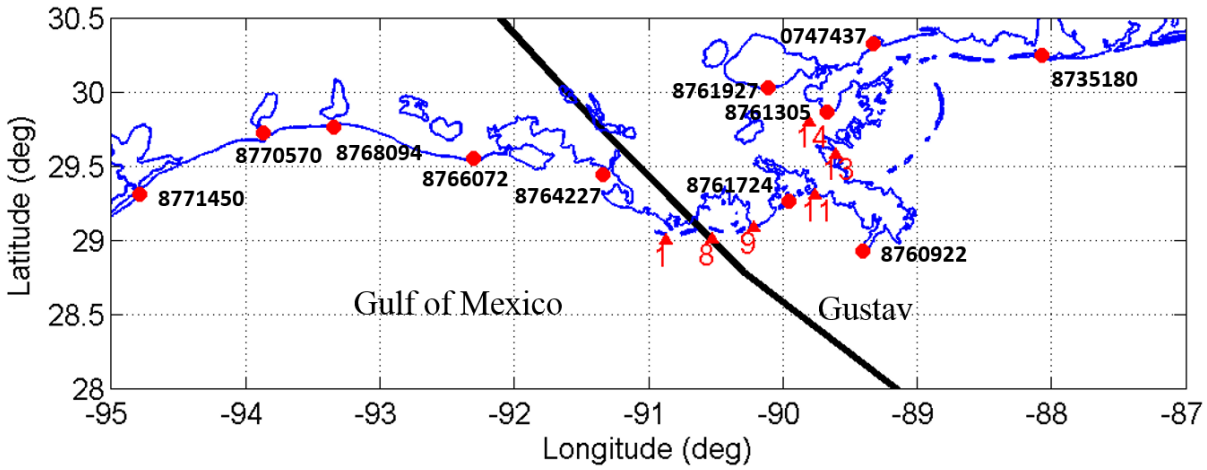

FIGURE 3.8: The location of NOAA stations (red dots) and Kennedy et al. (2010)'s wave gauges (red triangles)

NOAA stations:

In general, the model prediction of storm surge was in good agreement with observations at NOAA tides and currents stations (Figure 3.12). In the southeastern Louisiana, a significant flooding water can be observed and the highest storm surge appeared in the Breton Sound Basin (Figure 3.13) thanks to the long-lasting south-easterly wind and the blocking of the Mississippi River levee. Moreover, the peak surge occurred earlier on the west of the Mississippi River than it did on the east. Overall, the bias and SI for the stations in the southeastern Louisiana were -0.08 and 0.18 (from station 8735180 Dauphin Island to station 8761724 Grand Isle in Figure 3.12). In the western part of the Louisiana coast, the influence of storm surge was rather

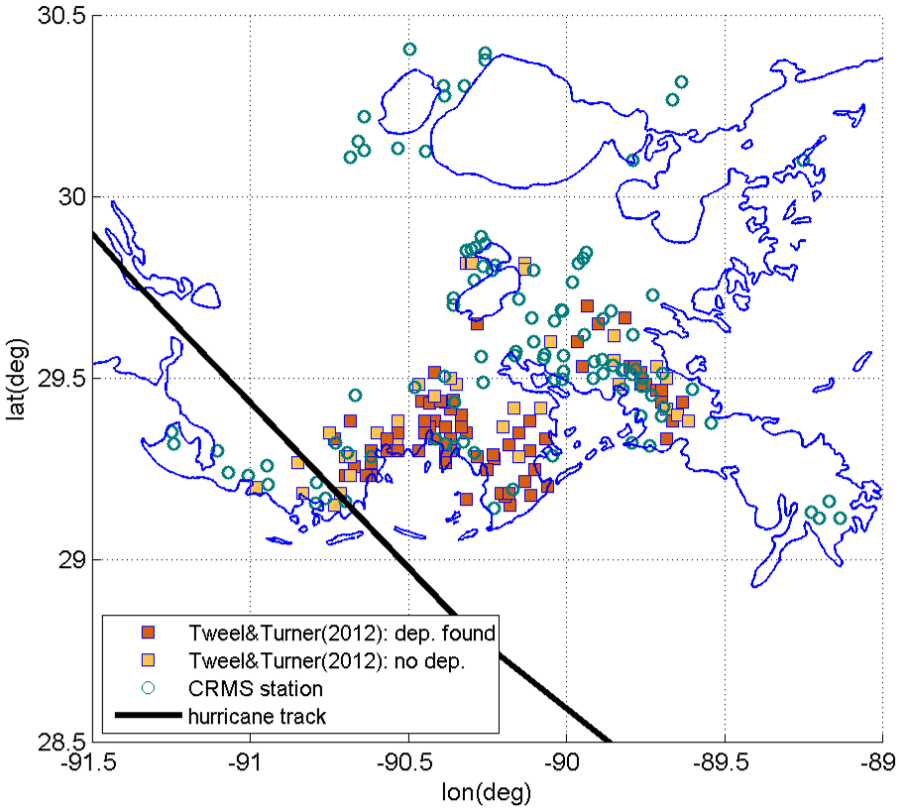

FIGURE 3.9: The locations of the CRMS stations (circles) and the survey sites in Tweel and Turner (2012) (rectangles)

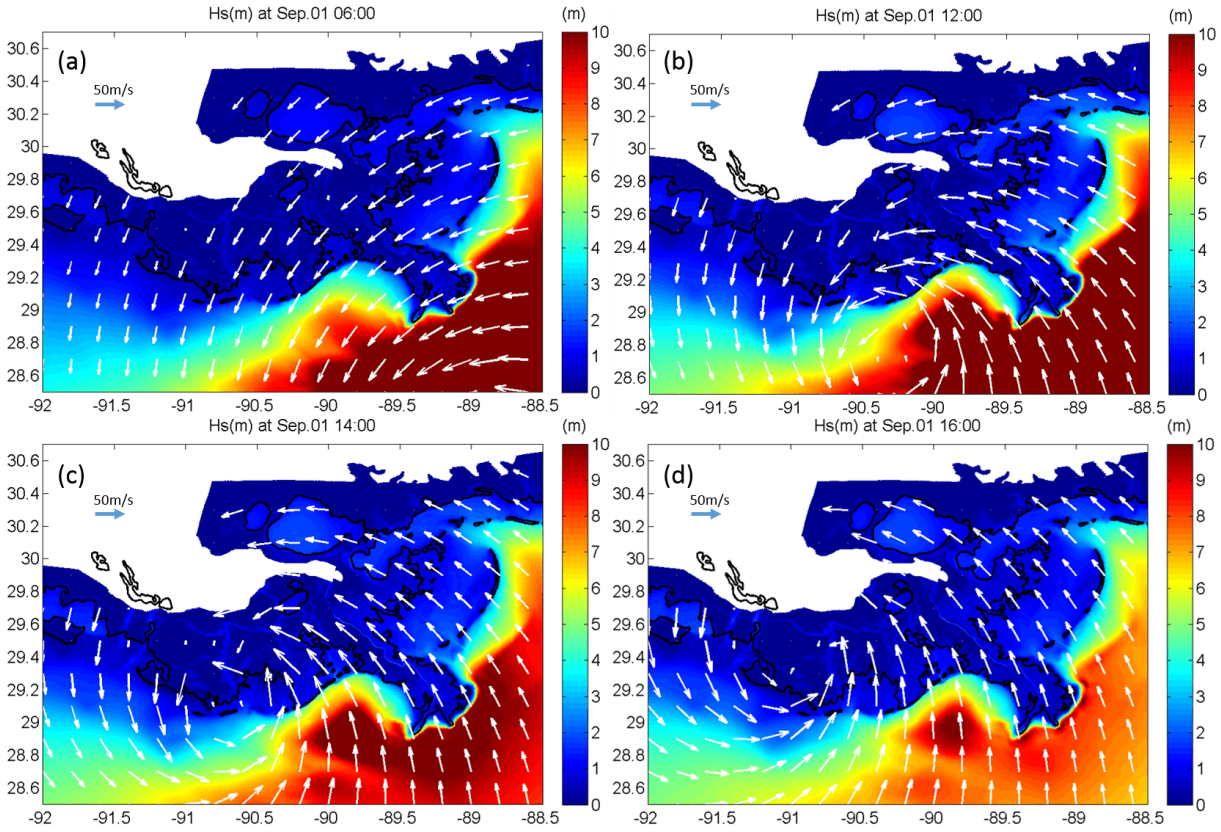

FIGURE 3.10: The simulated wind field (white arrows) and significant wave height before and after the landfall of Gustav (2008): (a) 06:00 UTC, Sep 01, or approximately 8 hours before landfall, (b) 12:00 UTC, Sep 01, or approximately 2 hours before landfall, (c) 14:00 UTC, Sep 01, or approximately landfall, and (d) 16:00 UTC, Sep 01, or approximately 2 hours after landfall.

limited, and model results captured the tidal variation of water level fairly well (from station 8764227 LAWMA to station 8771450 Galveston Pier in Figure 3.12). Because of the relatively low water, the SI of all of the 11 stations was 0.35 (Table 3.1).

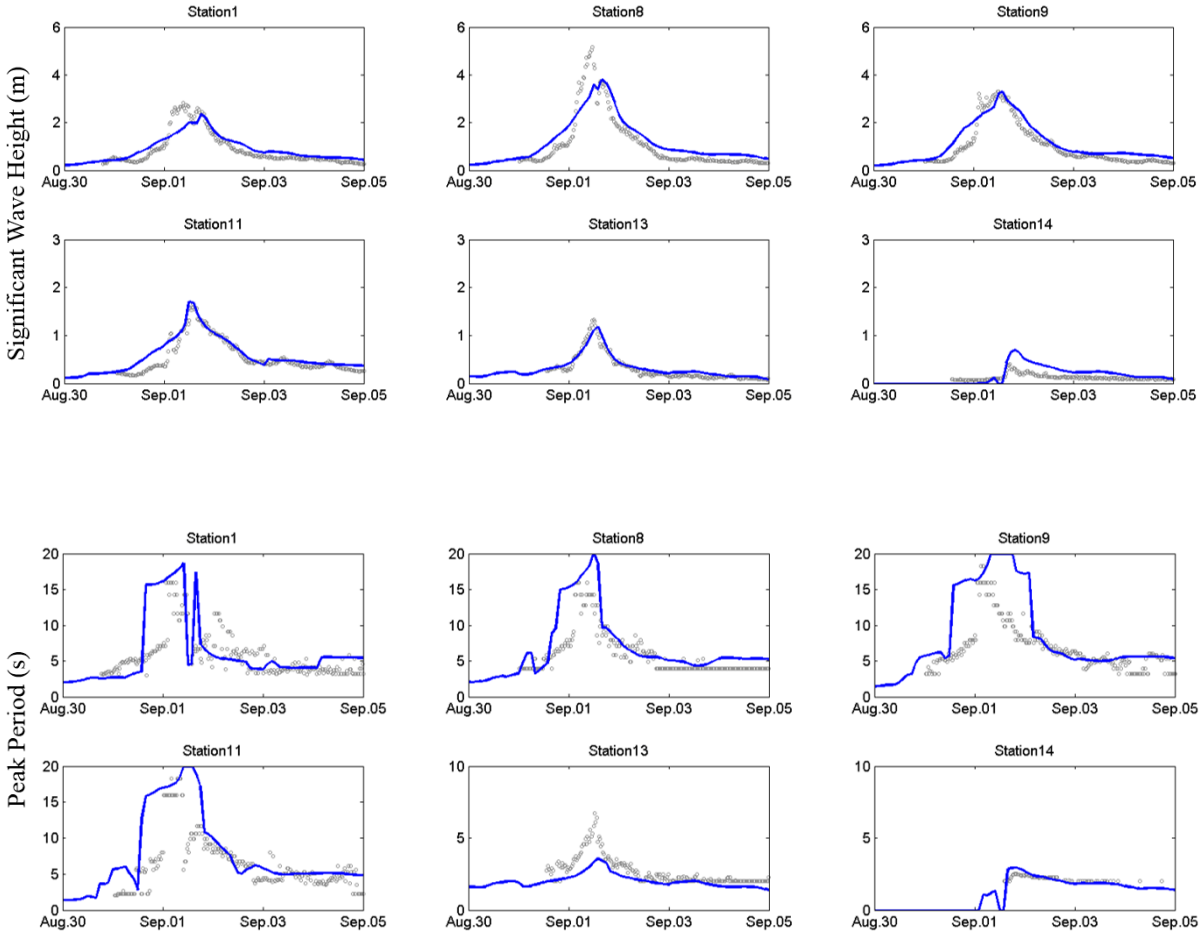

FIGURE 3.11: Comparison of modeled wave heights and periods (blue lines) with the observations (black circles) in Kennedy et al. (2010)

CRMS:

To simulate the inland surge flooding accurately is more challenging than that in the coastal water. Many factors, including vegetation friction and local structures, come into play. To validate the model performance in predicting the extent of surge flooding on coastal wetlands, the modeled peak surge was compared with observations at the CRMS stations during Gustav. The surge levels in Barataria Bay and Terrebonne Bay were in the range of 1 to 2 meters. The slope

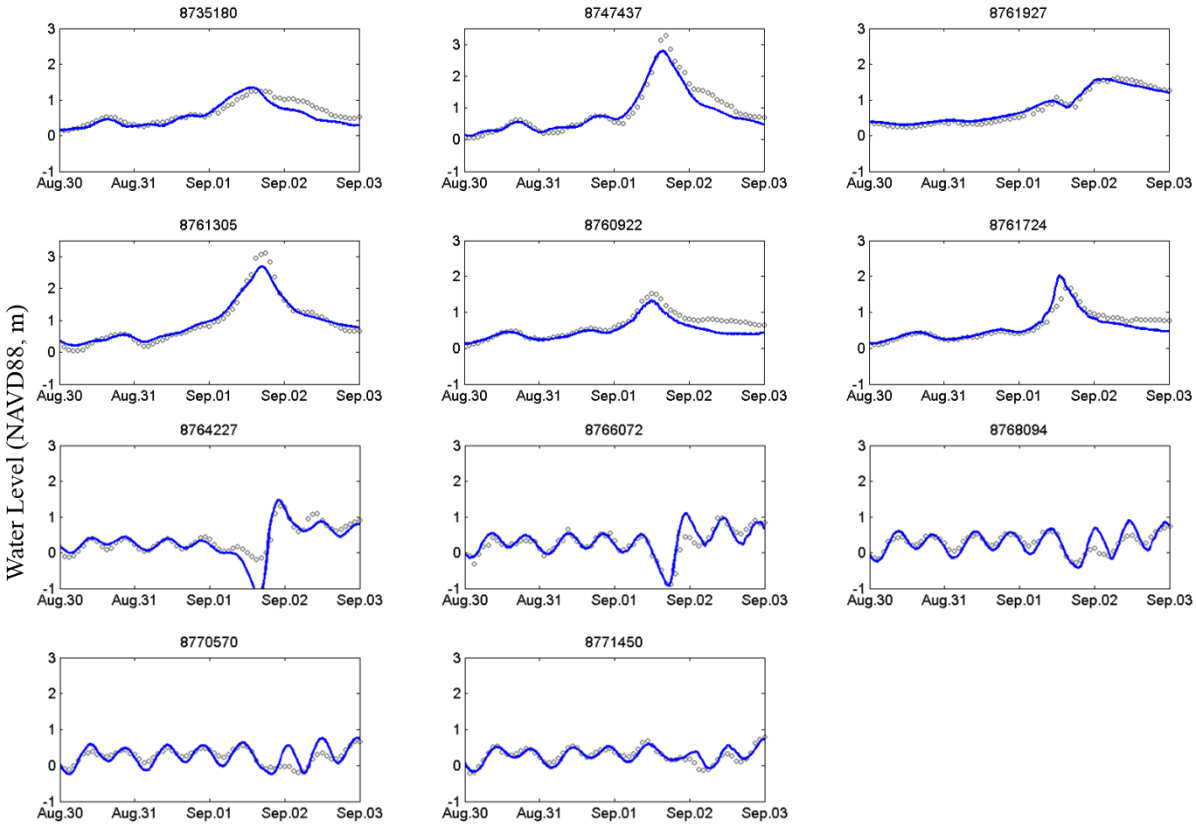

FIGURE 3.12: Comparison of modeled water levels (blue lines) with observations (black circles) at the NOAA tides and currents stations

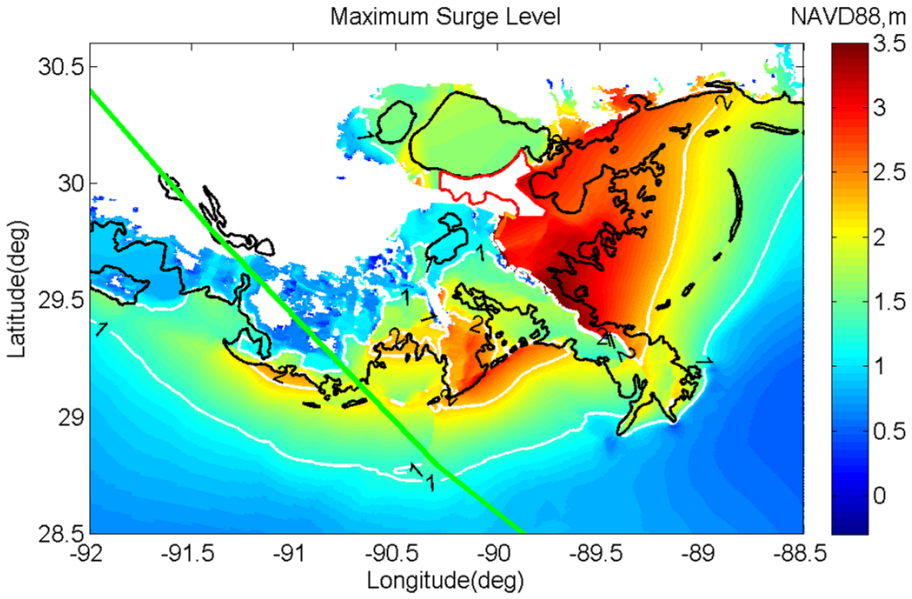

FIGURE 3.13: Modeled maximum surge level in southeastern Louisiana during the passage of Gustav

and the R-square of the best fit of peak surge at all the stations were 0.92 and 0.85 (Figure 3.14), respectively.

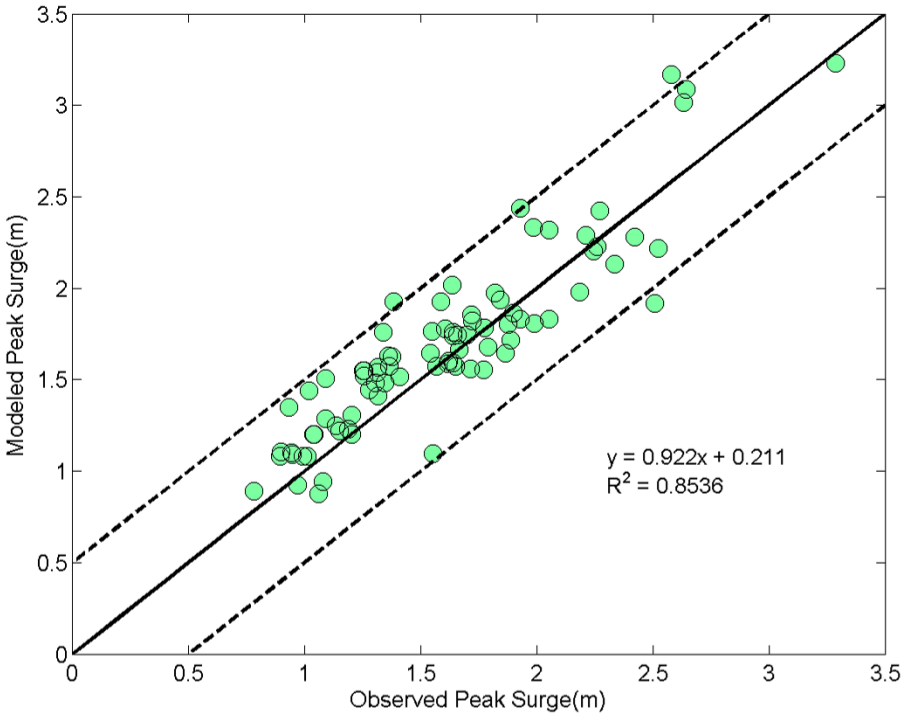

FIGURE 3.14: Comparison of peak surges with the data records at the CRMS stations

TABLE 3.1: The summary of errors for the modeled wave and surge time series

Dataset	Variable	#Stations	Bias	Scatter Index
NOAA tide stations (southeastern LA)	Water Level (m)	6	-0.08	0.18
NOAA tide stations (total)	Water Level (m)	11	-0.06	0.35
Kennedy et al.[2010]	Water Level (m)	6	0.07	0.28
Kennedy et al.[2010]	Wave Height (m)	5	0.10	0.27
Kennedy et al.[2010]	Peak Wave Period(s)	6	1.07	0.41

3.7 Summary

An accurate prediction of storm surge and hurricane waves is imperative to the simulation of hurricane-induced sediment transport. In this chapter, a fully coupled surge model and wave model for Hurricane Gustav (2008) were developed using Delft3D. At offshore, the wave predictions agreed well with the observations at the selected NDBC wave gauges in the Gulf

of Mexico, which validated the stand-alone wave model and the hurricane wind field. In the nearshore region, surge and wave interaction became important, and the coupled surge and wave models predicted surge level fairly well in comparison with water level measurements from various sources, which covered a large area from the coastline to inland marshes. Measurements for nearshore waves were also available at limited number of wave gauges. The modeled wave heights and wave periods were in reasonable agreement with the observations.

The good accuracy in the surge and wave predictions gave us confidence in applying the coupled surge model and wave model to simulating sediment transport during Gustav in the following chapters.

CHAPTER 4 GUSTAV-INDUCED WETLAND-BAY AND BAY-SHELF SEDIMENT FLUXES

4.1 Introduction

It is widely recognized that intense hurricanes play a key role in shaping the morphology of coastal wetlands. Over decades, sediment accretion was observed on the marsh surface after hurricanes and storms, and it was believed to help the marsh to maintain the elevation and keep pace with sea level rise and subsidence (Morgan et al., 1958; Chamberlain, 1959; Roberts et al., 1987; Rejmanek et al., 1988; Reed, 1989; Nyman et al., 1995; Cahoon et al., 1995; Turner et al., 2006; McKee and Cherry, 2009). On the other hand, hurricanes may have negative effects by eroding the edge of marshes and expanding the existing ponds and small lakes (McGee et al., 2006; Morton and Barras, 2011). In order to clear the doubts on the net effect of hurricanes on coastal morphodynamics, identify the major source of sediment supplies to the coastal wetlands and take proper actions to maintain the sediment balance, a better understanding of the effect of hurricanes on the large-scale sediment budget of a coastal system is highly desired.

Considerable efforts have been devoted to quantifying the contribution of hurricane-induced sedimentation. Turner et al. (2006) estimated that Hurricane Katrina and Rita brought in 131 million metric tons (MMT) of mineral material to the Louisiana coast. Tweel and Turner (2014) developed a statistical model based on deposition data observed from Hurricanes Katrina (2005), Rita (2005) and Gustav (2008), and estimated that the annual deposition on the marsh surface from category 1 or higher hurricanes was 5.6 MMT. By chronostratigraphic assessment of 27 cores taken within the Breton Sound Basin, Smith et al. (2015) suggested the annual sediment accumulation caused by category 3 or higher hurricanes is about 0.05 MMT in that area. Besides the inconsistent results from different methods, some obvious limitations exist in the above-mentioned studies: Firstly, the spatial distribution of deposition was predicted by interpolation of a limited number of coring stations, and thus the effects of local bathymetry and human-made

structures were not taken into account. Secondly, sediment deposition inland is often associated with both erosion and deposition on wetlands, while most measurements didn't include the temporal variation of the marsh surface elevation and thus could not reproduce the erosional history.

Another question of practical interest is the source of the observed deposition on marshes. Whether it was a result of onshore transport of marine material originating from the inner continental shelf or it came from redistribution of local sediment, implies different mechanisms of sediment balance and could lead to different wetland restoration strategies. A popular hypothesis is that most deposition originates from the shallow lakes and open bays, where relatively large waves suspend sediment and the raising water move them to the marsh surface (Chamberlain, 1959; Roberts et al., 1987; Rejmanek et al., 1988; Reed, 1989). A complete answer to this question requires a further study to identify the pathway of sediment transport in a typical coastal environment during an extreme event, and the answer is likely to depend on sediment properties, vegetation coverage, and many other local environmental factors.

Numerical models have been applied to simulate large-scale hydrodynamics, sediment transport and morphological changes for coastal Louisiana under hurricane conditions. Xu et al. (2016) developed a three-dimensional sediment transport model based on the Regional Ocean Modeling System (ROMS) to study the seabed erosion and deposition after Katrina and Rita on the Louisiana-Texas continental shelf. Freeman et al. (2015) used MIKE21/MIKE 3 to hindcast the spatial pattern of accretion/erosion at Sister Lake during Hurricane Rita. However, little has been done to model the sediment transport and morphological processes in the entire continental shelf, coastal bay and lakes and wetlands system, and to quantify the sediment exchange of shelf-bay and bay-wetland borders. As a first attempt, Liu et al. (2015) developed a coupled modeling system based on Delft3D, including wind, surge, waves and sediment processes for the Louisiana coast.

In this chapter, we follow the modeling framework in Liu et al. (2015) and apply the model to study the short-term impact of a hurricane on sediment dynamics on coastal wetlands. Specific objectives include: (1) estimate the net deposition on the coastal wetlands during a major hurricane event, and (2) identify the major source of the deposited sediment on the wetland surface. This chapter is organized as following: The sediment transport model in briefly introduced in Section 4.2; The model setup, sediment properties and the coupling of the sediment transport model with the flow model and the wave model are described in Section 4.3; The predicted sedimentation on coastal wetlands and other results are presented in Section 4.4; A sensitivity analysis and uncertainty analysis for model parameters in sediment properties are conducted in Section 4.5; Finally we summarize this chapter in Section 4.6.

4.2 Modeling Sediment Transport in Delft3D

4.2.1 Governing equations

In Delft3D, suspended sediment transport is modeled by an advection-diffusion equation for sediment concentration:

$$\frac{\partial c}{\partial t}+\frac{\partial uc}{\partial x}+\frac{\partial vc}{\partial y}+\frac{\partial (w-w_s)c}{\partial z}=\frac{\partial}{\partial x}\left(\epsilon_{s,x}\frac{\partial c}{\partial x}\right)+\frac{\partial}{\partial y}\left(\epsilon_{s,y}\frac{\partial c}{\partial y}\right)+\frac{\partial}{\partial z}\left(\epsilon_{s,z}\frac{\partial c}{\partial z}\right) \quad (4.1)$$

where c is mass concentration of sediment, u, v and w are flow velocity in x, y and z directions, $\epsilon_{s,x}$, $\epsilon_{s,y}$, $\epsilon_{s,z}$ are eddy diffusivity of sediment, and w_s is (hindered) settling velocity of sediment. Flow velocities are obtained from hydrodynamic computation. Eddy diffusivity is calculated from eddy viscosity in the manner:

$$\epsilon_{3D}=\frac{\mu_{3D}}{\sigma_c} \quad (4.2)$$

where σ_c is the Prandtl-Schmidt number, whose value depends on the substance. In Delft3D, four turbulence closure models are available to determine ϵ_{3D} and μ, namely constant coefficient, Algebraic Eddy viscosity Model (AEM), $k-L$ turbulence closure model and $k-\epsilon$ turbulence closure model. The first method allows users to specify a constant value for ϵ_{3D} and

μ. And the other three methods are based on the concept of eddy viscosity which relates to a characteristic length scale and kinetic energy scale:

$$\mu_{3D} = c_\mu L\sqrt{k} \tag{4.3}$$

with L being the mixing length, k the turbulent kinetic enrgy, and c_μ a constant determined by calibration.

4.2.2 Settling velocity

The settling velocity of non-cohesive sediment fraction (sand) is calculated from sediment diameter using the formula by van Rijn (1993):

$$w_{s,0} = \begin{cases} \dfrac{(s-1)gD_s}{18\mu} & \text{if } 65\,\text{um} < D_s \leq 100\,\text{um} \\ \dfrac{10\mu}{D_s}\left(\sqrt{1+\dfrac{0.01(s-1)gD_s^3}{\mu^2}}-1\right) & \text{if } 100\,\text{um} < D_s \leq 1000\,\text{um} \\ 1.1\sqrt{(s-1)gD_s} & \text{if } 1000\,\text{um} < D_s \end{cases}$$

where

s is sediment density relative to water density ρ_s/ρ_w;

D_s is representative diameter;

μ is kinematic viscosity coefficient of water [m^2/s].

For mud, settling velocity is provided by users. When the sediment concentration is too high, the settling velocity of each individual particle is reduced due to the presence of other particles. This effect is modeled as hindered settling by Richardson and Zaki (1954):

$$w_s = \left(1 - \frac{c_s^{tot}}{C_{soil}}\right) w_{s,0} \tag{4.4}$$

with C_{soil} being the user-specified reference concentration, c_s^{tot} the total mass concentration of all the sediment fractions, and $w_{s,0}$ the settling velocity without hindered effect.

4.2.3 Erosion and deposition

For sandy fractions, erosion and deposition fluxes are evaluated at the so-called kmx-layer, which is defined entirely above van Rijn's reference height (van Rijn, 1993). Deposition flux is given by

$$D = w_s c_{kmx(bot)} \tag{4.5}$$

where $c_{kmx(bot)}$ is the sediment concentration at the bottom of the kmx-layer. Erosion flux comes from the upward diffusion of sediment:

$$E = \epsilon_s \frac{\partial c}{\partial z} \tag{4.6}$$

where ϵ_s and $\frac{\partial c}{\partial z}$ are also evaluated at the bottom of the kmx-layer.

For cohesive sediment fractions, erosion and deposition are calculated using the Partheniades-Krone formulations (Partheniades, 1965) which depend on the calculated bed shear stress relative to the critical shear stress for deposition and erosion:

$$E = M \times S\left(\tau_{cw}, \tau_{cr,e}\right) \tag{4.7}$$

$$D = w_s \times c_b \times S\left(\tau_{cw}, \tau_{cr,d}\right) \tag{4.8}$$

$$c_b = c\left(z = \frac{\Delta z_b}{2}, t\right) \tag{4.9}$$

where:

E represents erosion flux [kg m^{-2}s^{-1}];

M represents user-defined erosin parameter [kg m^{-2}s^{-1}];

$S(\tau_{cw}, \tau_{cr,e})$ is erosion step function which is equal to $\left(\frac{\tau_{cw}}{\tau_{cr,e}} - 1\right)$ when $\tau_{cw} > \tau_{cr,e}$, and 0 when $\tau_{cw} \leq \tau_{cr,e}$;

D is deposition flux [kg $m^{-2}s^{-1}$];

w_s is fall velocity [m/s];

c_b is average sediment concentration in the near bottom computational layer;

$S(\tau_{cw}, \tau_{cr,d})$ is deposition step function which is equal to $\left(1 - \frac{\tau_{cw}}{\tau_{cr,d}}\right)$ when $\tau_{cw} < \tau_{cr,d}$, and 0 when $\tau_{cw} \geq \tau_{cr,e}$;

τ_{cw} is the maximum bed shear stress due to current and waves;

$\tau_{cr,e}/\tau_{cr,d}$ is the user-defined critical erosion/deposition shear stress.

4.3 Model Setup

4.3.1 Sediment properties

Two sediment classes were considered in our model: mud and sand. The initial composition of mud and sand on the bed was extracted from the usSEABED data (Williams et al., 2006). Over 47,000 historical surficial grain-size data points are available on the Texas-Louisianan shelf, most of which contain more than 80% of mud (Figure 4.1). These data were interpolated to generate the initial mud and sand fraction in the domain (Figure 4.2). An initial sediment layer of five meters was assumed in the model. This thick bed layer was used to prevent the removal of the sediment reservoir in sensitivity tests. When multiple sediment fractions were present at the same location, a uniform bed layer with well-mixed sediment was assumed in the model. Water temperature and salinity could affect mud flocculation and the vertical distribution of sand, but considering the spatial variation and stratification of temperature and salinity during a hurricane event could be limited, the temperature or salinity-dependency of sediment properties was not taken into account here. The sediment concentration in the water column was assumed to be zero at the beginning of the simulation. Neumann-type boundary conditions were imposed for both mud and sand at the open boundary.

TABLE 4.1: The median diameter (D_{50}) of sand, the settling velocity (ω_s), critical shear stress (τ_{crit}) and erosion rate (E) of mud in literature

Literature	Study Site	Models	D_{50}(mm)	Settling Velocity (mm/s)	Critical Shear Stress (Pa)	Erosion Rate (10^{-4} kg/m^2/s)
Edmonds & Slingerland (2010)	Atchafalaya Bay	Delft3D	0.125, 0.225, 0.350	/	0.1 2.0	/
Leadon (2015)	Barrier Islands within Barataria	SBEACH	0.10∼ 0.15	/	/	/
Nardin and Edmonds (2014)	Wax Lake Delta	Delft3D	0.10	/	0.25	/
Xu et al. (2011)	Texas-LA Continental shelf	ROMS	/	0.1, 1.0	0.03, 0.11	0.5
Xu et al. (2016)	Texas-LA Continental shelf	ROMS	0.063, 0.250	0.1, 1.0	0.11, 0.13	2.0, 3.0
Freeman et al. (2015)	Sister Lake	MIKE 21/3	/	/	0.15	/

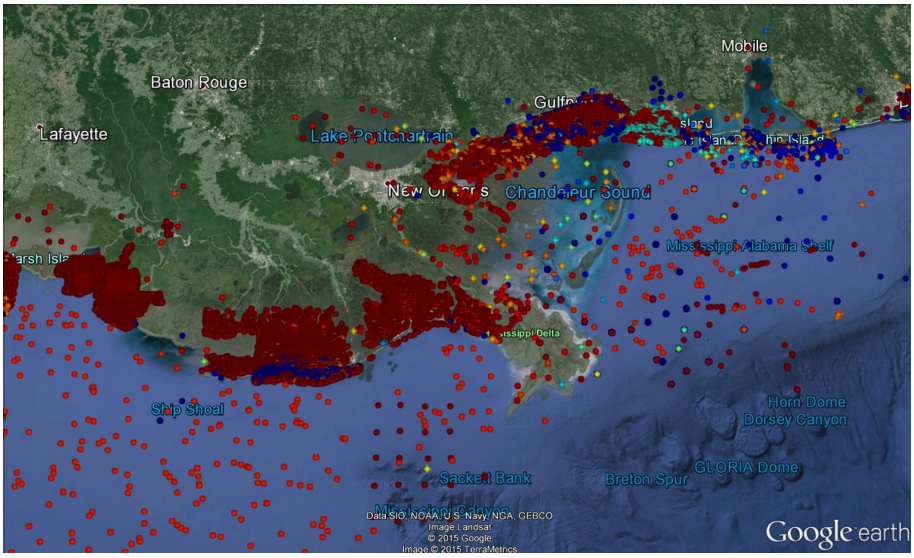

FIGURE 4.1: Data points near the coast of Louisiana from the usSEABED dataset (red indicates high mud composition, and blue indicates high sand composition)

TABLE 4.2: Sediment properties in the sediment transport and morphology model

Sediment Class	Origin	Settling Velocity(mm/s)	Critical Shear Stress (Pa)	Erosion Rate (10^{-4} kg /m^2 /s)
Mud	sea	0.1, 0.25, 1.0	0.05, 0.1, 0.2	0.5, 1.0, 5.0
	estuary		0.05, 0.1, 0.2	
	wetland		0.5, 1.0, 2.0	
Sand	sea	Determined by D_{50}=0.14mm	NA	NA
	estuary		NA	NA

The following parameters are important in simulating erosional and depositional processes in our model: the median diameter (D_{50}) of sand, the settling velocity (ω_s), critical shear stress (τ_{crit}) and erosion rate (E) of mud. To determine a reasonable range of these parameters, we did a literature search on numerical simulations of sediment transport in coastal Louisiana (Edmonds and Slingerland, 2010; Leadon, 2015; Xu et al., 2011, 2016; Freeman et al., 2015) and the values used by those studies are listed in Table 4.1. In addition, Wright et al. (1997) used a critical shear stress of 0.1 Pa for a sediment transport study on the continental shelf to the south of Terrebonne Bay. Based on these studies, the median diameter of sand was set to be 0.14 mm according to a study on barrier islands in the Barataria Basin (Leadon, 2015). The density of sand was 2650 kg/m^3. For mud, we chose three levels of settling velocity at 0.1, 0.25, and 1.0 mm /sec and three levels of erosion rate at 0.5, 1.0, and 5.0×10^4 kg /m^2 /s (summarized in Table 4.2). Thus three sets of settling velocity and three sets of erosion rate yield a total of nine model runs. A baseline model run with optimum parameters will be chosen based on a best agreement of post-hurricane deposition with the measurements in Tweel and Turner (2012) in Section 4.4.2. The critical shear stress was 0.1 Pa for mud in sea and coastal bays, which was consistent with other numerical studies in the same region (Xu et al., 2016; Freeman et al., 2015), and 1.0 Pa for vegetated land to account for the fact that vegetation roots can strengthen the soil layer and enhance its resistance to erosion. The impact of the uncertainty of critical shear stress will be discussed in Section 4.5.

In Delft3D, sediment calculation is performed when local water depth is deeper than a certain threshold. According to our experiments, this threshold must be equal to or greater than the minimum depth for wetting and drying, otherwise instability would occur at the front of the wetting line. Here, we set the minimum depth for sediment calculation to be 0.1 m and the threshold depth for wetting and drying to be 0.1 m.

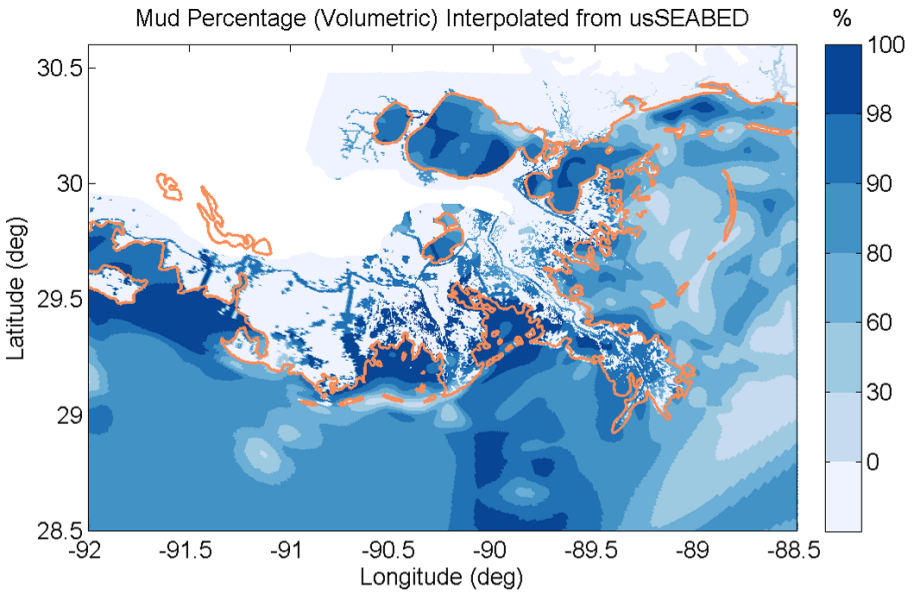

FIGURE 4.2: The initial bed mud fraction interpolated from data points in usSEABED (Williams et al., 2006)

4.3.2 Coupling the sediment transport with the hydrodynamic model

In this study, the hurricane wind, surge, wave, and sediment transport processes were integrated into a coupled modeling system. The flow module provided surge level and current velocity to the wave computation. The wave module computed the radiation stresses that would further elevates surge level. The computed flow velocity, diffusivity and bed shear stress from both modules served as the driving force for sediment erosion and redistribution in the sediment transport module (Figure 4.3). Moreover, the coupled modeling system was running on the same mesh, which avoided interpolation error between heterogeneous model meshes. For Hurricane Gustav, the simulation time was eight days from August 28 to September 5, 2008. The time

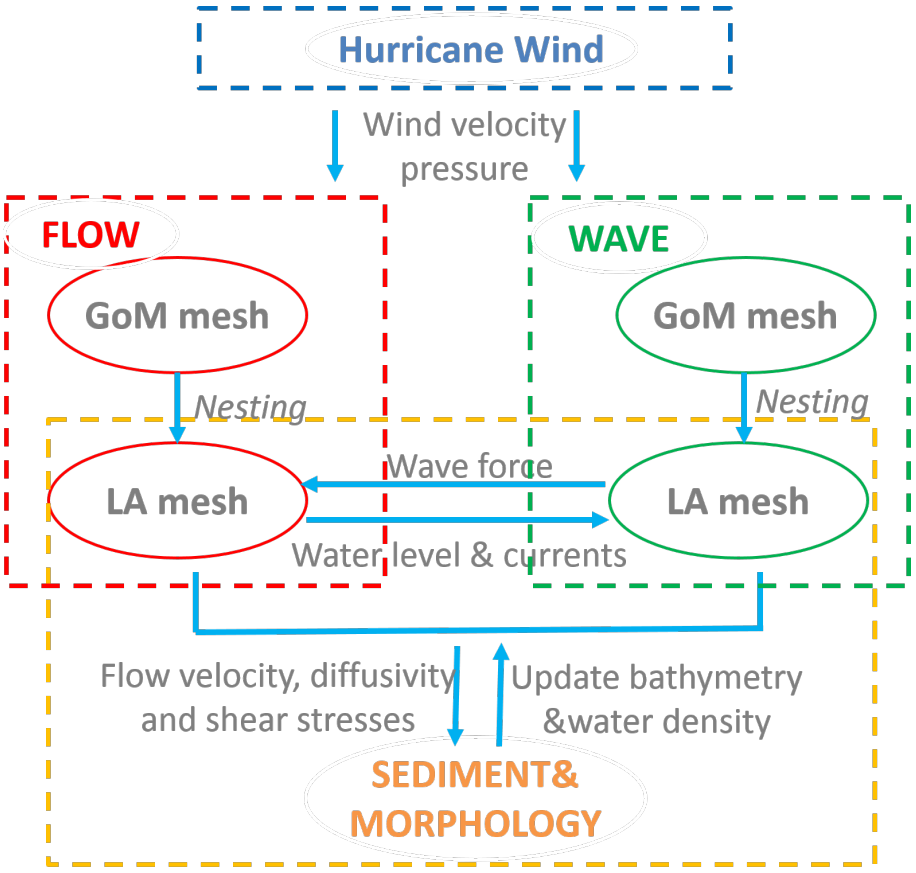

FIGURE 4.3: Data flow between different modules and mesh layers in the integrated modeling system

step for the storm surge and sediment simulation was 0.5 minute, while the wave model ran in the non-stationary mode with a 60-minute interval. The coupling interval was 60 minutes. Twelve-hour spin-up time was set in the sediment transport model before erosion or deposition took place on the bed sediment layer.

4.4 Model Results

4.4.1 Hydrodynamic forcing and sediment suspension

The modeled depth-averaged current velocity is presented in Figure 4.4. As the center of Hurricane Gustav was approaching the shoreline, the wind direction in the Terrebonne-Barataria area changed from easterly to southerly (Figure 3.10). A strong current ($>$1.0 m/s) persisted in longshore direction until 16:00, Sep 01, and the maximum current speed ($\sim$4 m/s) occurred immediately to the east of Gustavs landfall location. Due to the steep change of bathymetry and the blocking of barrier islands at the inlets of estuaries, the currents inside Terrebonne Bay and Barataria Bay were much weaker than that on the adjacent continental shelf, and the depth-averaged velocity inside the bay was 1 to 2 m/s during the hurricane landfall. It is noticeable that the rise of the onshore current velocity inside Barataria Bay happened earlier than that in Terrebonne Bay. This could be explained by the fact that the inlet of Barataria Bay aligned with the direction of the longshore current, and thus Barataria Bay was relatively easier to be affected by the circulation in the continental shelf.

The growing current and hurricane waves brought up the bed shear stress in the same region (Figure 4.5). On continental shelf, model results showed that the maximum bed stress was 8 to 10 Pa, while in the estuaries and the marsh, the maximum bed shear stress could exceed 20 Pa.

The significant increase of bed shear stress had the potential to suspend the sediments on the bed of inner shelf as well as estuaries. Storm surge and flooding current carried them further onshore. Although two sediment classes, mud and sand, were both available in the model,

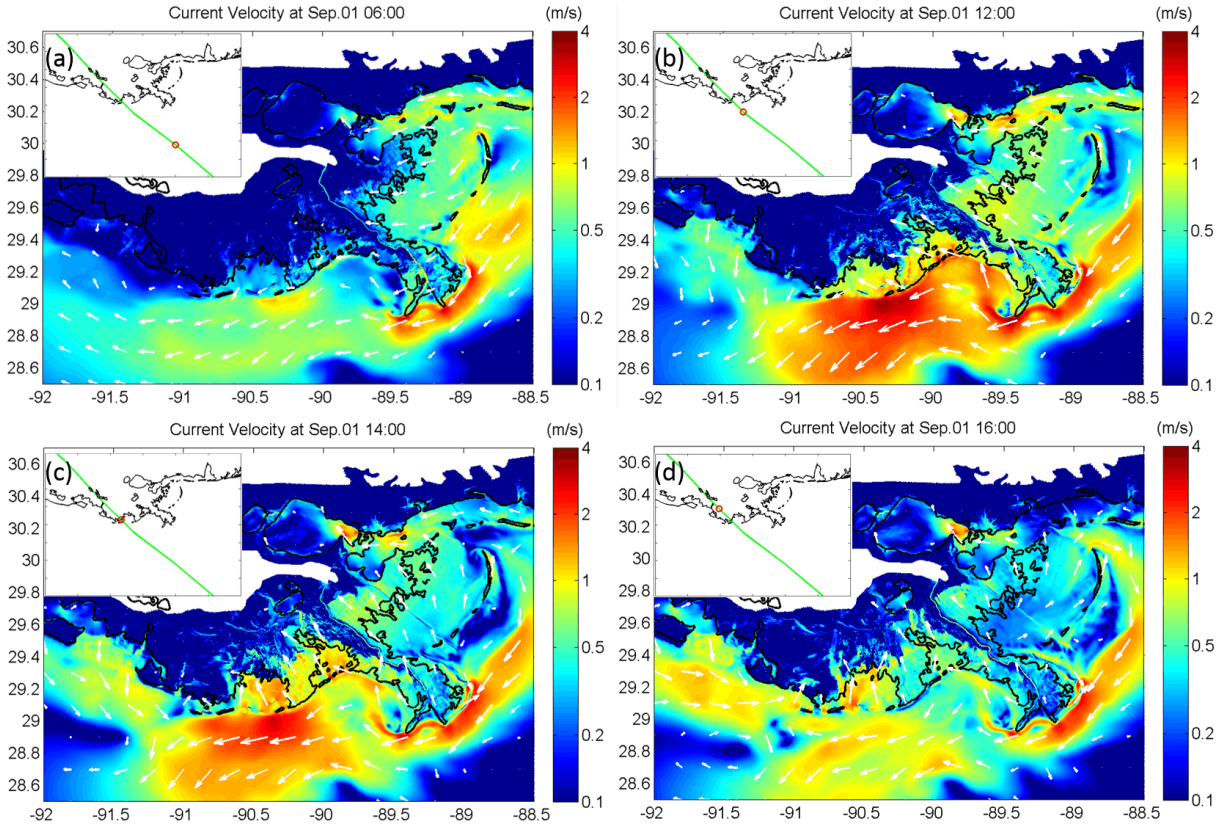

FIGURE 4.4: The modeled depth-averaged current velocity before and after the landfall of hurricane Gustav (2008) (green lines: hurricane track; red circles: hurricane center relative to the shoreline): (a) 06:00 UTC, Sep 01, or approximately 8 hours before landfall, (b) 12:00 UTC, Sep 01, or approximately 2 hours before landfall, (c) 14:00 UTC, Sep 01, or approximately landfall, and (d) 16:00 UTC, Sep 01, or approximately 2 hours after landfall.

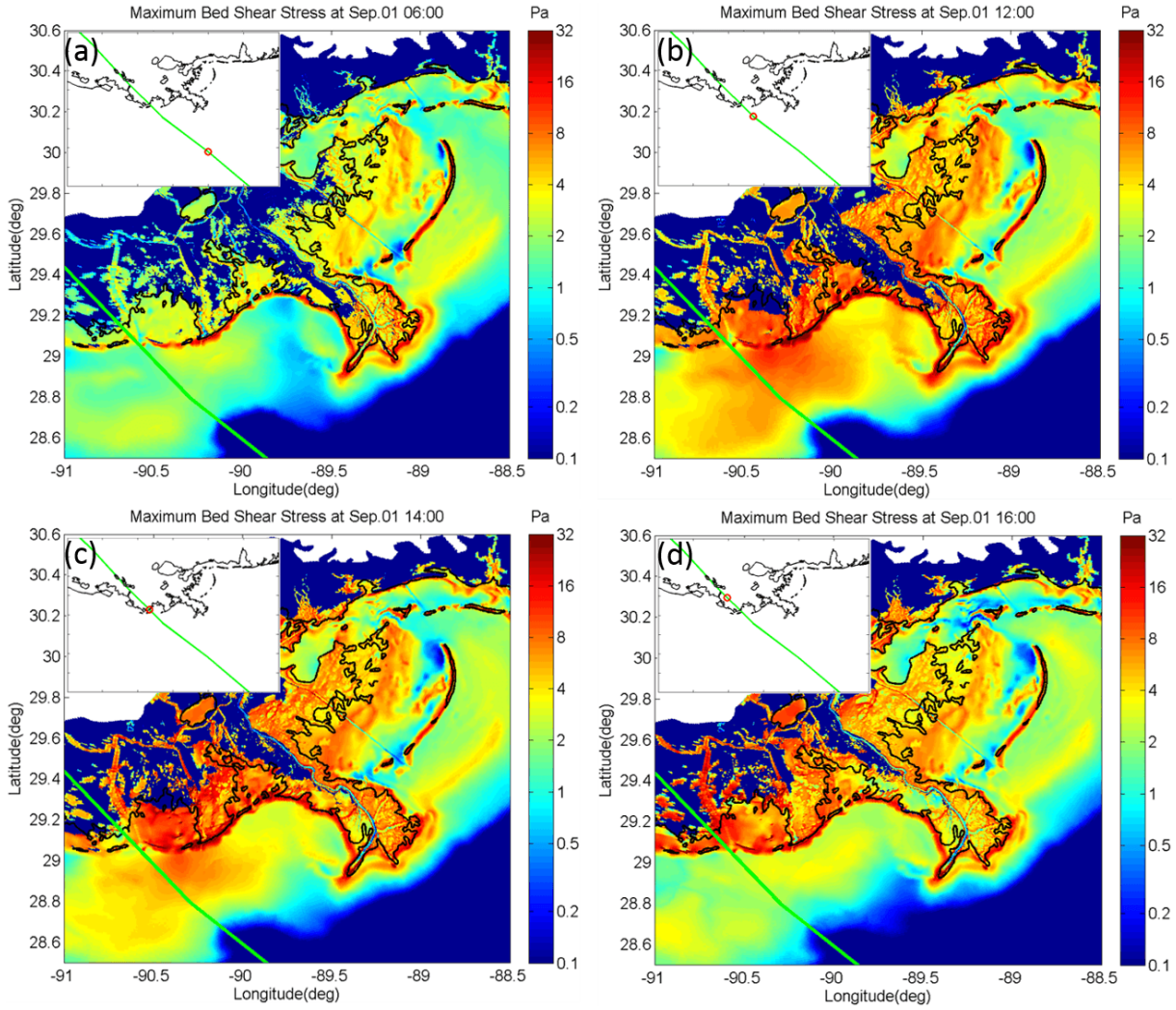

FIGURE 4.5: The modeled bed shear stress before and after the landfall of Hurricane Gustav (2008) (green lines: hurricane track; red circles: hurricane center relative to the shoreline): Times (a)-(d) are as in 4.4

the suspension and transport of these two sediment classes were not equal. During Hurricane Gustav, the maximum concentration of mud in the water column exceeded the concentration of sand by at least an order of magnitude (Figure 4.6). Given the assumption that the initial sediment concentration in the water column was much smaller than the suspended sediment concentration, we can expect the hurricane-induced deposition was mainly made up of muddy material.

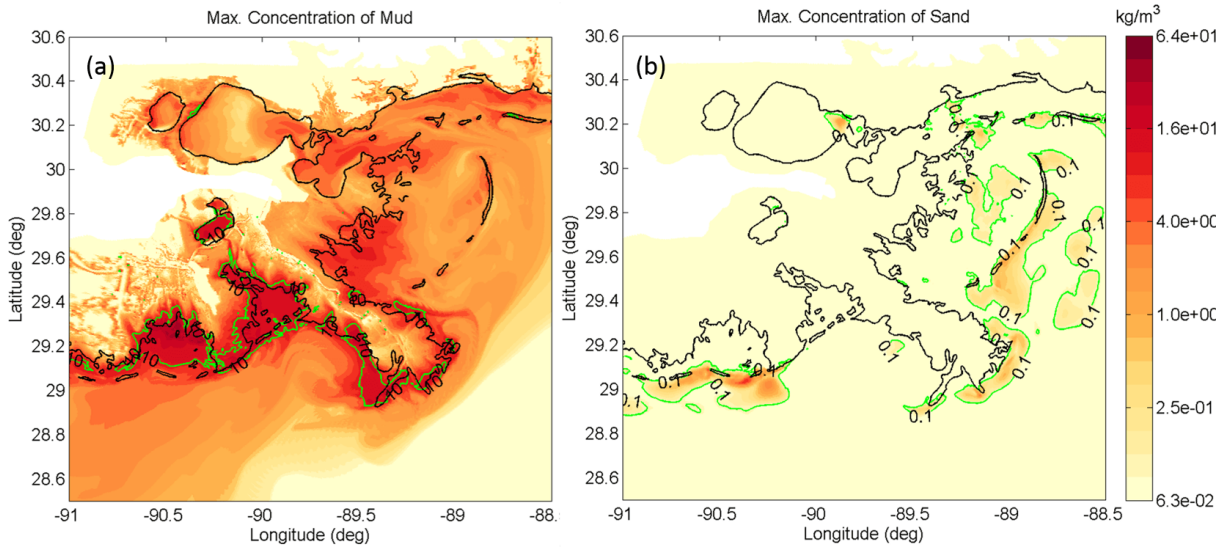

FIGURE 4.6: Maximum suspended sediment concentration of mud with $10\,\mathrm{kg/m^3}$concentration contour lines (a), and sand with $0.1\,\mathrm{kg/m^3}$ concentration contour lines (b) during Gustav: with a settling velocity of 0.25 mm/s, a critical shear stress of 0.1 Pa, and an erosion rate of $0.5 \times 10^{-4}\,\mathrm{kg/m^2/s}$

4.4.2 Post-hurricane accretion

Field survey was conducted following the landfall of Gustav (Tweel and Turner, 2012), and the thickness of surface deposition on the coastal wetlands were measured at 110 locations in Barataria Bay, Terrebonne Bay, and a small part of Breton Sound (Figure 3.9). The reported maximum accretion was $7.46\,\mathrm{g}\,/\mathrm{m^2}$ (Tweel and Turner, 2012). This dataset was compared with the modeled deposition on the wetlands to calibrate our sediment transport model.

As pointed out by Xu et al. (2016), two types of deposition should be distinguished: the net deposition

$$DEP_n = z_{end} - z_{bgn} \tag{4.10}$$

is simply the arithmetical difference between the bed elevation after and before the hurricane; and the post-hurricane deposit

$$DEP_p = z_{end} - z_{min} \tag{4.11}$$

is the amount of deposition above the deepest cut (z_{min} in Figure 4.7). The net deposition is not necessarily the same as post-hurricane deposit as illustrated in Figure 4.7. Since Tweel and Turner (2012) measured the thickness of a fresh event layer without records of pre-hurricane elevation, it is the post-hurricane deposit, instead of the net deposit, from the model that corresponds to the measurements.

We also note that there was a large variation in the observed accretion, even at locations very close to each other. This is not surprising given the fact that the topography on the marsh surface can be complex with various local features. In our model, the mesh resolution was limited and not sufficient to resolve the small-scale features such as creeks and small channels. Therefore, instead of a point-by-point comparison, the mean accretions at the measured sites within Terrebonne Bay and Barataria Bay (the division of basins was plotted in Figure 4.8) and the standard errors of the means were computed and validated against the corresponding mean value from the field measurement.

The mean accretions and standard errors within each basin from different sediment parameters are presented in Table 4.3. Among all the experimental runs, R11, R12, R22, R13 and R23 produced spatial-averaged accretion in the same order of magnitude as the observation. The overall error of each experimental run was evaluated as the following

$$\delta = \frac{\delta_1 n_1 + \delta_2 n_2}{n_1 + n_2} \tag{4.12}$$

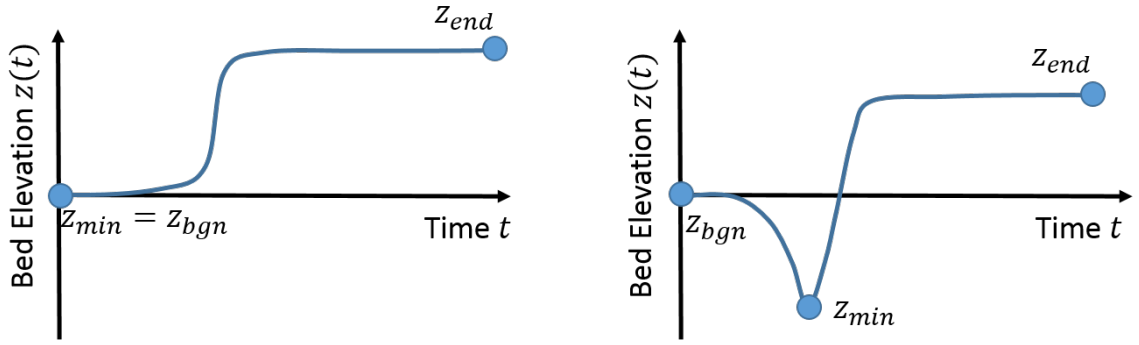

FIGURE 4.7: The conceptual diagram of two types of deposition, modified after Xu et al. (2015) (z_{bgn}/z_{end}: the bed elevation at the beginning/end of the hurricane event; z_{min}: the minimum bed level ever experienced during the hurricane)

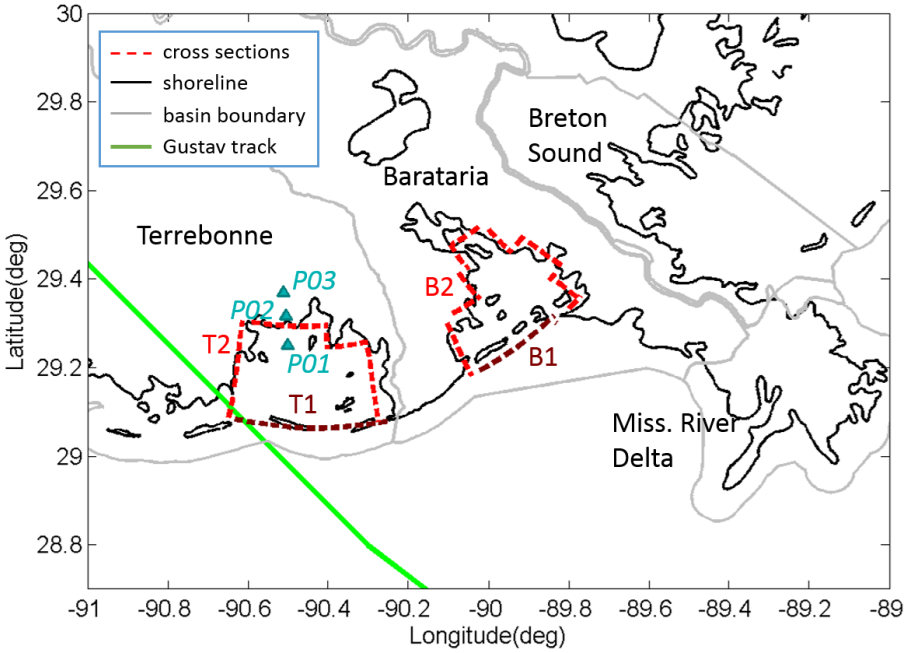

FIGURE 4.8: The locations of observation points (P02/P02/P03), the cross-sections in Terrebonne Bay (T1 and T2) and Barataria Bay (B1 and B2), and the basin boundaries

TABLE 4.3: The sediment parameters used in numerical experiments and the mean accretion and standard error from each experimental run

	Erosion Rate (10^{-4} kg/m^2/s)	Settling Vel. (mm/s)	Critical Shear Stress (Pa): water/land	Mean Accretion (cm)		Standard Error (cm)		Overall Error (cm)
				Ter.	Ber.	Ter.	Ber.	
obs.				2.93	3.19	0.31	0.63	0.00
R11	0.5	0.1	0.1/1.0	6.62	3.57	0.55	0.43	2.19
R21	1.0	0.1	0.1/1.0	12.3	7.30	1.05	0.85	6.82
R31	5.0	0.1	0.1/1.0	46.1	28.2	4.46	4.09	33.8
R12	0.5	0.25	0.1/1.0	4.29	2.57	0.43	0.40	0.51
R22	1.0	0.25	0.1/1.0	8.31	5.29	0.83	0.77	3.81
R32	5.0	0.25	0.1/1.0	43.3	28.6	3.98	4.44	32.4
R13	0.5	1.0	0.1/1.0	1.17	0.89	0.20	0.23	-1.88
R23	1.0	1.0	0.1/1.0	2.48	1.84	0.36	0.46	-0.78
R33	5.0	1.0	0.1/1.0	12.2	13.4	1.70	2.80	9.17
X2	0.5	0.25	0.05/0.5	8.39	5.36	0.83	0.77	3.88
X3	0.5	0.25	0.2/2.0	2.13	1.25	0.23	0.21	-1.21

where δ_1/ δ_2 is the absolute error of mean accretion for the Terrebonne/Barataria Basin, and n_1/n_2 is the number of points within the Terrebonne/Barataria Basin. Since R12 has a minimum δ within our experiments, R12 with an erosion parameter of 0.5×10^{-4} kg /m^2 /s and a settling velocity of 0.25 mm /s of mud was defined as the baseline model and the following discussion of model results were based on the settings in R12. We also want to point out R12 is not likely to be the only parameter combination which could possibly generate a good match with the observation. But since the mean accretion within these three basins have been very close to observations, we did not go further to pursue a perfect match in this sense. Instead, how the uncertainty in these parameters could affect our interpretation of the results and final conclusions will be discussed in section 4.5.1.

A side-by-side comparison of modeled deposition with measurements in Tweel and Turner (2012) was given in Figure 4.9. The model not only produced a basin-averaged post-hurricane deposition close to the measurements (blue bars and green bars in Figure 4.9), but also revealed that the net change of the sediment layer thickness at the selected survey locations could be

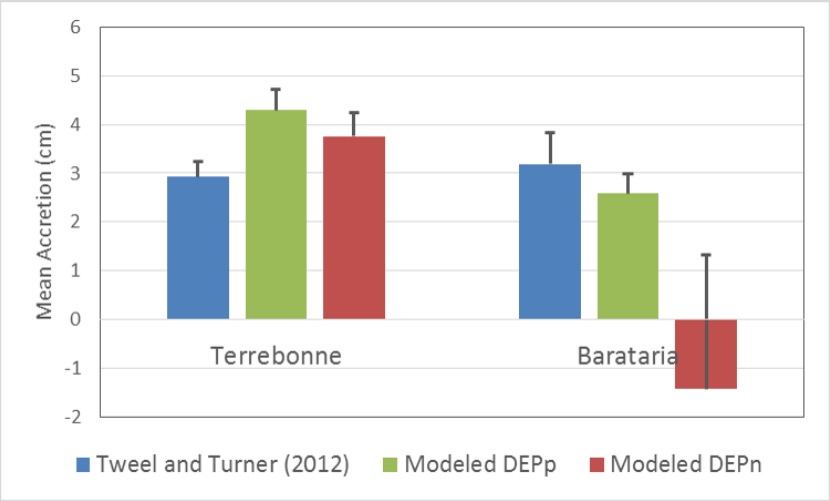

FIGURE 4.9: Comparison of the modeled post-hurricane deposition DEP_p (Equation 4.10) and net deposition DEP_n (Equation 4.11) with measurements in Tweel and Turner (2012)

considerably different from the fresh deposition measured after the hurricane (blue bars and red bars in Figure 4.9). For instance, the net effect of Gustav was erosion for the survey locations in Barataria Bay.

To illustrate the evolution of hydrodynamic forcing and different types of morphological changes, three observation points (P01, P02 and P03 in Figure 4.8) were selected in Terrebonne Bay. They represented three types of landscape characteristics: P01 was located in the open bay, P02 was in a small water pond, and P03 was initially on dry land. The maximum significant wave height decreased from 1.2 m in the shallow bay (P01) to 0.5 m on the marsh near the bay (P03) and the current also dropped from $1.5\,$m /s to $0.4\,$m /s due to the damping effect of vegetation. The modeled high shear stress was a combined result of strong currents and large waves during the hurricane (Figure 4.10). In the shallow bay, a severe erosion of 8 cm deep was experienced prior to the deposition (P01), which indicated a significant suspension in the open bay as the hurricane was approaching onshore. On wetlands, a direct deposition was more likely to happen for two reasons: first, the vegetation enhanced the soil strength and increased resistance to erosion; and secondly, the erosion was filled almost immediately by the deposition.

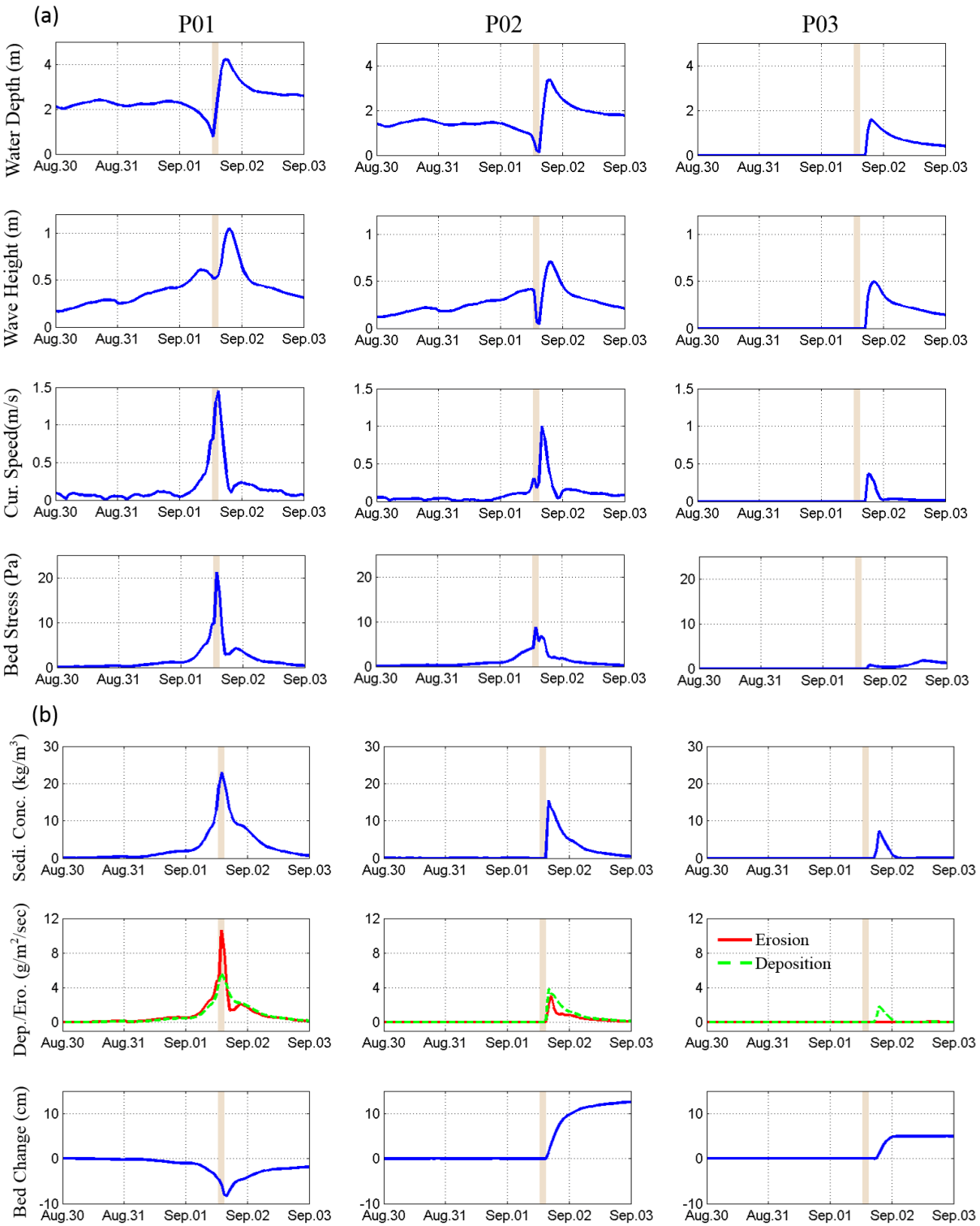

FIGURE 4.10: The modeled hydrodynamics processes (a) and morphological processes (b) at P01/P02/P03 (defined in Figure 4.8)in Terrebonne Bay: from R12

4.4.3 Deposition on wetlands and the source of sediment

TABLE 4.4: The definition of cross-sections

Cross-section ID	Offshore Side	Onshore Side
B1	Gulf of Mexico	Barataria Bay
B2	Barataria Bay	Wetlands in Barataria
T1	Gulf of Mexico	Terrebonne Bay
T2	Terrebonne Bay	Wetlands in Terrebonne

To evaluate the sediment exchange among the shelf, the estuaries, and coastal wetlands, four cross-sections were defined around Barataria Bay (B1, B2) and Terrebonne Bay (T1, T2) (Figure 4.8). B1 and T1 were located between the continental shelf and the coastal bays, while B2 and T2 were between the estuaries and the coastal wetlands (details in Table 4.4).

Based on our experiments, the suspension and transport of sand was much less than that of mud. Therefore, the redistribution of sediment under hurricane forcing mainly occurred to mud on the Louisiana coast. To conveniently track the source of deposition, three sediment categories were further distinguished according to their origins: sediment originating from the shelf, from the estuaries, and from wetlands. As a result, the time history of total (including suspended load and bedload) sediment transport across B1/B2/T1/T2 were recorded for the three sediment groups: sediment from sea, from bay, and from wetlands. To be specific, we defined the total transport $T_i(t)$ of the i-th sediment group at one of the cross-sections B1/B2/T1/T2 to be

$$T_i(t) = \int_L S_i(x, y; t) dl \tag{4.13}$$

where $S_i(x, y; t)$ is the total sediment transport per unit length per unit time (m^2 /s) , L is the length (m) of one of the four cross-sections. T_i and S_i are both onshore positive.

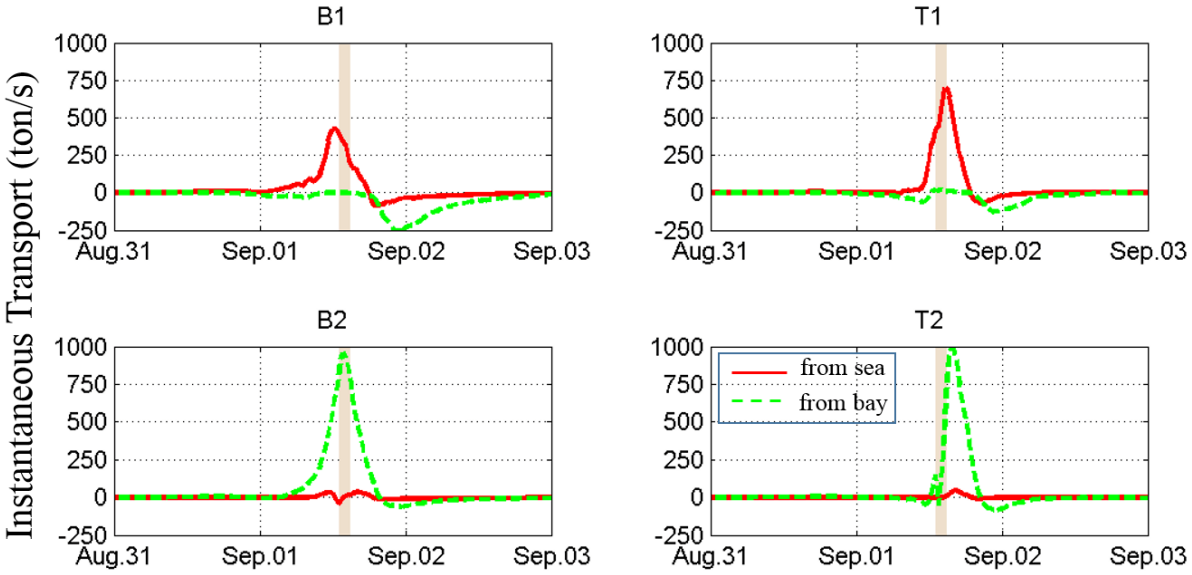

FIGURE 4.11: The time series of the total suspended transport over the defined cross-sections: from R12

In both Terrebonne Bay and Barataria Bay, we found a significant transport of marine material, from continental shelf to the estuaries (cross-section B1 and T1 in Figure 4.11). At the cross-sections between the estuaries and wetlands, however, the flux of sediment originating from the coastal bays was dominated (cross-section B2 and T2 in Figure 4.11). As the soil on vegetated wetland was hard to erode, the transport of sediment from wetlands was almost negligible compared with other two groups. We also noted that the peak of sediment transport appeared earlier in Barataria Bay than it did in Terrebonne Bay. This might be explained by the fact that the hurricane approached the coastline in a southeaster direction and the strong current and wave appeared earlier in the Barataria Basin.

The time integration of $T_i(t)$ over the hurricane event gave the net onshore sediment transport M_i over each cross-section, i.e.,

$$M_i = \int_{t_{bgn}}^{t_{end}} T_i(t)\rho_i dt \tag{4.14}$$

In our calculation, t_{bgn} was Aug/28/2008 and t_{end} was Sep/05/2008. The flux of mud from the shelf $M_{mud,sea}$ (blue arrows) and the flux of mud from the bay $M_{mud,bay}$ (yellow arrows) were evaluated at each cross-section in Figure 4.12. To calculate the total deposition on wetlands

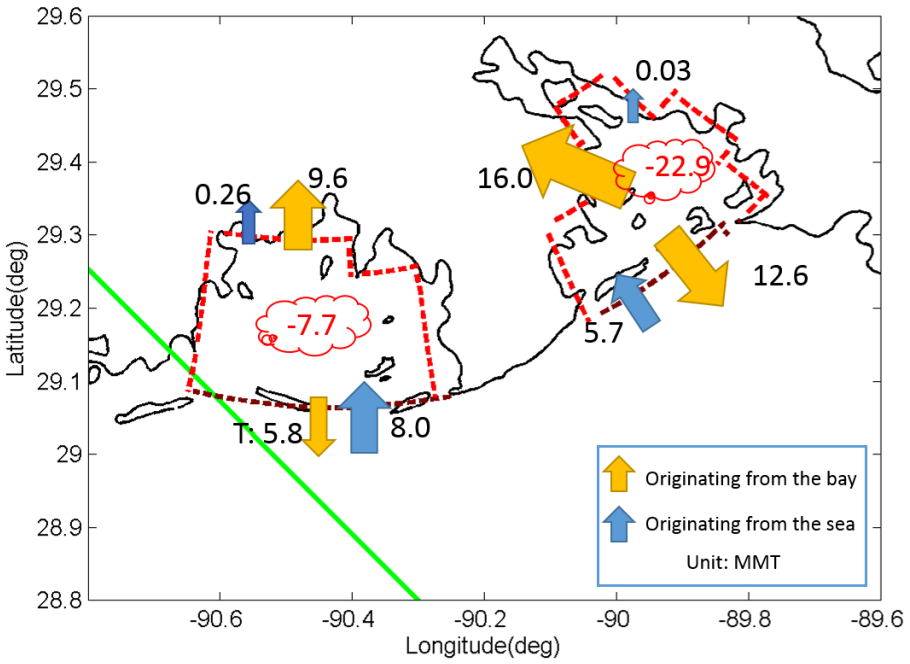

FIGURE 4.12: The net sediment transport over each cross-section during Gustav

(TDW), we can evaluate

$$TDW = M_{mud,sea} + M_{mud,bay} \tag{4.15}$$

at cross-section T2 and B2, which yielded 9.61 MMT for Terrebonne Bay and 15.98 MMT for Barataria Bay.

Similar to the observations in Figure 4.11, most sediment transport to the wetlands through B2 and T2 can be traced back to the suspended material from the bays ($M_{mud,bay}$= 9.35 MMT for Terrebonne Bay and 15.95 MMT for Barataria Bay), and only a very small fraction of deposition on wetlands came from the marine material travelling through the estuaries ($M_{mud,sea}$= 0.26 MMT through Terrebonne Bay and 0.03 MMT through Barataria Bay). As a measure of contribution of coastal bays to the total deposition on wetlands, the percentage of sedimentation originating from the bay (PB) can be calculated as

$$PB = \frac{M_{mud,bay}}{(M_{mud,bay} + M_{mud,sea})} \times 100\% \tag{4.16}$$

which gave 97.3% for Terrebonne Bay and 99.8% for Barataria Bay.

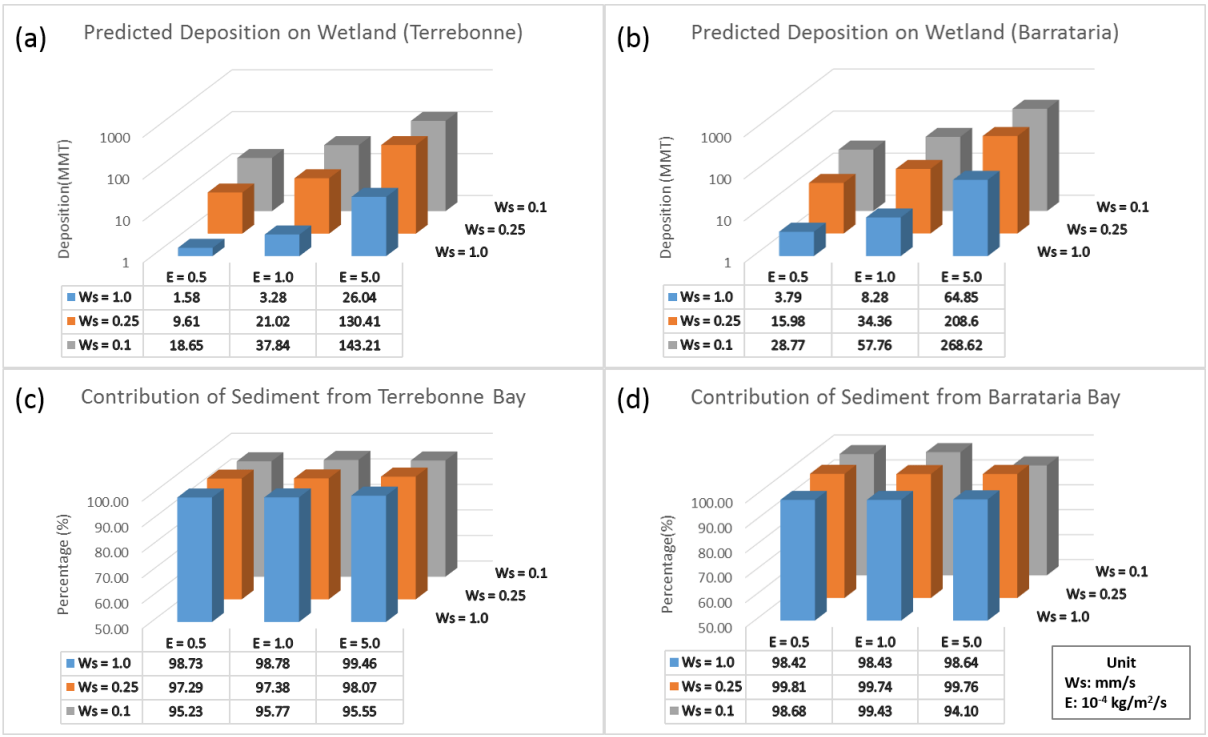

FIGURE 4.13: The predicted total deposition on wetlands (a and b) and the percentage of sediment from the coastal bays (c and d) with different settling velocity and erosion rate

4.5 Sensitivity and Uncertainty

4.5.1 Sensitivity to sediment parameters

The sensitivities of model results to settling velocity and erosion rate of mud were shown in Figure 4.13. As settling velocity increased from 0.1 to 1.0 mm /s and erosion rate increased from 0.5 to 5.0×10^4 kg /m^2 /s, TDW varied by two orders of magnitude (from 1.58 to 143.21 MMT in Terrebonne Bay, and from 3.79 to 268.62 MMT in Barataria Bay). In general, with larger erosion rate, more sediment can be suspended from the bed, and with less settling velocity, the suspended material is more likely to be transported far enough to reach the shoreline before it settles down again. Therefore, the largest TDW corresponded to the largest erosion rate and smallest settling velocity (Figure 4.13 (a) and (b)). In contrast, in terms of the contributions of coastal bays to the deposition on wetlands, PB seemed insensitive to these parameters. The calculated PB for Terrebonne Bay and Barataria Bay was in the range of 95.23- to 99.46%

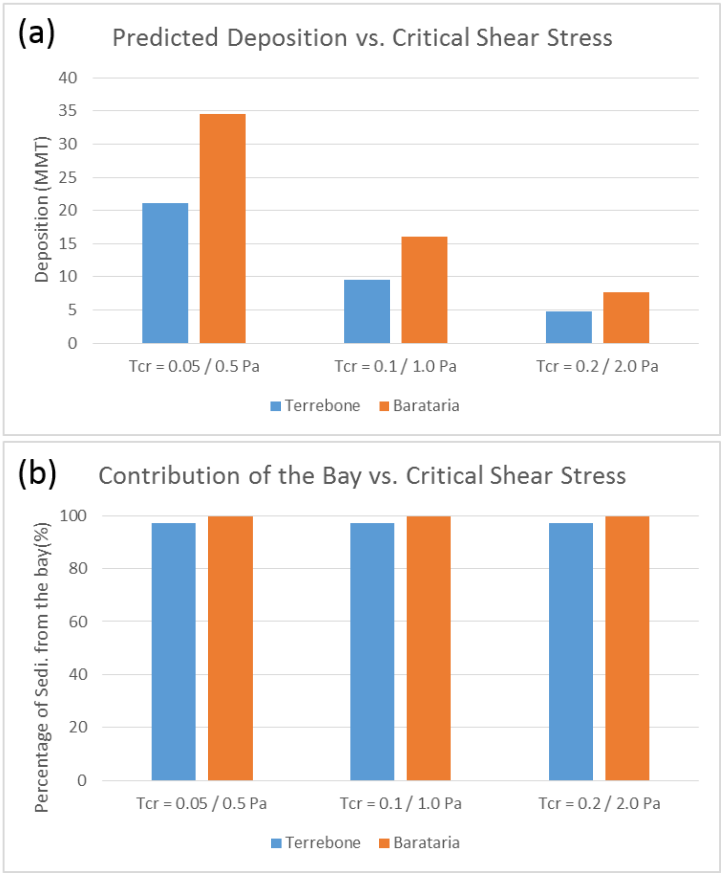

FIGURE 4.14: Model sensitivity of the total deposition (a) and the contribution of sediment from the bay (b) to critical shear stress

and 94.10- to 99.81%, respectively, regardless of different settling velocity and erosion rate (Figure 4.13 (c) and (d)).

Based on the baseline model, experiments were also conducted with different critical shear stress (X2 and X3 in Table 4.3). TDW decreased with critical shear stress for erosion, but PB remained nearly constant within the range of critical shear stress in the experiments (Figure 4.14). The above results indicated that the major source of wetland deposition being from the coastal bays is determined by the transport capability of near shore circulation during the hurricane event rather than sediment parameters.

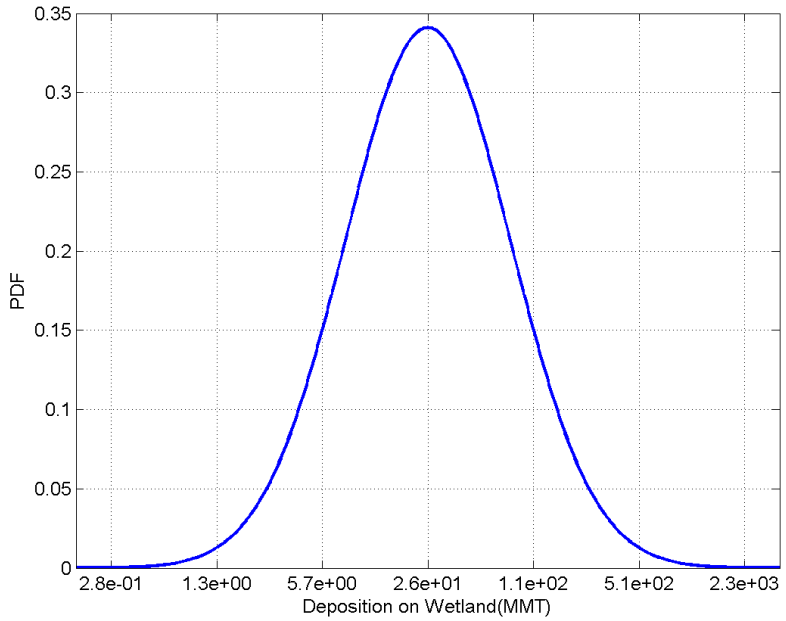

FIGURE 4.15: The probability distribution of the modeled deposition on wetlands by assuming a Gaussian distribution

4.5.2 Uncertainty analysis

To analyze the relative contribution of each parameter to the total variance of results, the following dimensionless parameters were defined:

$$TDW' = \ln\left(\frac{TDW}{TDW_0}\right) \tag{4.17}$$

$$E' = \ln\left(\frac{E}{E_0}\right) \tag{4.18}$$

$$\omega_s' = \ln\left(\frac{\omega_s}{\omega_0}\right) \tag{4.19}$$

$$\tau_{crit}' = \ln\left(\frac{\tau_{crit}}{\tau_{crit,0}}\right) \tag{4.20}$$

where TDW_0=25.6 MMT, E_0=0.5×10^4 kg /m^2 /s, ω_{s0}=0.25 mm /s, $\tau_{crit,0}$=0.1 Pa were from the baseline model. Assuming the model prediction of TDW' can be approximated by a lin-

earized response function of the dimensionless parameters E', ω_s' and τ_{crit}', a multi-variate analysis gave the approximate sensitivity coefficient and variance associated with each sediment parameter (Table 4.5). It was shown that TDW' has a positive sensitivity coefficient with E' (1.21) and a negative sensitivity coefficient with ω_s' (-0.95) and τ_{crit}' (-1.08), which was consistent with our observations in Figure 4.13 and Figure 4.14.

The impact of uncertainties of these three parameters on the modeled deposition on wetlands can be measured by the percentage of each parameter's contribution to the total variance in TDW'. The variance in erosion rate E' accounted for 52.6% of the variance in TDW', while only 32.1% and 15.3% of the total variance could be represented by settling velocity ω_s' and critical shear stress τ_{crit}'. In other words, most of the uncertainty in TDW' was caused by erosion rate.

TABLE 4.5: The approximate sensitivity coefficient and the variance of each dimensionless sediment parameter

Variable X'	Sensitivity Coefficient	Standard Deviation	The Variance in TDW' due to X'	Percentage(%)
E'	1.21	0.70	0.72	52.6
ω_s'	-0.95	0.70	0.44	32.1
τ_{crit}'	-1.08	0.42	0.21	15.3

Assuming the uncertainty in TDW' follows a Gaussian distribution around the baseline run, the probability function of TDW' was shown in Figure 4.15. The 5- to 95 percentile interval for the predicted deposition on wetland was [3.8, 174] MMT.

In reality, critical shear stress could vary in space and time, and settling velocity and erosion rate are also variables depending on sediment properties and flow conditions. But in this paper they are simplified to be constants in time and a uniform value for sediment under water and on the vegetated wetlands. The scarcity of data for these parameters highlights the need for a more detailed sediment data set for the Louisiana coast.

4.6 Summary

The limited understanding of hurricane-induced sedimentation on coastal wetlands was expanded by coupling the sediment transport model with the validated storm surge model and wave model for Hurricane Gustav. The simulations showed that during a hurricane event, the sediment suspension and redistribution mainly occurred to mud on the mud-dominant Louisiana coast; in contrast, the transport of sand was relatively negligible during the hurricane. The modeled spatial range and mean value of sediment accretion on wetlands within the Terrebonne and Barataria Basins were in reasonable agreement with the measurements of fresh deposition after Gustav by Tweel and Turner (2012).

The model prediction of wetland deposition in the Terrebonne and Barataria Basins during Gustav was sensitive to some sediment properties in the model, namely settling velocity, erosion rate and critical shear stress. Among them, uncertainty in erosion rate constituted the major part of the variance in the predicted deposition. Based on a baseline setting verified by the basin-average sediment accretion, the sediment deposition to coastal wetlands during Gustav was about 25.6 MMT, and the 5- and 95% percentile interval was [3.8, 174] MMT.

The long-existing hypothesis about the source of deposition on wetlands was verified via numerical simulation for the first time. Our model results showed that the observed deposition on wetlands are mostly suspended material from the coastal bays. During this large-scale (but short-term) sediment transport and redistribution, Terrebonne Bay and Barataria Bay acted as a major source of sediment exported to adjacent coastal wetlands.

CHAPTER 5 THE IMPACT OF BARRIER ISLANDS ON HURRICANE-INDUCED SEDIMENT TRANSPORT: A THREE-DIMENSIONAL STUDY

5.1 Introduction

Louisiana's barrier islands serve as a valuable natural protection for the coastal environment. They not only shelter the estuaries from severe surge flooding and wave attacks (Penland et al., 1988; Stone and McBride, 1998), but also help maintain the environmental framework of the estuaries by separating the higher salinity Gulf of Mexico water and the lower salinity estuarine water and protecting the coastal wetlands from erosion.

While the benefits of barrier islands in mitigating coastal hazards have been widely recognized by the coastal community, only recently did studies start to apply numerical models to quantify the benefits of barrier island systems in reducing surge and waves (Stone et al., 2005; Wamsley et al., 2009; Grzegorzewski et al., 2011; Cobell et al., 2013). Using the ADvanced CIRCulation Model (ADCIRC) and SWAN, Stone et al. (2005) modeled the storm surge and waves in the south-central Louisiana with shoreline and bathymetric configurations for 1950, the early 1990s, and 2020. The authors found that most of the study area underwent a considerable increase of combined surge and wave height during the interval from 1950 to the 1990s. They predicted that a significant increase of surge and wave height would occur from the 1990s to 2020 as a result of deterioration of the coastline including the barrier islands. Wamsley et al. (2009) applied the ADCIRC model to evaluate the potential benefits of restoration projects at Caernarvon Marsh and Biloxi Marsh in reducing both the storm surge and wave heights. They also found that the deflation of barrier islands could result in an increase of surge and waves on the lee side of the islands. Grzegorzewski et al. (2011) used the ADCIRC model coupled with the STeady State spectral WAVE (STWAVE) model to simulate the storm surge with restored Plaquemines barrier islands and Ship Islands, and reported that the barrier island restoration may significantly influence surge passways and flooding water volume. Cobell et al. (2013)

evaluated the barrier island restoration projects in the Louisiana Coastal Master Plan 2012 and the associated benefits for reducing storm surge and wave heights. Through numerical modeling using ADCIRC and SWAN, the authors concluded that the ridge and barrier island restoration reduced the surge level compared with no-action scenarios and the wave heights also decreased at the immediate backside of the restoration structure.

The role of barrier islands in the entire coastal system, however, goes beyond their being a single defense line against surge and waves. In the previous chapters, we have shown that hurricanes and storms have the potential to cause a sediment exchange between the estuaries and the continental shelf and redistribute sediment towards coastal wetlands. Since the landscape of barrier islands could influence the surge and wave energy inside the estuary, it is logical to ask what role the barrier islands play in the large-scale sediment dynamics in a hurricane event.

In the past decade, many researchers have developed and applied three-dimensional (3D) models for coastal hydrodynamics and sediment transport studies. Compared with two-dimensional (2D) models, 3D models have advantages in many aspects. For instance, while 2D models have to reply on assumptions about velocity profile and equilibrium sediment concentration, 3D models can resolve the vertical variation in current velocity and sediment concentration. This capability is valuable for modeling flow velocity during a storm event because Lapetina and Sheng (2015) demonstrated that the vertical variation of current velocity at locations close to the hurricane track can be significant. When it comes to flow and sediment transport on coastal wetlands, vegetation effects come into play. For submerged vegetation, 3D models allow us to model complex flow patterns both above and within the vegetation canopy. For sediment transport on marshes, modeling the vegetation effects in turbulent mixing is possible only with a multi-layer model. In addition, if the density stratification is important for the sediment suspension and transport, a 3D model is required. Therefore, 3D simulations have been widely used

for sediment studies in the coastal zone, from the continental shelf to the wetlands (Keen et al., 2004; Temmerman et al., 2005; Blaas et al., 2007; Warner et al., 2008; Xu et al., 2011).

In certain circumstances, 2D models seem to be sufficient for the purpose of morphodynamic modeling. For example, Horstman et al. (2013) and Horstman et al. (2015) showed that a carefully calibrated 2D model can achieve an accurate prediction of tidal current and bed deposition at a tidal mangrove similar to the 3D model does. In the studies on long-term morphodynamic simulations, with or without the interaction of hydrodynamic forcing, sediment, and vegetation, 2D models are commonplace due to their efficiency (Van der Wegen and Roelvink, 2008; D'Alpaos et al., 2007; Wegen, 2013).

Although in the previous chapters, the depth-averaged modeling system has been validated in terms of storm surge, waves, and sediment deposition on the wetlands, some questions remain to be answered. The 2D model suggested that the suspended material from the estuary plays a significant role in wetland deposition, and the calculation of bed shear stress and thus the resultant bed erosion highly depends on the current velocity, especially in deep water. Although Chen et al. (2008) indicated the water body was probably well mixed in the inner shelf and the estuaries during high-energy events such as a hurricane, the extent to which the current velocity varies vertically is still unclear. Moreover, the inland extension of sediment deposition relies on a reasonable representation of surge and wave attenuation over the vegetated wetlands, and how the vegetation affects the vertical mixing of suspended sediment needs to be explored.

In this chapter, we move forward to test our hypotheses on hurricane-induced sediment transport using a 3D-version of the coupled modeling system and to apply the validated 3D models to investigate the influence of barrier islands during hurricane Gustav. Our specific objectives are to (1) develop a three-dimensional fully-coupled modeling system for storm surge, waves and sediment transport and validate the modeling system with the datasets described in Chapter 3 and 4; (2) verify whether different modeling approaches for vertical variation of cur-

rent velocity and sediment concentration would affect the prediction for the hurricane-induced sedimentation on wetlands and the finding that the major source of the deposited material is the suspension in the bays; (3) evaluate the impact of the possible deterioration of barrier islands on the large scale sediment redistribution under hurricane conditions.

5.2 Modeling Hurricane Hydrodynamics and Sediment Transport in 3D

5.2.1 Governing equations and coordinate system

In 3D mode, Delft3D-FLOW computed the vertical velocity from the continuity equation under the hydrostatic assumption. Two different vertical grid systems are available in Delft3D: the σ-coordinate and the Cartesian Z-coordinate (Figure 5.1). The σ-coordinate was initially developed for atmospheric models (Phillips, 1957). It consists of multiple vertical layers bounded by two sigma planes, which are not strictly horizontal but follow the bottom topography and the free surface and represent the topography smoothly. A shortcoming of the σ-coordinate is that the coordinate lines may intersect with the density interfaces, which may give significant errors in the approximation of strictly horizontal density gradients (Stelling and Van Kester, 1994). Therefore, the Z-coordinate was also introduced for 3D simulations of weakly forced stratified water systems.

In addition to a background horizontal viscosity / diffusivity, four turbulence closure models have been implemented in Delft3D to account for 3D turbulence. The vertical viscosity and diffusivity can be determined by one of the following ways: a constant coefficient, an algebraic eddy viscosity closure model, a k-L turbulence closure model, or a k-ϵ turbulence closure model.

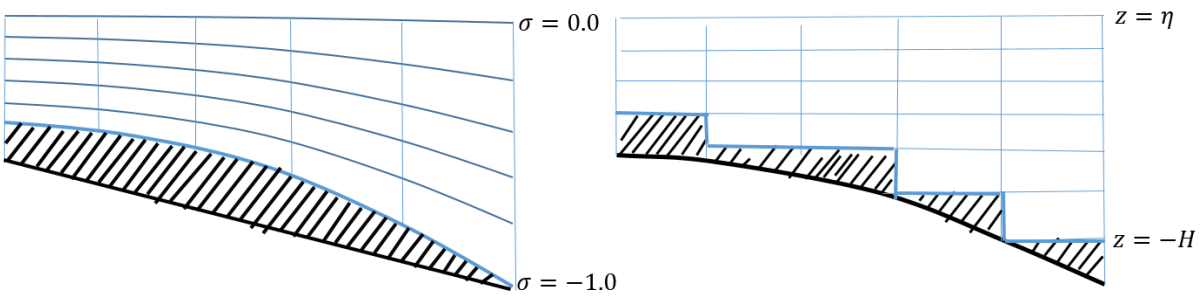

FIGURE 5.1: Schematic of σ-coordinate (left) and Z-coordinate (right)

5.2.2 Current-induced bed shear stress from the three-dimensional velocity field

In 2D mode, bed shear stress is calculated from the depth-averaged velocity $\vec{U}$ and a 2D Chezy coefficient C_{2D} in the following way:

$$\vec{\tau_b} = \frac{\rho_0 g \vec{U}|\vec{U}|}{C_{2D}^2} \tag{5.1}$$

where ρ_0 is the water density and g is gravitational acceleration.

For a 3D model, vertical variation of horizontal velocity can be resolved between the vertical layers, and the bed shear stress can be expressed as a function of shear velocity $\vec{U_*}$:

$$\vec{\tau_b} = \rho_0 \vec{U_*}|\vec{U_*}| \tag{5.2}$$

Normally, it is assumed that the first layer above the bed is situated in the logarithmic boundary layer. Letting Δz_b be the distance from the bed to the grid point in the first layer above the bed and $\vec{U_b}$ be the horizontal velocity at Δz_b, the logarithmic law gives

$$\vec{U_b} = \frac{\vec{U_*}}{K} \ln\left(1 + \frac{\Delta z_b}{2 z_0}\right) \tag{5.3}$$

where the roughness height z_0 of the bed can be related to the 2D Chezy coefficient C_{2D} by

$$z_0 = \frac{H}{e^{\left(1 + K C_{2D}/\sqrt{g}\right)} - e} \tag{5.4}$$

5.2.3 The vegetation module in the 3D mode

While vegetation effect in the 2D flow model is parameterized as a drag force in the momentum equation, a more comprehensive Directional Point Model (DPM) can be applied in the 3D model. The features of the 3D DPM include the following: vegetation properties, such as stem diameter and density, are allowed to vary with the vegetation height; the friction force due to vegetation is calculated for each vertical layer (following a quadratic law); the influence of vegetation on vertical mixing can be modeled by an extra source term in the kinetic turbulence energy equation and an extra source term in the epsilon equation. For more details, readers are referred to Uittenbogaard (2003). This method has been validated extensively against various datasets, including laboratory experiments (Baptist, 2003; Borsje et al., 2009) and field data on flow patterns in salt marshes, intertidal flats and sandy sites (Temmerman et al., 2005; Bouma et al., 2007). In the meantime, the drag-force based representation of vegetation (Baptist, 2005), as described in Chapter 3, is still available in 3D mode.

5.2.4 Wave effects on the 3D flow model

Wave-current interactions are more complicated in the 3D model in the sense that more physical processes can be considered and the vertical distribution of different forcing is more realistic.

In 3D models, three types of wave forcing due to the gradient of radiation stress are included in the momentum equation and treated separately according to their origins: the one caused by wave breaking and whitecaping is applied at the top layer, the one caused by bottom friction is applied at the bottom layer, and the remaining part is distributed over the water column (Deltares, 2012).

For wave-induced flow and mass flux, the Generalized Lagrangian Mean (GLM) theory (Andrews and McIntyre, 1978) allows a convenient representation of Stokes drift in both 2D and 3D models (Groeneweg and Klopman, 1998) and has been implemented in Delft3D (Wal-

stra et al., 2001). In 3D models, Stokes drift is spread over the vertical direction according to the linear wave theory (Dean and Dalrymple, 1991). In addition, a wave-induced current (streaming) is modeled as a time-averaged shear stress in the wave boundary layer and assumed to decrease linearly within the boundary layer as shown by Fredsøe and Deigaard (1992).

The vertical mixing processes are also enhanced by the wave actions, for example, the wave breaking at the water surface and the friction in the bottom boundary layer. These processes are modeled by adding the wave energy dissipation and production terms in the turbulence model (Deltares, 2012).

The combination of wave- and current-induced bed shear stress follows the same way in the 2D model, except that the depth-averaged velocity is replaced by the velocity near the bed and corrected by the Stokes drift.

5.3 Model Setting

5.3.1 Three-dimensional mesh

The 3D model in this chapter used the same nested mesh as we presented in Section 3.4.1. To determine a proper vertical structure of the computational mesh, we conducted a literature review on 3D simulations of flow, wave and sediment transport processes. Despite the various models and study areas, a sufficient resolution of 3D flow and sediment phenomena in most coastal applications requires the number of vertical layers to range from four to ten (Table 5.1). Therefore, in this study, seven vertical layers with a thickness of 5%, 10%, 20%, 30%, 20%, 10%, and 5% of total water depth in the σ-coordinate were used. The same bathymetric data for the 2D model as described in Section 3.4.2 were interpolated into the 3D mesh here.

5.3.2 Vegetation for surge reduction

Four major vegetation types, namely saline marsh, brackish marsh, intermediate marsh, and freshwater marsh, on coastal Louisiana have been modeled through the 3D DPM. Their spatial distribution came from the same USGS dataset as mentioned in Section 3.4.2. The stem

TABLE 5.1: A summary of the number of vertical layers in the 3D hydrodynamic and sediment transport models

Literature	Study Area	Physical Processes	Numerical Model	Num. of Vertical Layers
Horstman et al. (2015)	Mangrove at the Thai Andaman coast	tidal flow and sedimentation	Delft3D	8 uniform layer
Hu et al. (2015)	Breton Sound under Hurricane Issac (2012)	storm surge with vegetation	Delft3D	7 non-uniform layer
Lapetina and Sheng (2015)	Galveston Bay under Hurricane Ike (2008)	Storm surge, wave and sediment transport.	CH3D-SWAN	4 and 8 uniform layers showing little difference
Weisberg and Zheng (2008)	Tampa Bay, FL under a hypothetical hurricane	storm surge	FVCOM	11(uniform)
Xu et al. (2015)	LA-TX continental shelf	Storm surge, current and sediment transport.	ROMS	30 non-uniform layers
Zheng et al. (2013)	Gulf of Mexico under Hurricane Ike	Storm surge	FVCOM	11 uniform layers

diameter and density were assumed to be vertically uniform. The background Manning's coefficient was set to be 0.025, approximately the value for the shallow water in open bays to account for the friction to flow due to a bare bed.

Since the 3D DPM assumed the vegetation stem to be rigid, we reduced the vegetation stem height to 60% of its original value, which was similar to other studies (Hu et al., 2015; Kuiper, 2010), to account for the flexibility of vegetation. We should note that the exact reduction of vegetation height in 3D DPM is not necessary to be the same as in the literature, and an optimum setting might require further calibration with field measurements.

5.3.3 Vegetation for wave attenuation

The vegetation effect in wave attenuation was modeled in the same way as in the 2D model, using the Madsen's formulation (Madsen et al., 1988). The local water depth in the formula was updated from the 3D flow model for each wave computation.

5.3.4 Sediment properties

Consistent with the 2D model, the median diameter of sand is 0.14 mm, and muddy material has a erosion parameter of 0.5×10^{-4} kg /m^2 /s and a settling velocity of 0.25 mm /s in the 3D model . The critical shear stress was 0.1 Pa for mud in the sea and coastal bays and 1.0 Pa for vegetated land to account for the fact that vegetation roots can strengthen the soil layer and enhance its resistance to erosion. The temperature and salinity stratigraphy and their effects in sediment properties were not considered in the model.

5.3.5 Other settings: turbulence and coupling

Most of the parameters for the wave model remain the same. Since the flow model was in 3D mode, the current velocity used in the wave model can be either the depth-averaged velocity, the velocity at the surface layer, or a vertically weighted velocity. In this study, the depth-averaged velocity was provided for wave computation. The time step for the storm surge simulation was 0.5 minute. The wave model ran in the non-stationary mode with a time step of 60 minutes. The coupling interval between the flow and the wave model was one hour.

The background horizontal eddy viscosity was set to be 1.0 m^2 /s. A k-ϵ turbulence closure was applied to account for the 3D turbulence. Other model parameters remained the same as in the 2D model. For details, please refer to Section 3.4.

5.4 Hindcast of Storm Surge and Waves in Hurricane Gustav (2008)

5.4.1 Storm surge and waves

Similar to previous chapters, we simulated the hydrodynamics and sediment transport during Hurricane Gustav from August 28 to September 5, 2008, following a one-month spin-up time. The model predictions of storm surge and waves were validated against the water level at the eleven NOAA tide stations, the peak surge at the eighty-seven CRMS stations, the water level, wave heights and wave periods at the six wave gauges in Kennedy et al. (2010). A comparison of the modeled peak surge with the observations at CRMS stations was plotted in

TABLE 5.2: The summary of errors for the modeled (3D and 2D) wave and surge time series

	Variable	Num. of Stations	Bias (3D/2D)	Scatter Index (3D/2D)
NOAA tide stations (southeastern LA)	Water Level (m)	6	-0.07/-0.08	0.20/0.18
NOAA tide stations (total)	Water Level (m)	11	-0.06/-0.06	0.36/0.35
Kennedy et al.[2010]	Water Level (m)	6	0.07/0.07	0.28/0.28
Kennedy et al.[2010]	Wave Height (m)	5	0.10/0.10	0.27/0.27
Kennedy et al.[2010]	Peak Wave Periods (s)	6	0.17/0.17	0.41/0.41

Figure 5.2. The normalized bias and scatter index of the modeled surge and wave time series were summarized in Table 5.2.

The model predictions of storm surge, wave heights and wave periods showed similar agreement with the measurements as the 2D model (Table 5.2), although no intention was made to reproduce the surge and waves from the 2D model in the previous chapter. When most of the physical parameters are kept the same, it is safe to say that the 3D model can serve as a platform to study the hurricane-induced sediment transport processes with a better representation of the 3D flow field, vertical mixing and possible stratification of sediment, and at least the same level of accuracy in hydrodynamics can be achieved as in the 2D model.

5.4.2 Current profile

The 3D model and the 2D model showed a similar spatial pattern of maximum current speed during Hurricane Gustav in a depth-averaged sense (Figure 5.3). On the continental shelf, a strong current along the coastline formed from the Mississippi River Delta to the inlet of Terrebonne Bay, and the maximum current speed (depth-averaged) reached $\sim$4 m/s. In the estuaries, current speed was reduced behind the barrier islands. The maximum value (depth-averaged) was 1 to 2 m/s in Terrebonne Bay and Barataria Bay.

The lack of measurements for velocity profile during Gustav made it diffcult to assess the accuracy of the modeled current velocity, but the 3D model revealed more information about

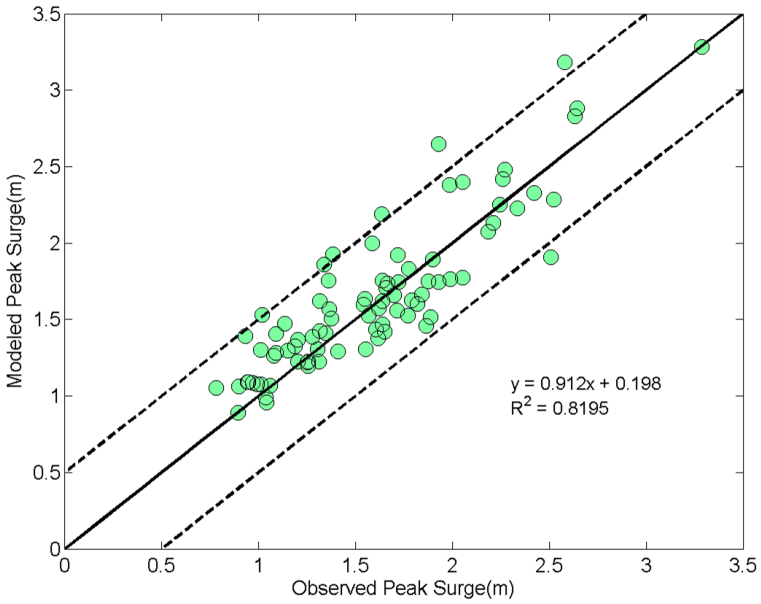

FIGURE 5.2: A comparison of the predicted peak surge and observations at the CRMS stations from the 3D model

the vertical variation of current velocity. A comparison of the depth-averaged current velocity and the one in the bottom layer suggested that vertical variability of current velocity did exist in most of the domain even with the high energy hurricane forcing (Figure 5.4). In the estuaries, the flow velocity near the bed was generally smaller than the one in the upper part of the water column, while the strong longshore flow ($>$1 m/s) on the inner continental shelf seemed to be better-mixed over the water volume.

5.4.3 Sediment transport and morphological effect

Since the 3D model and the 2D model produced similar storm surge level and wave heights, it is not surprising to see that the bed shear stress from the 3D model exhibited a spatial pattern similar to the 2D model (Figure 5.5). When Gustav was making landfall, a high shear stress of $\sim$8 Pa was shown on the continental shelf close the hurricane track. As the shear stress caused by wave orbital velocity is inversely proportional to water depth, the shear stress in the shallow water in the estuary and flooded wetland exhibited a larger magnitude. On the other hand, the vertical variation of current velocity caused some subtle differences in the predicted bed shear

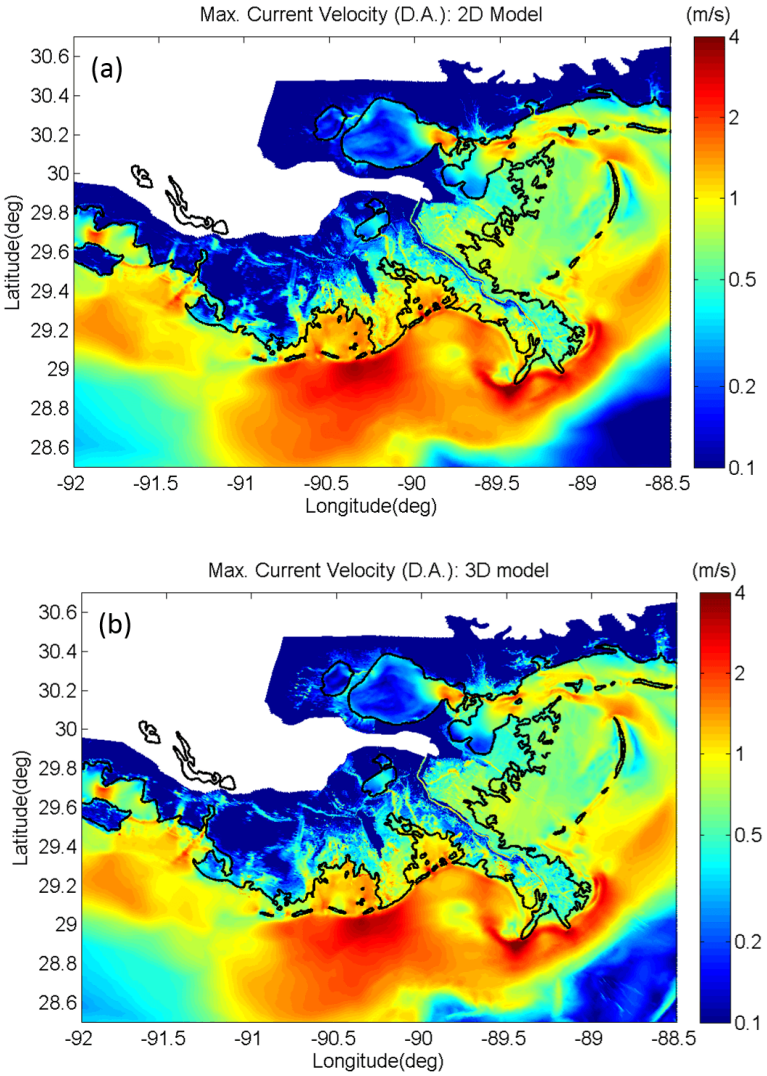

FIGURE 5.3: The maximum current speed (depth-averaged) during Gustav: 2D model (a) versus 3D model (b)

stress, which can be observed in the time series of hydrodynamic and morphodynamic variables at the selected points in Terrebonne Bay (Figure 5.6).

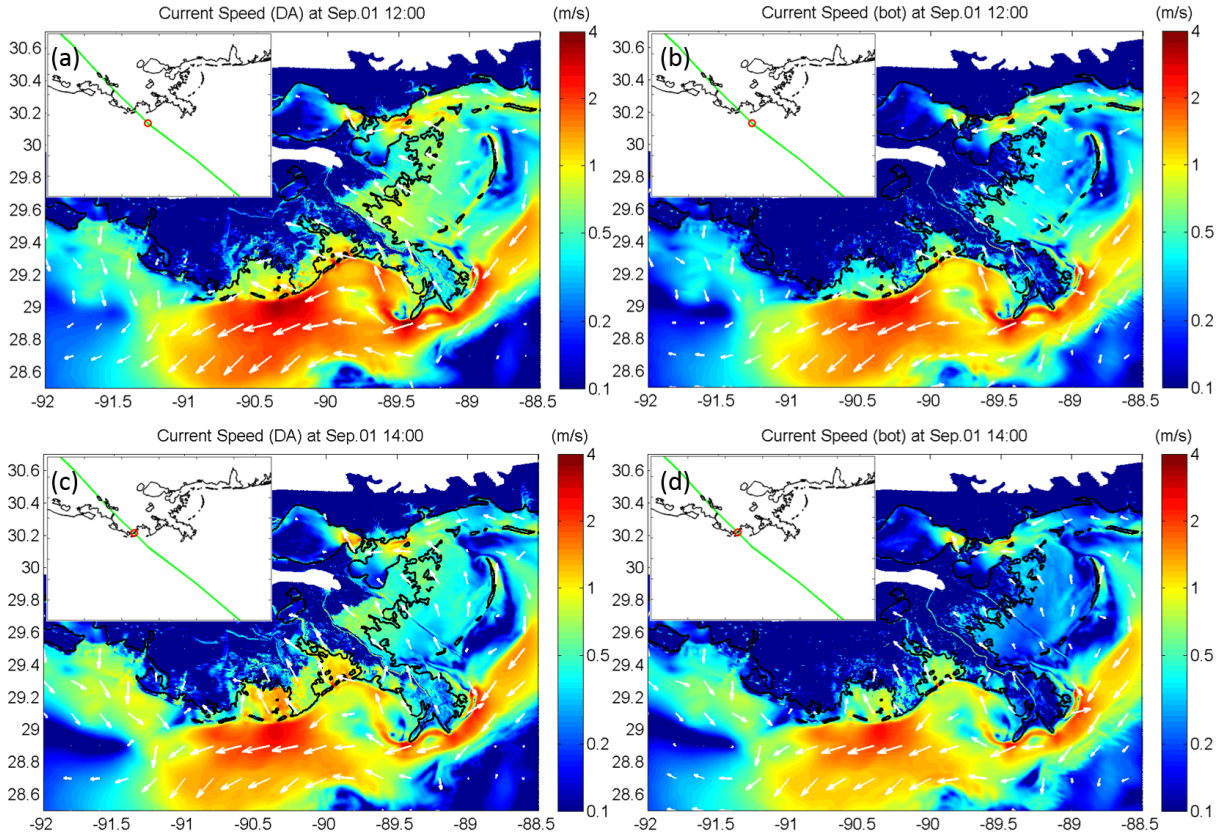

FIGURE 5.4: A vector view of the modeled current velocity before and after the landfall of Gustav (2008) (green lines: hurricane track; red circles: hurricane center relative to the shoreline): (a) the depth-averaged velocity at 12:00 UTC, Sep 01, or approximately 2 hours before landfall, (b) the bottom-layer velocity at 12:00 UTC, Sep 01, (c) the depth-averaged velocity at 14:00 UTC, Sep 01, or approximately landfall, and (d) the bottom-layer velocity at 14:00 UTC, Sep 01.

At P01 and P02, which were located in the estuary and in the water pond on wetlands respectively, the modeled local water depth and wave heights were very close to the results from the 2D model. However, the modeled current velocity in the bottom layer was much smaller than the depth-averaged velocity in the 2D model, which was consistent with our observations in Figure 5.4. Although the current-induced bed shear stress was smaller in the 3D model, the wave-induced component and the effect of the nonlinear combination of these two components

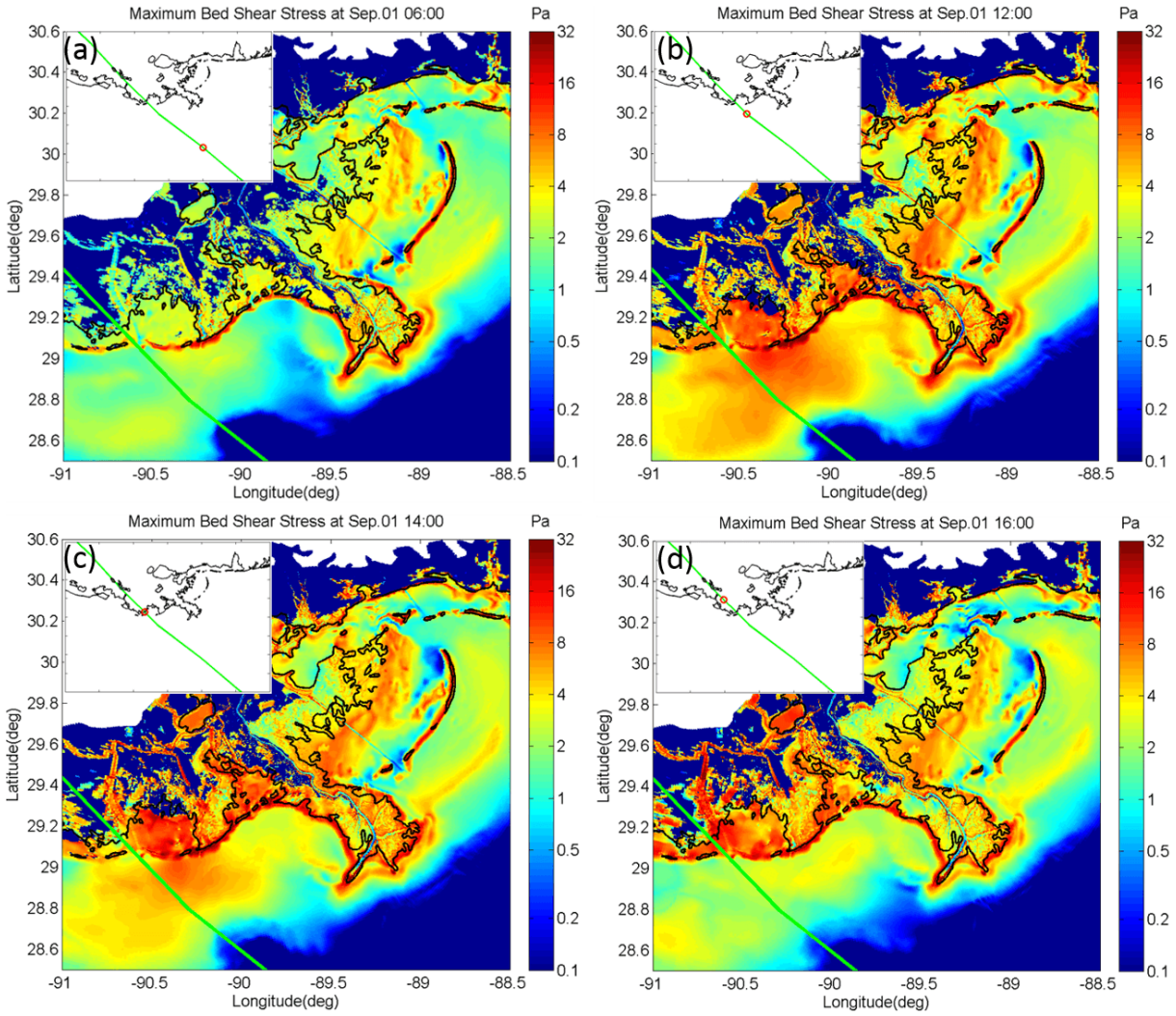

FIGURE 5.5: The modeled bed shear stress before and after the landfall of Hurricane Gustav (2008) from the 3D model (green lines: hurricane track; red circles: hurricane center relative to the shoreline): (a) 06:00 UTC, Sep 01, or approximately 8 hours before landfall, (b) 12:00 UTC, Sep 01, or approximately 2 hours before landfall, (c) 14:00 UTC, Sep 01, or approximately landfall, and (d) 16:00 UTC, Sep 01, or approximately 2 hours after landfall.

had a much larger magnitude than the current-induced shear stress alone. Therefore, the combined bed shear stress from the 3D model was similar to that from the 2D model.

At P03, which was located on vegetated wetland, the general trend of hydrodynamic processes was similar to the prediction from the 2D model, except that the current velocity and bed shear stress were slightly larger. Remembering that the 3D model and the 2D model utilized different methods for modeling vegetation effects and different roughness coefficients to account for the friction on the bare bed, it was not surprising that the 3D DPM produced different bed shear stress compared with the drag force based method in the 2D model, using the same vegetation properties and spatial distribution. Also note that the vegetation height was reduced to 60% of its original value in the 3D DPM, and an optimum choice of this percentage highlighted the need for more field data on the hydrodynamic effects of vegetation under hurricane conditions.

The morphological changes at all the three observation points behaved qualitatively the same as those in the 2D model (Figure 5.6b and Figure 4.10b): a severe erosion occurred prior to the deposition in the shallow bay while a direct deposition was more likely to happen on wetlands. Some differences in details between the 3D and the 2D model were noticeable: (1) at P01 and P02, the sediment was well-mixed in the water body, and the sediment concentration was larger than the prediction from the 2D model; (2) at P01 and P02, both erosional and depositional processes became more intensive than those in the 2D model, which may be a result of higher sediment concentration in the water body; (3) at P03, erosion was enhanced due to the larger shear stress from the 3D DPM method, which further led to a smaller net deposition on wetland.

Similar to the analysis for the 2D model, the sediment flux from different origins, either from the bay or from the sea, were evaluated at four cross-sections (defined in Figure 4.8). At the interface between the continental shelf and the estuaries (cross-section B1 and T1), a

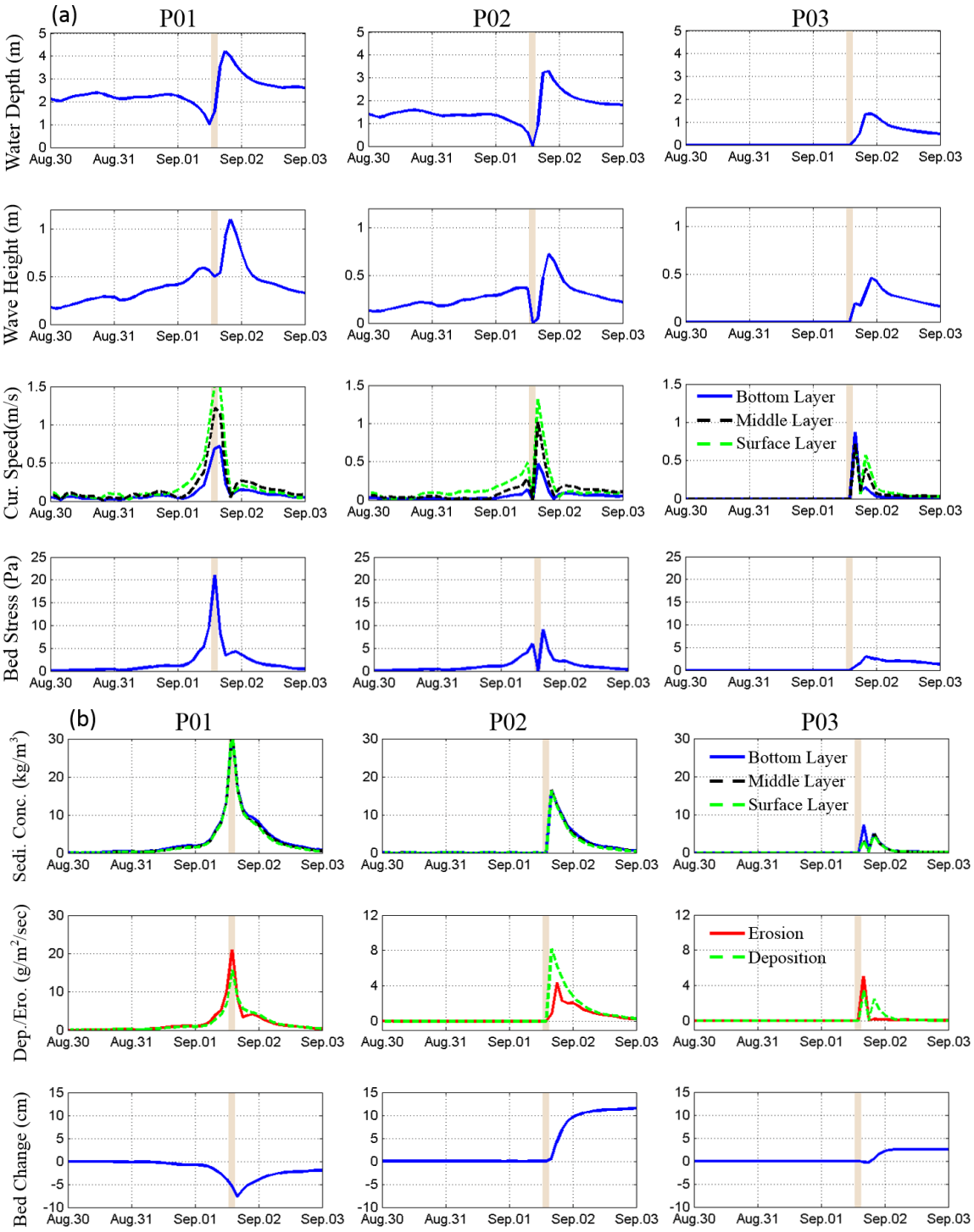

FIGURE 5.6: Modeled hydrodynamics processes (a) and morphological processes (b) at P01/P02/P03 (locations in Figure 4.8) in Terrebonne Bay: from the 3D model

significant transport of marine material (red lines in Figure 5.7) can be found. However, the offshore transport of material from the estuary, which appeared in the 2D model, became much smaller. A further investigation showed that the water discharge across the boundary was nearly the same, but the sediment loads at the estuary inlet were smaller than their counterparts in the 2D model. At the cross-sections between the estuaries and wetlands (B2 and T2), a large amount of sediment originating from the estuaries was moved towards the wetlands, although the magnitudes of the sediment fluxes were smaller than those appeared in the 2D model (grey solid lines and grey dashed lines in Figure 5.7). Again, the transport of sediment from wetlands was almost negligible compared with other two groups.

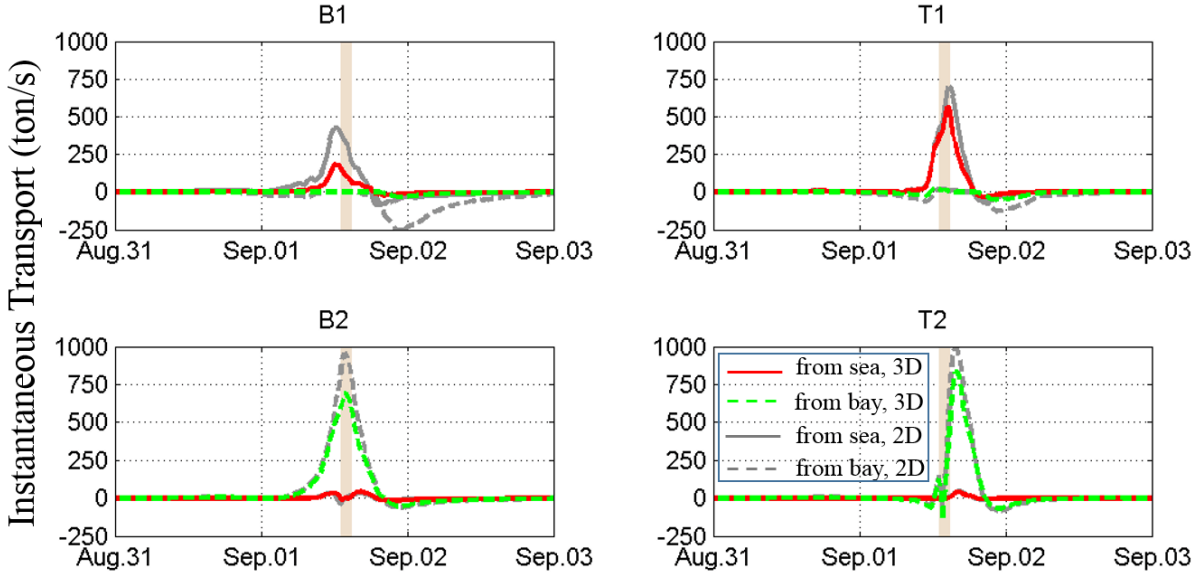

FIGURE 5.7: The time series of the suspended transport through cross-sections (T1/B1/T2/B2 defined in Figure 4.8): from the 3D model

As a result, in the 3D model, almost all the components of the sediment suspension and redistribution within the shelf-bay-wetland system during Gustav slightly decreased compared with their counterparts in the 2D model (Figure 5.8). For instance, the net sedimentation on the coastal wetland in the 3D model dropped from 9.61 to 7.74 MMT in Terrebonne and from 15.98 to 12.63 MMT in Barataria. The post-hurricane deposition, defined in equation 4.11, in

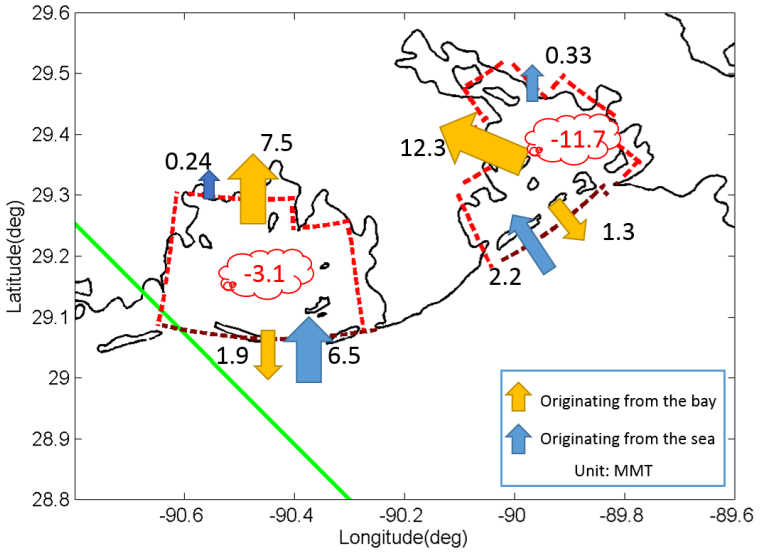

FIGURE 5.8: The net sediment transport in the shelf-bay-wetland system: from the 3D model

Terrebonne and Barataria also decreased from their counterparts in the 2D model, but they still lay in a reasonable range from the basin-averaged deposition reported in Tweel and Turner (2012) (Figure 5.9).

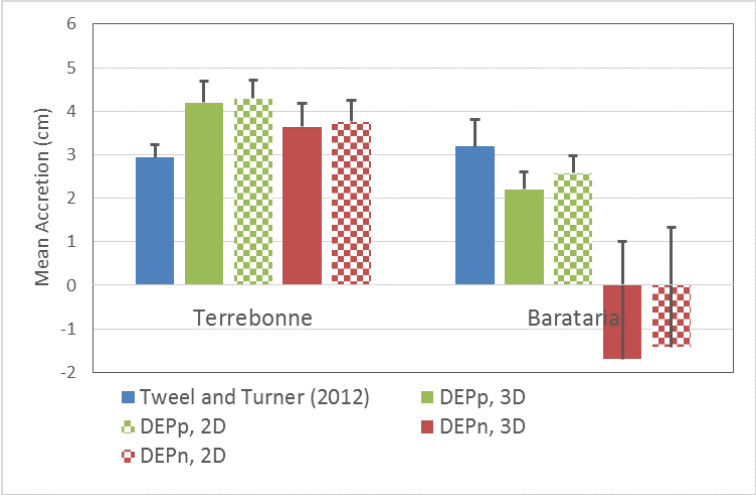

FIGURE 5.9: Comparison of the modeled post-hurricane deposition DEP_p (equation 4.10) and net deposition DEP_n (equation 4.11) with measurements in Tweel and Turner (2012)

5.4.4 Summary

In this section, a fully-coupled storm surge, wave and sediment transport model in three dimensions was developed based on the 2D depth-averaged model in the previous chapters. Compared with the 2D model, several improvements have been included in the 3D model.

A direct benefit of using the 3D model is the capability to solve for the vertical variation of current velocity. Model results showed that in most of the nearshore regions, including the estuaries, the vertical variation of current velocity was significant, and the bottom velocity was smaller than the depth-averaged one. On the east side of the hurricane track (close to the landfall location), where the longshore current on the continental shelf was the strongest, the water was better-mixed than the rest of the domain. A more realistic vertical profile of the current velocity in the 3D model was helpful for an accurate prediction of the bed shear stress due to the current. Another improvement of the 3D model is a more comprehensive representation of the vegetation effects in storm surge attenuation. The directional point method in the 3D model considered not only the vegetation drag force in the moment equations but also the vegetation effects in turbulence mixing.

The 3D model was validated against the same dataset of surge and waves as in Chapter 3, and the statistics showed the 3D model can achieve the same level of accuracy in hydrodynamic results as the 2D model with minimum calibration. With the same sediment properties, the 3D model and the 2D model predicted similar sediment movement among the shelf-bay-wetland system, but the magnitude of sediment flux was smaller in the 3D model, which could be explained by a smaller erosion forcing on the bed and thus a smaller sediment load in the 3D model. In total, the net sedimentation on the coastal wetland in the 3D model was 7.74 MMT in Terrebonne and 12.63 MMT in Barataria, and most of the deposited material came from suspension in the bay, which was consistent with our findings using the 2D model.

TABLE 5.3: Model settings for the selected barrier islands in the baseline configuration and the degradation configuration

	Crest Elevation of the Islands or the Shoals (m, MSL)	Mannings Value at the Islands or the Shoals
Baseline Configuration	$\sim$ +1.0 m	0.03 to 0.05
Degradation Configuration	$\sim$ -1.6 m	0.02

5.5 The Effect of Barrier Islands on Sediment Redistribution

5.5.1 Model setting: baseline configuration and degradation configuration

To assess the potential impact of the deterioration of barrier islands on the hydrodynamic process and sediment dynamics in the shelf-bay-wetland system, 3D simulations for hurricane-induced sediment transport were conducted for a baseline configuration and a degradation configuration. The 3D model described in section 5.3 served as the baseline configuration. For the degradation configuration, the bathymetry and landscape at four barrier islands in Terrebonne Bay and Barataria Bay were modified corresponding to a hypothetical degradation scenario (Figure 5.10). To be specific, the barrier islands were degraded into submarine shoals by lowering the crest elevations from approximately +1.0 m (MSL) to -1.6 m (MSL). The Manning's coefficients at the islands were reduced to 0.02, which is the value used in the shallow bays. Table 5.3 summarized the simulation configurations for the barrier islands and the submarine shoals in this section. The wind field for Hurricane Gustav, the tidal boundary condition, and the river discharge were kept the same for both configurations. It should be noted that the degradation configuration was for illustration purpose only. It represented one possible degradation scenario and the practicality was not verified here.

5.5.2 Impact on storm surge and waves

Inspection of the maximum surge at a cross section over Timbalier Island (C1-C2 in Figure 5.10) confirmed that the surge level was high enough to overtop the crest of the barrier islands during Hurricane Gustav (Figure 5.11). The potential degradation of the barrier islands could lead to an increase of surge level on the protected side by up to a half meter. The barrier

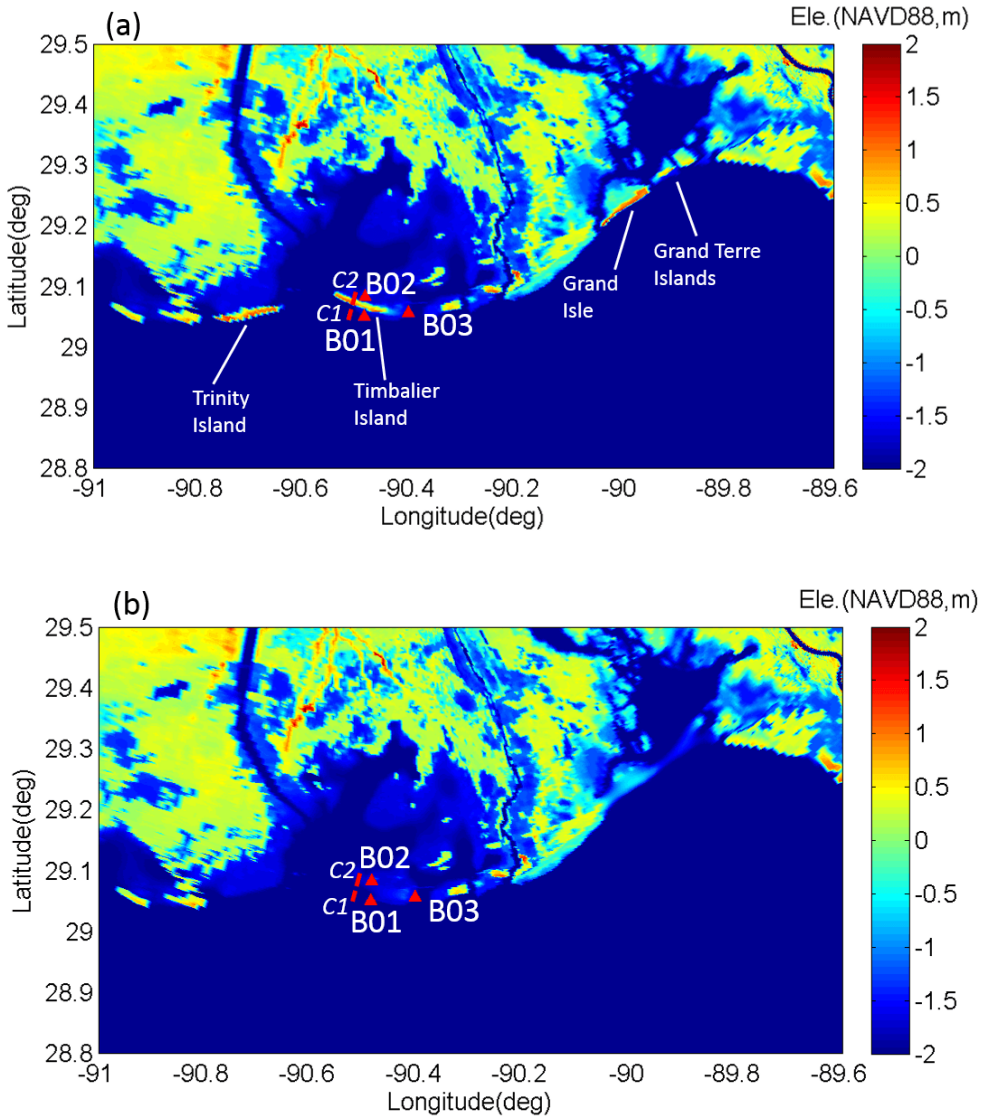

FIGURE 5.10: The model bathymetry in the baseline configuration (a) and degradation configuration (b). Note the positions of the barrier islands in (a).

islands also had some adverse effect by raising the surge level on the gulf side. But this increase was relatively small and only showed up in a limited distance from the islands (Figure 5.11).

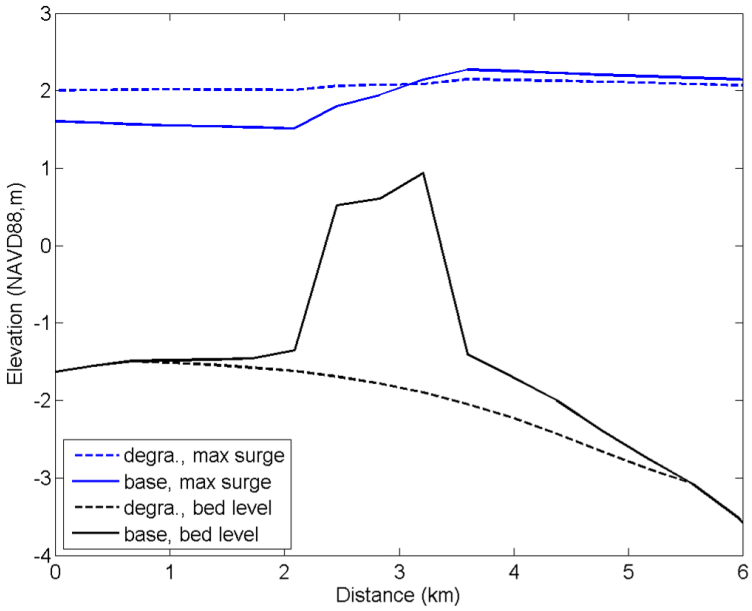

FIGURE 5.11: The bed level and maximum surge at the cross section C1-C2 for the baseline configuration (solid lines) and the degradation configuration (dashed line)

An overall view of the benefits of barrier islands in storm surge and wave reduction can be obtained by comparing the maximum surge level and significant wave height from the baseline configuration and those from the degradation configuration. To be specific,

$$y_{reduce} = y_{degrd} - y_{base} \tag{5.5}$$

where y can be maximum surge level or significant wave height. The analysis focused on the change near the barrier islands and within the estuaries, and the reduction of peak surge and maximum wave height are presented along with the corresponding value from the baseline configuration (Figure 5.12 to Figure 5.15). Blue indicates an increase of peak surge and wave height in the degradation configuration, and red indicates the opposite.

When barrier islands were removed, the peak surge level increased within both Terrebonne Bay and Barataria Bay, and this effect decreased with the distance from the islands (Fig-

ure 5.13). The maximum increase of surge was about a half meter, and most of the area within the bay experienced an increase of more than 0.1 m. In contrast, surge level on the seaward side of the islands dropped slightly in the degradation configuration as more surge water can flush into the estuaries without the obstruction of barrier islands.

In the wave model, the wave heights within the basins depend on many factors including local wind, bathymetry, bottom friction, and long swells propagating from the gulf. From the model results, most long swells did not enter the estuaries as a result of depth-limited breaking at the steep bathymetric slope (Figure 5.14). Only a small portion of wave energy penetrated into the estuaries through the narrow inlets between barrier islands. Therefore, the wave field within the bay was mainly controlled by local wind waves and much smaller than the offshore swell in the shelf.

In the degradation case, the significant wave height on the protected side of barrier islands generally increased. Unlike the reduction of the storm surge, however, this effect was concentrated in a limited area behind the barrier islands (Figure 5.15). We also notice that the wave height at the narrow inlets between the islands in Barataria Bay decreased after the islands were removed. This could be attributed to the fact that smoothing the bathymetry at the grid points of the barrier islands (in the degradation configuration) changed the deep channel into relatively shallow water with similar depth to the shallow bay.

In order to evaluate temporal evolution of storm surge and waves corresponding to the degradation of barrier islands and the deviation from the baseline configuration, three observation points close to Timbalier Island were selected (B01, B02, and B03 in Figure 5.10). B01 and B02 were on the seaward side and the protected side of Timbalier Island, and B03 was located in the gap between Timbalier Island and East Timbalier Island. Model results showed that the reduction of wave heights and surge due to the hypothetical degradation of barrier islands was rather limited at all the three observation points, except that the surge level at the protected

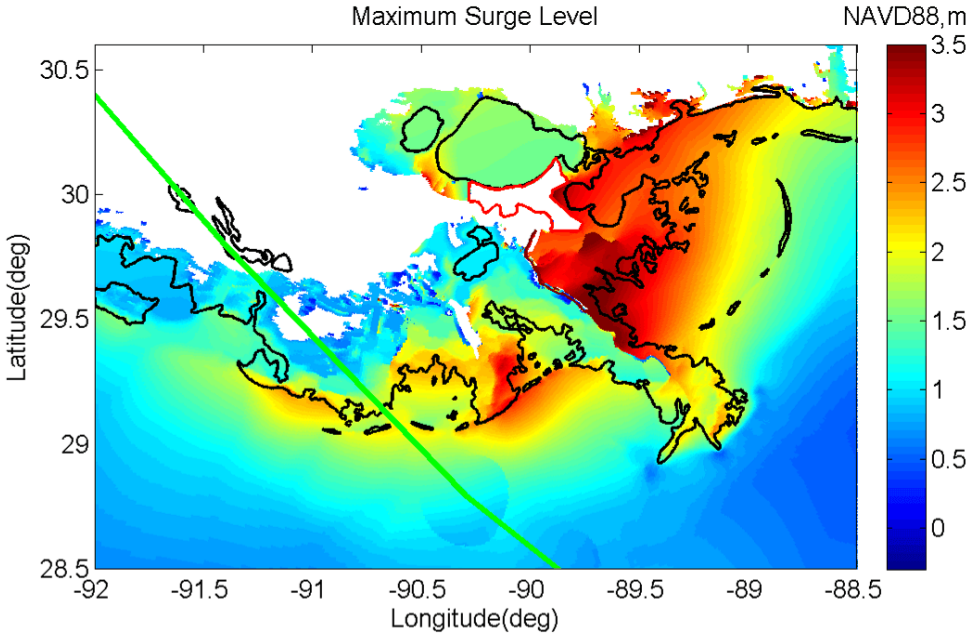

FIGURE 5.12: The modeled maximum storm surge during Hurricane Gustav (2008): baseline configuration (green line: the track of Gustav)

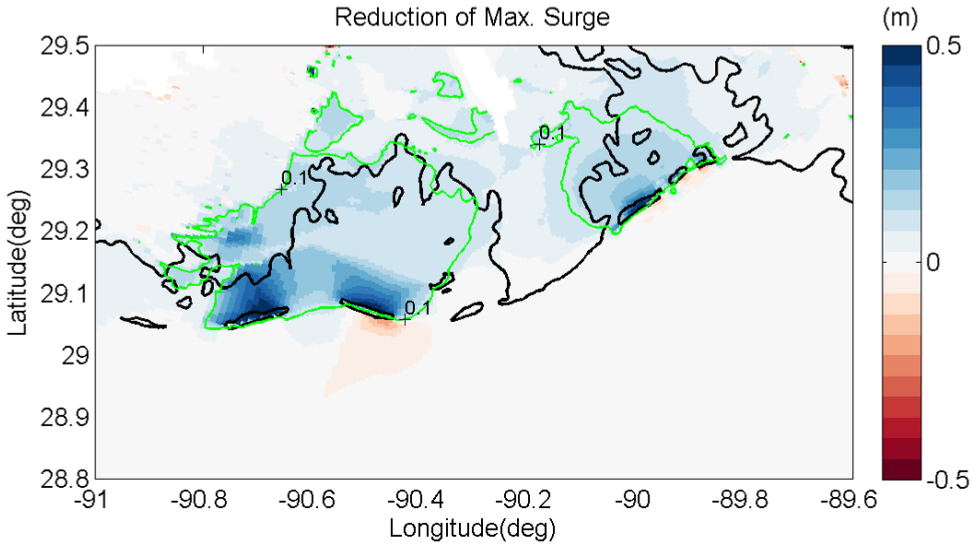

FIGURE 5.13: The reduction of storm surge due to the barrier islands during Hurricane Gustav (2008) (green line: 0.1 m contour line for storm surge reduction)

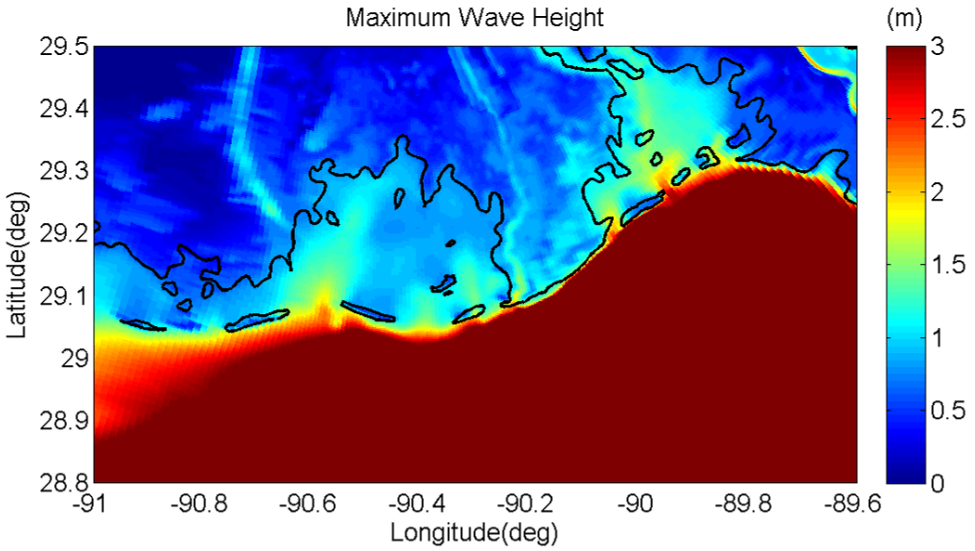

FIGURE 5.14: The modeled maximum wave height during Hurricane Gustav (2008): baseline configuration

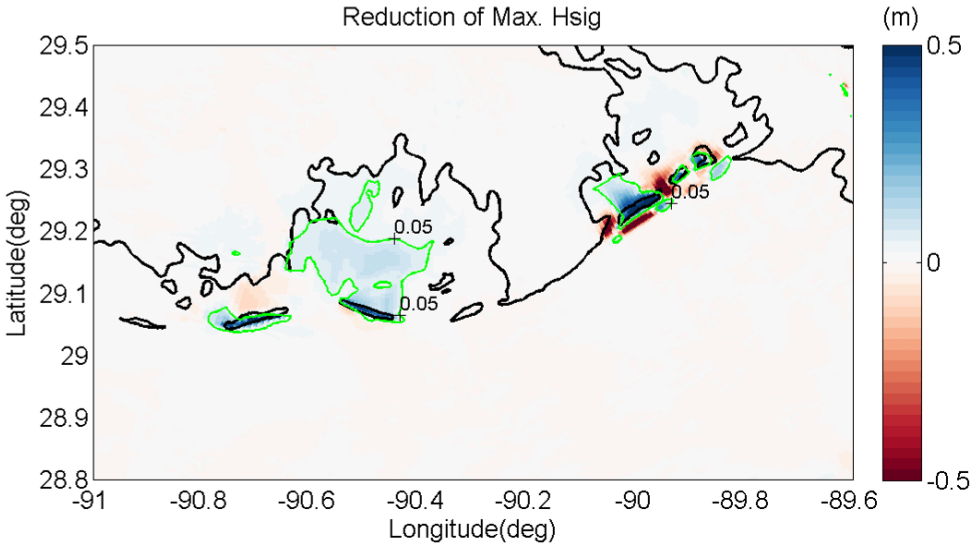

FIGURE 5.15: The reduction of wave height due to the barrier islands during Hurricane Gustav (2008) (green line: 0.05 m contour line for wave height reduction)

side went up from 3.0 m in the baseline configuration to 3.5 m in the degradation configuration (Figure 5.16a). The current speed (depth-averaged) at B01 and B02 also exceeded the one from the baseline configuration by 0.2 to 0.3 m/s as the blocking effect of the barrier islands was removed, which further caused an increase of bed shear stress (2.4 Pa at B01 and 4.1 Pa at B02) in the degradation case. In terms of sediment transport, these changes could benefit the suspension and onshore transport of sediment from inner shelf to the estuaries.

5.5.3 Impact on sediment transport

The total sediment transport, including the suspended sediment transport and the bedload, of all the sediment classes from the degradation configuration was plotted in Figure 5.17. When the hurricane was making landfall, the suspended sediment was moving along the coastline from east to west, following the direction of longshore currents. Because of different orientations of the bay, the sediment fluxes outside Terrebonne Bay were mainly shore-parallel, while the fluxes outside Barataria Bay were turning from shore-normal to shore-parallel. The largest sediment flux occurred on the inner shelf to the east of Gustav's landfall location, where the longshore current was strong. Although the barrier islands have been removed in this case, the sediment fluxes through the offshore boundary of the estuaries were still small compared with the transport either inside the bay or on the adjacent continental shelf.

The relative difference in total transport rate can be defined as

$$\Delta M_{rel} = \frac{|M_{base}| - |M_{degrd}|}{|M_{base}|} \times 100\% \tag{5.6}$$

where $|M_{base}|$ and $|M_{degrd}|$ are the magnitude of sediment flux in the baseline model and the degradation model, respectively. Thus a positive ΔM_{rel} indicates a positive effect of barrier islands on sediment transport, while a negative value means a suppressive effect. A direct comparison of model results from the baseline configuration and the degradation configuration gave the relative change of sediment flux at the Terrebonne and Barataria Basins (Figure 5.18). In general, the degradation of barrier islands enhanced the sediment transport through overtopping

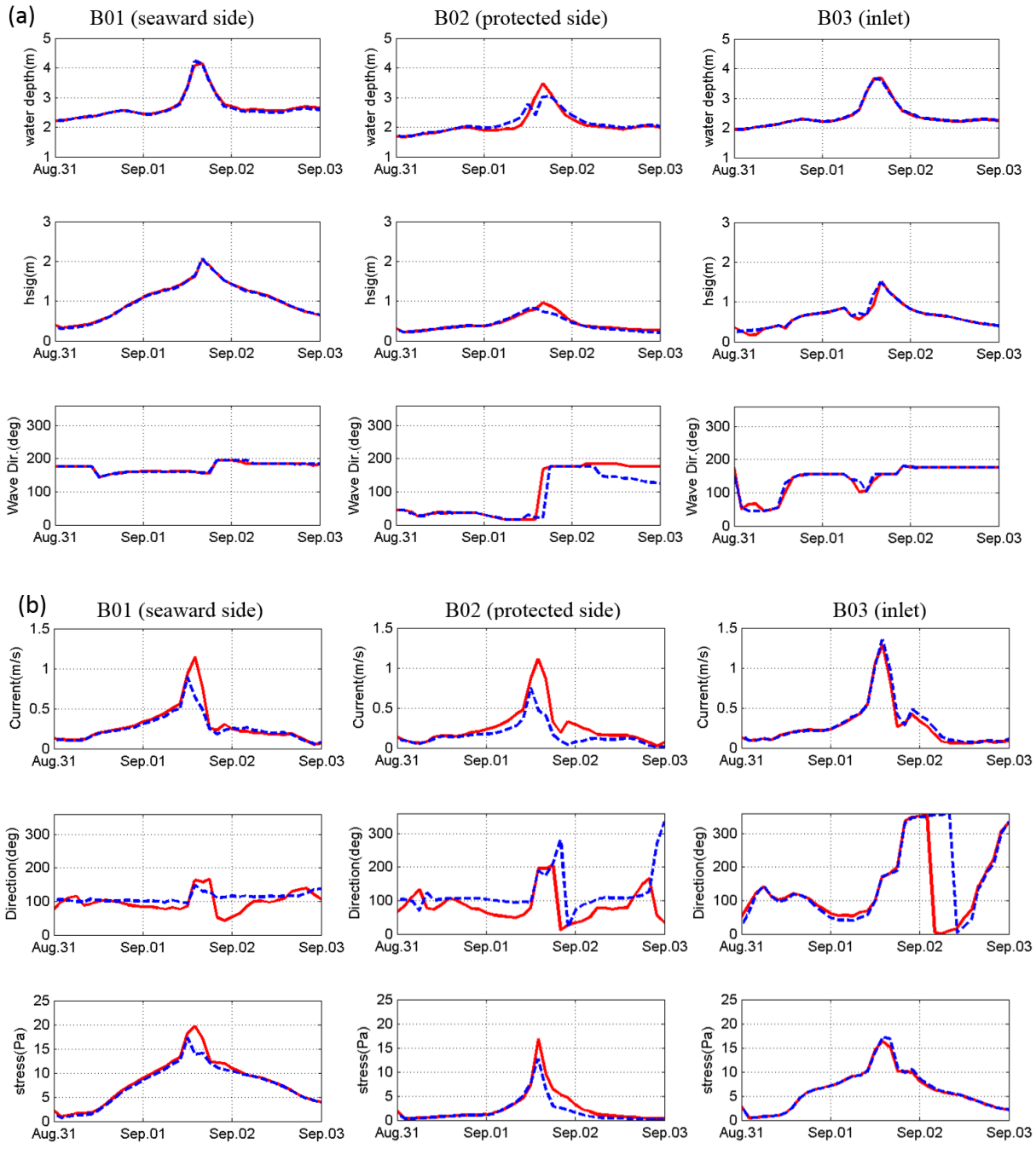

FIGURE 5.16: Time series of wave height and direction (a), current speed and direction, and bed shear stress (b) at observation points B01, B02 and B03 (defined in Figure 5.10) (blue dashed line: baseline configuration; red solid line: degradation configuration)

TABLE 5.4: The effects of barrier islands on sediment redistribution: Terrebonne

Transport Components	Baseline Configuration	Degradation Configuration	Relative Change
transport from inner shelf to bay (MMT)	6.47	6.87	+6.18%
transport from bay to wetland (MMT)	7.46	7.96	+6.70%
net deposition on wetland, TDW (MMT)	7.74	8.07	+4.26%
percentage of deposition from the bay, PB (%)	96.9	98.6	+1.75%

the islands, but the transport through the previously existing narrow inlets between the islands dropped. The relative change in the sediment flux could be as much as $\pm 50\%$ near the barrier islands.

The sediment fluxes through the entire cross-section T1/T2/B1/B2 (defined in Figure 4.8) were integrated over the hurricane event, from 08/28/2008 to 09/05/2008, and some components of the net transport in the Terrebonne and Barataria Basins were listed in Table 5- 4 and Table 5- 5. In the degradation scenario, the sediment transport from the inner shelf to Terrebonne Bay and that from Terrebonne Bay to wetlands increased by 6.18% and 6.70% compared with the baseline case. The net deposition on wetlands increased by 4.26% while the percentage of deposition originating from the bay was nearly unchanged in the degradation scenario for Terrebonne Bay. In Barataria Bay, although the transport from the shelf to the open bay decreased by 10.0%, the transport from the bay to wetlands and the net deposition on wetlands increased by 8.13% and 8.73%, respectively.

5.5.4 Summary

The impact of barrier islands on hurricane hydrodynamics and sediment redistribution was examined by comparing 3D simulations of hurricane hydrodynamics and sediment transport during Hurricane Gustav with different configurations for the barrier island chains in Terrebonne Bay and Barataria Bay. Numerical simulations showed that the degradation of barrier islands

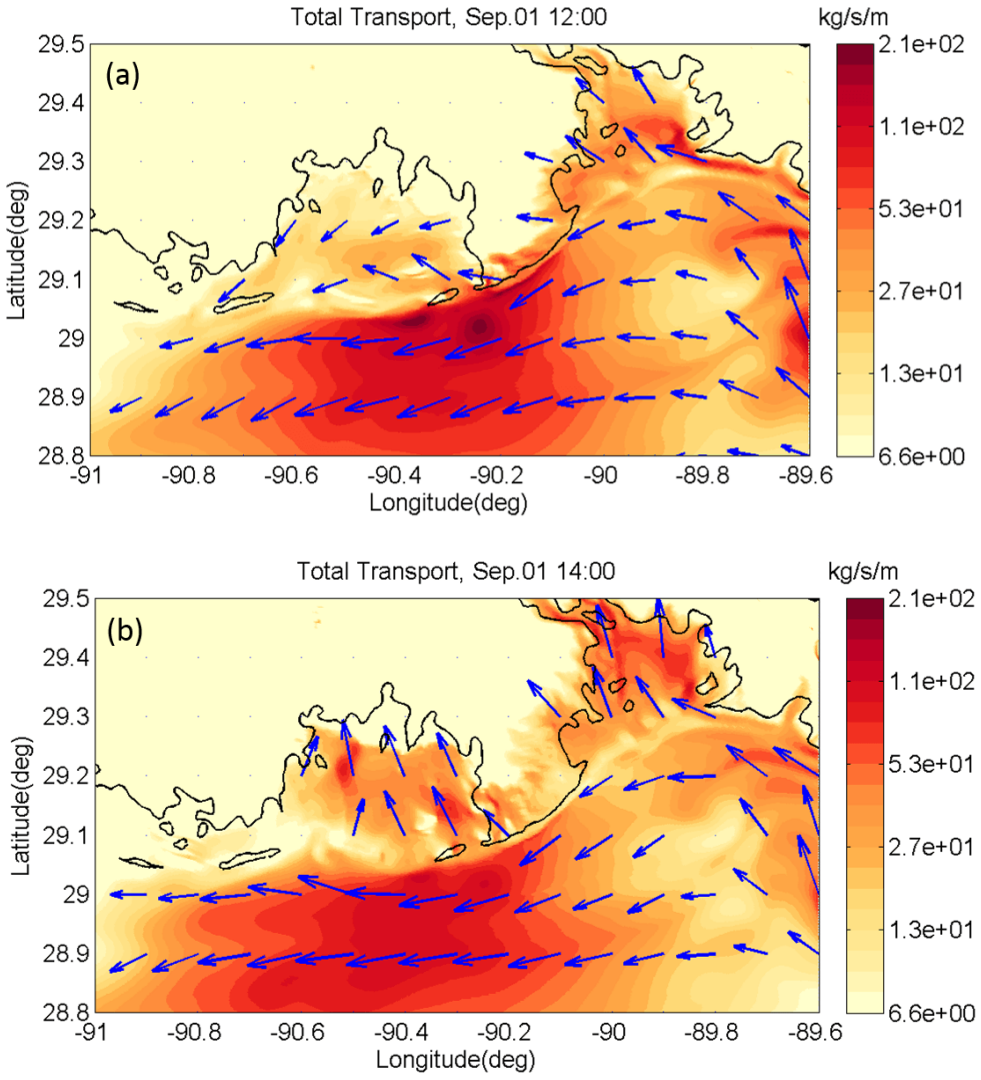

FIGURE 5.17: The total transport of the summation of all the sediment classes from degradation configuration when Gustav (2008) was making landfall: (a) 12:00 UTC, Sep 01, or approximately 2 hours before landfall, (b) 14:00 UTC, Sep 01, or approximately landfall.

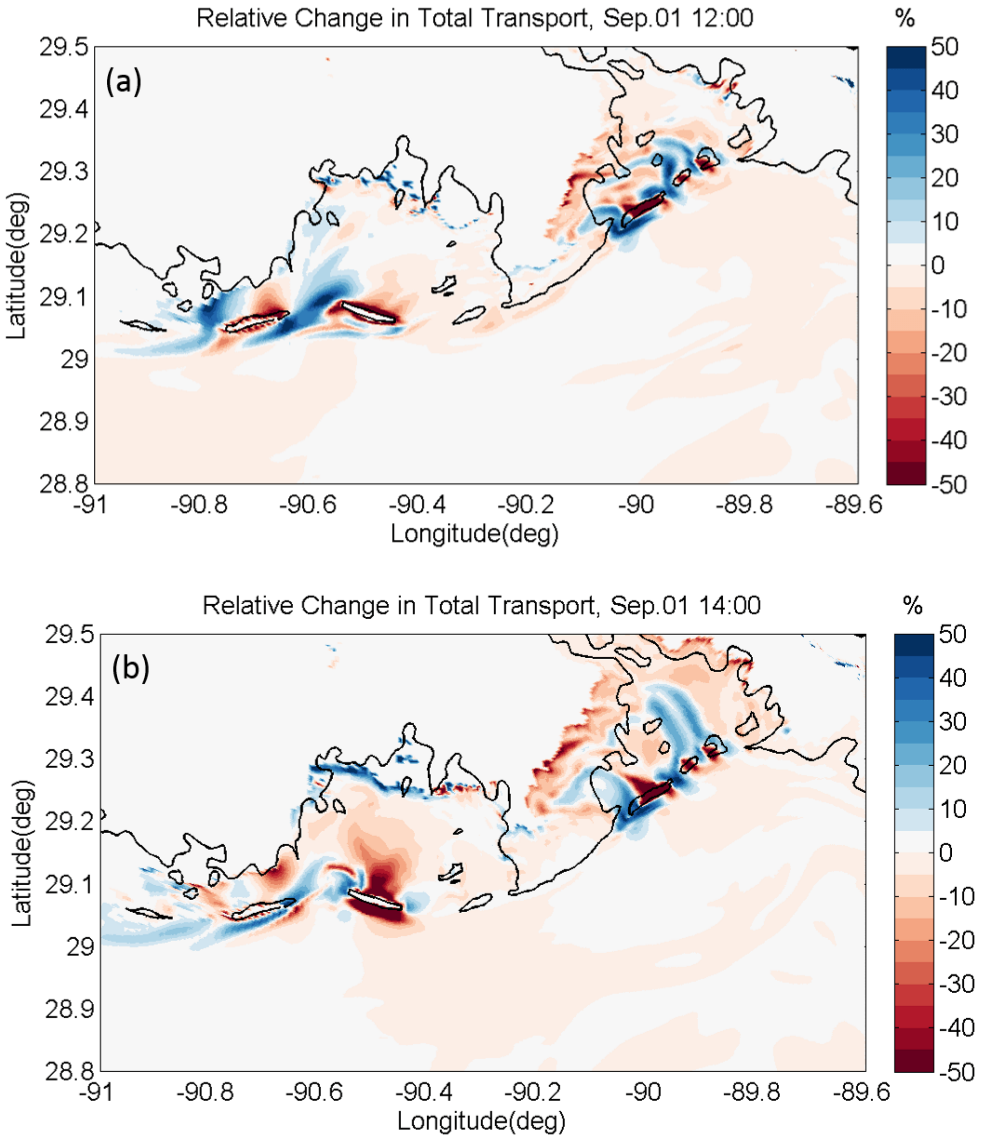

FIGURE 5.18: The relative difference of the magnitude of total transport between the baseline configuration and the degradation configuration: Times (a)-(b) are as in Figure 5.17

TABLE 5.5: The effects of barrier islands on sediment redistribution: Barataria

Transport Components	Baseline Configuration	Degradation Configuration	Relative Change
transport from inner shelf to bay (MMT)	2.20	1.98	-10.0%
transport from bay to wetland (MMT)	12.3	13.3	+8.13%
net deposition on wetland, TDW (MMT)	12.6	13.7	+8.73%
percentage of deposition from the bay, PB (%)	97.6	97.1	-0.51%

resulted in an increase of storm surge on the protected side of the islands, and the increase was more than 0.1 m in most area in the estuaries. The maximum wave height in the estuaries also exhibited an increase in the degradation configuration during the hurricane, but the influence was limited in the area immediately behind the barrier islands.

Since the barrier islands could obstruct current from flowing into the estuaries, more sediment transport from the shelf to the bays and a larger contribution of marine sediment to the wetland deposition might be expected in the degradation configuration. From the model results, the exact impact turned out to be insignificant. With the hypothetical deterioration of barrier islands, model results showed that the onshore transport through overtopping the islands was enhanced while the transport through the previously existing narrow inlets was decreased. The net effect on sediment trasnport from the shelf to the bays varied by location. In Terrebonne Bay, the net transport from the inner shelf to the bay and from the bay to wetlands both slightly increased. In Barataria Bay, in contrast, the transport from the shelf to the bay decreased by 10%. Despite all these changes in sediment fluxes in the shelf-bay-wetland system as the barrier islands were removed, the net deposition on wetlands only showed a slight increase of 4.26% and 8.73% for Terrebonne and Barataria, and the degradation scenario did not change the fact that most of the deposited material on coastal wetland originated from the bay.

The above analysis provides valuable information on the trend of the change of large-scale hurricane-induced sediment transport in response to topography change in the coastal zone, but should not be taken as a definitive quantitative assessment of the impact of barrier islands. The exact benefits of barrier islands in reducing storm surge and waves and altering sediment transport could vary significantly with hurricane parameters (including hurricane track, intensity and approaching angle), the crest height of the islands relative to the surge level, the bathymetry in the adjacent estuary and continental shelf, even the distance from the islands to the mainland (Wamsley et al., 2009; Cobell et al., 2013). The accuracy of the modeled effects of barrier islands was also limited by the relatively coasre mesh, which has only three to four grid points across the islands in the shore-normal direction. In addition, the passage of hurricanes could cause severe morphological effects on the barrier islands, for example, channel incisions, dune scarps, and overwash fans, which were not considered in this study. A larger set of storm parameters and a better representation of different barrier island topography using higher-resolution local grid are desired for future study.

CHAPTER 6 SUMMARY AND CONCLUSIONS

In this study, we developed a coupled modeling system integrating hurricane winds, storm surge, waves and sediment transport to explore the hurricane-induced large-scale sediment dynamics and morphodynamics on Louisiana coast. Through comprehensive numerical simulations, we demonstrated that a major hurricane event has the ability to deliver a considerable amount of sediment to the coastal wetlands. In addition to a quantitative prediction of the total deposition, the numerical modeling system also helped us to understand where the observed sediment accretion came from and how the barrier islands could affect the sediment exchange in the shelf-bay-wetland system.

In Chapter 2, wind effects in wave nonlinearities in shallow water were studied using a combination of analytical and numerical methods. First, wind effects were incorporated into a Boussinesq-type wave model as a pressure variation on water surface following the classic sheltering mechanism by Jeffreys (1925). Then, based on the obtained Boussinesq Model With Wind (BMWW), a set of EVolution equations for the first Three Harmonics (EVTH) was derived for constant water depth with one-dimensional winds using the multi-scale expansion. We solved EVTH using a fourth-order Range-Kutta method, and the numerical solution for a small amplitude wave in a wave tank was validated against the laboratory measurements in Chapalain et al. (1992). The EVTH provides an analytical tool to understand wind effects on wave triad interactions in shallow water. The BMWW allows us to take wind into account when simulating nearshore processes, which is highly needed under some extreme conditions such as hurricanes and storms.

The EVTH and the BMWW were applied to study the wind effects on wave triad interactions in shallow water. Results from both methods consistently showed that following winds tended to increase the amplitude of all the harmonics, while opposing winds did the opposite (decreased the amplitude of all the harmonics). The mechanism of energy transfer from winds

to high harmonics was illustrated by a fast growth of the second harmonic. Results indicated that the following winds infused energy directly into high harmonics in addition to raising the primary wave and growing higher harmonics through an indirect transfer from the primary wave to free triads.

During wave shoaling, both bounded and free high harmonic waves are generated. The wind effects on wave shoaling were studied by numerical simulation with BMWW. The model predicted an increased wave height and a wind-induced shape change, similar to the observation in a laboratory wave flume by Feddersen and Veron (2005). In general, onshore winds amplify triad interactions while offshore winds suppress it. Another finding was that the triad interactions could influence the wave shape during the shoaling process and the wave skewness and wave asymmetry varied periodically on the slope in a cycle similar to the triad interactions. That might explain the difference in the wave shape sensitivity to winds at different locations reported by Feddersen and Veron (2005).

An accurate prediction of storm surge and hurricane waves is imperative to the simulation of hurricane-induced sediment transport. In Chapter 3, a hydrodynamic model for Hurricane Gustav (2008) was developed using Delft3D. In order to better resolve the complex geometry, a nested two-layer curvilinear mesh was designed for the Louisiana coast. The Gulf of Mexico mesh covered the Gulf of Mexico, the Caribbean Sea and part of the western North Atlantic Ocean to capture the development of the fast-moving hurricane and provide accurate boundary condition to the detailed domain. The nested domain (LA mesh) covered the entire Louisiana coast with 200 to 500 m resolution in coastal wetlands and lakes. The surge and waves were driven by a hurricane wind field from a parametric wind model and running in a fully-coupled way to simulate the interaction of surge and waves in the nearshore region. Vegetation plays an important role in the wetland hydrodynamics. In the surge model, the vegetation effects were represented as an extra drag force in the momentum equation (Baptist, 2005), and in the wave

model, the vegetation-induced wave attenuation was modeled as a friction-type dissipation in the wave action balance equation (Madsen et al., 1988).

We collected observation data for the storm surge and surface waves during Hurricane Gustav and validated the models using the observation data. Offshore, the wave predictions agreed well with the observations at NDBC wave gauges in the Gulf of Mexico, which validated the stand-alone wave model and the hurricane wind field. In the nearshore region, surge and wave interactions became important, and the coupled surge and wave model predicted surge level fairly well in comparison with the water level measurements from various sources, including NOAA tides and current stations in the coastal water and CRMS stations on the wetlands. Measurements for nearshore waves were also available at a limited number of wave gauges. The modeled wave heights and wave periods were in reasonable agreement with the observations. The statistics for the agreement between model results and the measurement data showed good accuracy and gave us confidence in applying the coupled surge and wave models to the study of hurricane-induced sediment transport.

In Chapter 4, the limited understanding of hurricane-induced sedimentation on coastal wetlands was expanded by coupling the sediment transport model with the validated storm surge and wave models for Hurricane Gustav. Two sediment classes, mud and sand, were considered in the sediment transport model. The initial composition of each class was interpolated in the model domain from the usSEABED dataset. The simulations showed that during a hurricane event, the sediment suspension and redistribution mainly occurred to cohesive sediment on the mud-dominant Louisiana coast; in contrast, the transport of sand was relatively negligible during the hurricane.

Large uncertainties exist in some of the sediment properties. In the sediment transport model, we set the range of settling velocity, erosion rate and critical shear stress based on sediment transport models for coastal Louisiana in the literature. A baseline configuration was de-

termined by comparing the modeled basin-average sediment accretion with the measurements of fresh deposition in the Terrebonne and Barataria Basins after Gustav by Tweel and Turner (2012), and the uncertainty analysis suggested that the variability of the erosion rate constituted the major part of the variance in the predicted deposition on wetlands. From the baseline configuration, the sediment deposition to coastal wetlands in the Terrebonne and Barataria Basins during Gustav was about 25.6 MMT, and the 5% and 95% percentile interval was [3.8, 174] MMT.

The long-existing hypothesis about the source of deposition on wetlands was verified via numerical simulation for the first time. Our model results indicated that the observed deposition on wetlands was mostly suspended material from the coastal bays, which was independent of the exact value of sediment properties within the range of our experiments but rather determined by the transport capability (onshore transport distance) of the storm surge. During this large-scale sediment transport and redistribution caused by Hurricane Gustav, Terrebonne Bay and Barataria Bay acted as a major source of sediment for the deposition on the adjacent coastal wetlands. Numerical simulations also suggested that a sediment exchange occurred at the inlets of Terrebonne Bay and Barataria Bay as surge water flooded into and receded from the estuaries, although they did not contribute to the deposition on the wetlands directly.

Compared with depth-averaged models, three-dimensional (3D) models have some inherent advantages. In Chapter 5, the depth-averaged version of the storm surge, wave and sediment transport modeling system was extended into a three-dimensional one with seven vertical layers. In most of the nearshore regions, including the estuaries, the 3D model results suggested a significant vertical variation of current velocity, and the bottom velocity was generally smaller than the depth-averaged one. On the east side of the hurricane track (close to the landfall location), where the longshore current on the continental shelf was the strongest, water was better mixed than in the rest of the domain. The 3D model was validated against the collected dataset for

surge and waves, and the statistics showed that, with minimum calibration, the 3D model could achieve the same level of accuracy in hydrodynamic results as the 2D model. When keeping the sediment properties the same, the 3D model and the 2D model predicted similar sediment movement among the shelf-bay-wetland system, except that the magnitude of sediment flux was smaller in the 3D model, which could be a result of a smaller erosion forcing on the bed and thus a smaller sediment load in the 3D model. In total, the 3D model predicted the net sedimentation on the coastal wetlands to be 7.74 MMT in Terrebonne and 12.63 MMT in Barataria, and most of the deposited material came from suspension in the bay, which was consistent with the findings using the 2D model. In other words, although some difference existed in the sediment concentration and vertical velocity profile, the basic conclusions about the large-scale sediment redistribution did not change regardless of the dimensionality of the numerical model.

The three-dimensional modeling system then served as a benchmark to study the impact of barrier islands on hurricane hydrodynamics and sediment redistribution during the hurricane event. By comparing the results from the baseline configuration and the hypothetical degradation configuration, we found that the degradation of barrier islands resulted in an increase of storm surge on the protected side of the islands, and the increase was more than 0.1 m in most parts of Terrebonne Bay and Barataria Bay during Hurricane Gustav. The maximum wave height in the estuaries also exhibited an increase in the degradation configuration, but the influence was limited in the area immediately behind the barrier islands.

Since the barrier islands could block the strong currents from flowing into the estuaries, a larger sediment flux from the shelf to the bays and potentially more onshore transport to the wetlands could be expected with the hypothetical deterioration of barrier islands. But it turns out not always to be the cases. The model results showed that in the degradation configuration, the onshore transport through overtopping the islands was enhanced while the transport through the narrow inlets between islands was suppressed. In Terrebonne Bay, the sediment transport

both from the inner shelf to the bay and that from the bay to the wetlands slightly increased. In Barataria Bay, the transport from the shelf to the bay decreased by 10% due to the change of sediment flux at the inlets. Despite all these changes in the sediment fluxes in the shelf-bay-wetland system as the barrier islands were removed, the net deposition on wetlands showed only a slight increase of 4.26% for Terrebonne and 8.73% for Barataria. The hypothetical degradation of barrier islands did not change the finding that the suspension of bed material from the estuaries contributed most of the deposited sediment on the wetlands in the Terrebonne and Barataria Basins.

There is no faith in model perfectibility. Some morphodynamic processes on wetlands may still be missing from the model. For example, observations indicated that a hurricane could dramatically change the vegetation covering on marsh surface and alter the resistance to erosion of wetlands. Although our model results showed the deposition was dominant on wetlands, how to model the dynamics erosional process and whether the local erosion on marsh erosion affects the distribution of hurricane-induced deposition have yet to be explored. Model results in this study also indicated that the choice of parameters for sediment properties could strongly influence the magnitude of the predicted deposition on wetlands. But unfortunately, to precisely measure these properties is not a trivial endeavor. Not to mention that a spatial distribution of such properties is needed in a large-scale model. Future efforts to better link the on-going field studies with model parameters will be very helpful for improving the model predictive skill. In the era of climate change, more frequent storm activities and more intensive extreme weather are expected to come in the Gulf Coast, and hurricanes could form through different tracks. Whether our findings still hold true for hurricanes with different approaching angles, landfall locations, and intensities remains to be further tested.

REFERENCES

Agnon, Y. and Sheremet, A. (1997). "Stochastic nonlinear shoaling of directional spectra." *Journal of Fluid Mechanics*, 345, 79–99.

Andrews, D. G. and McIntyre, M. (1978). "An exact theory of nonlinear waves on a Lagrangian-mean flow." *Journal of Fluid Mechanics*, 89(04), 609–646.

Baptist, M. (2003). "A flume experiment on sediment transport with flexible, submerged vegetation." *International workshop on riparian forest vegetated channels: hydraulic, morphological and ecological aspects, RIPFOR, Trento, Italy*.

Baptist, M. J. (2005). "Modelling floodplain biogeomorphology." Ph.D. thesis, Delft University of Technology.

Battjes, J. and Beji, S. (1992). "Breaking waves propagating over a shoal." *Coastal Engineering Proceedings*, 1(23).

Blaas, M., Dong, C., Marchesiello, P., McWilliams, J. C., and Stolzenbach, K. D. (2007). "Sediment-transport modeling on southern Californian shelves: A ROMS case study." *Continental Shelf Research*, 27(6), 832–853.

Boczar-Karakiewicz, B., Bona, J., and Cohen, D. (1986). *Interaction of shallow-water waves and bottom topography*. Inst. for Mathematics and its Applications, University of Minnisota.

Boczar-Karakiewicz, B. and Davidson-Arnott, R. G. (1987). "Nearshore bar formation by non-linear wave processes – A comparison of model results and field data." *Marine Geology*, 77(3), 287–304.

Booij, N., Ris, R., and Holthuijsen, L. H. (1999). "A third-generation wave model for coastal regions: 1. model description and validation." *Journal of Geophysical Research: Oceans*, 104(C4), 7649–7666.

Borsje, B. W., Hulscher, S. J. M. H., Herman, P. M. J., and De Vries, M. B. (2009). "On the parameterization of biological influences on offshore sand wave dynamics." *Ocean Dynamics*, 59(5), 659–670.

Bouma, T., Van Duren, L., Temmerman, S., Claverie, T., Blanco-Garcia, A., Ysebaert, T., and Herman, P. (2007). "Spatial flow and sedimentation patterns within patches of epibenthic structures: Combining field, flume and modelling experiments." *Continental Shelf Research*, 27(8), 1020–1045.

Bradford, S. F. (2000). "Numerical simulation of surf zone dynamics." *Journal of Waterway, Port, Coastal, and Ocean Engineering*, 126(1), 1–13.

Brocchini, M. (2013). "A reasoned overview on Boussinesq-type models: the interplay between physics, mathematics and numerics." *Proceedings of the Royal Society A: Mathematical, Physical and Engineering Science*, 469(2160), 20130496.

Bryant, P. J. (1973). "Periodic waves in shallow water." *Journal of Fluid Mechanics*, 59(4), 625–644.

Cahoon, D., Day Jr, J., Reed, D., and Young, R. (1998). "Global climate change and sea-level rise: estimating the potential for submergence of coastal wetlands." *Vulnerability of Coastal Wetlands in the Southeastern United States: Climate Change Research Results*, 21–35.

Cahoon, D. R. (2003). "Storms as agents of wetland elevation change: their impact on surface and subsurface sediment processes." *Proceedings of the International Conference on Coastal Sediments*, 18–23.

Cahoon, D. R., Day Jr, J. W., and Reed, D. J. (1999). "The influence of surface and shallow subsurface soil processes on wetland elevation: A synthesis." *Current Topics in Wetland Biogeochemistry*, 3, 72–88.

Cahoon, D. R., Reed, D. J., Day Jr, J. W., Steyer, G. D., Boumans, R. M., Lynch, J. C., McNally, D., and Latif, N. (1995). "The influence of Hurricane Andrew on sediment distribution in Louisiana coastal marshes." *Journal of Coastal Research*, 280–294.

Chambarel, J., Kharif, C., and Kimmoun, O. (2010). "Generation of two-dimensional steep water waves on finite depth with and without wind." *European Journal of Mechanics-B/Fluids*, 29(2), 132–142.

Chamberlain, J. (1959). "Influence of Hurricane Audrey on the coastal marsh of southwestern Louisiana." *Report No. TR-10-Pt-B*, DTIC Document.

Chapalain, G., Cointe, R., and Temperville, A. (1992). "Observed and modeled resonantly interacting progressive water-waves." *Coastal Engineering*, 16(3), 267–300.

Chen, Q., Kaihatu, J. M., and Hwang, P. A. (2004). "Incorporation of wind effects into Boussinesq wave models." *Journal of Waterway, Port, Coastal, and Ocean Engineering*, 130(6), 312–321.

Chen, Q., Madsen, P. A., and Basco, D. R. (1999). "Current effects on nonlinear interactions of shallow-water waves." *Journal of Waterway, Port, Coastal, and Ocean Engineering*, 125(4), 176–186.

Chen, Q., Wang, L., and Tawes, R. (2008). "Hydrodynamic response of northeastern Gulf of Mexico to hurricanes." *Estuaries and Coasts*, 31(6), 1098–1116.

Cobell, Z., Zhao, H., Roberts, H. J., Clark, F. R., and Zou, S. (2013). "Surge and wave modeling for the Louisiana 2012 Coastal Master Plan." *Journal of Coastal Research*, 67(sp1), 88–108.

Costanza, R., Farber, S. C., and Maxwell, J. (1989). "Valuation and management of wetland ecosystems." *Ecological Economics*, 1(4), 335–361.

Couvillion, B. R., Barras, J. A., Steyer, G. D., Sleavin, W., Fischer, M., Beck, H., Trahan, N., Griffin, B., and Heckman, D. (2011). "Land area change in coastal Louisiana from 1932 to 2010." *U.S. Geological Survey Scientific Investigation Map 3164*.

Couvillion, B. R., Steyer, G. D., Wang, H., Beck, H. J., and Rybczyk, J. M. (2013). "Forecasting the effects of coastal protection and restoration projects on wetland morphology in coastal Louisiana under multiple environmental uncertainty scenarios." *Journal of Coastal Research*, 67(sp1), 29–50.

D'Alpaos, A., Lanzoni, S., Marani, M., and Rinaldo, A. (2007). "Landscape evolution in tidal embayments: modeling the interplay of erosion, sedimentation, and vegetation dynamics." *Journal of Geophysical Research: Earth Surface*, 112(F1).

Dean, R. G. and Dalrymple, R. A. (1991). *Water wave mechanics for engineers and scientists*. World Scientific.

Deltares (2012). *User manual Delft3D-FLOW*. Deltares, Delft.

Dietrich, J. C., Westerink, J., Kennedy, A., Smith, J., Jensen, R., Zijlema, M., Holthuijsen, L., Dawson, C., Luettich Jr, R., Powell, M., et al. (2011). "Hurricane Gustav (2008) waves and storm surge: hindcast, synoptic analysis, and validation in southern Louisiana." *Monthly Weather Review*, 139(8), 2488–2522.

Dingemans, M. W. (1997). *Water wave propagation over uneven bottoms. Part2: Non-linear wave propagation*. World Scientific.

Douglass, S. L. (1990). "Influence of wind on breaking waves." *Journal of Waterway, Port, Coastal, and Ocean Engineering*, 116(6), 651–663.

Edmonds, D. A. and Slingerland, R. L. (2010). "Significant effect of sediment cohesion on delta morphology." *Nature Geoscience*, 3(2), 105–109.

Egbert, G. D., Bennett, A. F., and Foreman, M. G. (1994). "Topex/poseidon tides estimated using a global inverse model." *Journal of Geophysical Research*, 99(C12), 24,821–24,852.

Egbert, G. D. and Erofeeva, S. Y. (2002). "Efficient inverse modeling of barotropic ocean tides." *Journal of Atmospheric and Oceanic Technology*, 19(2), 183–204.

Eldeberky, Y. and Battjes, J. A. (1995). "Parameterization of triad interactions in wave energy models." *Coastal Dynamics '95*, W. R. Dally and R. B. Zeidler, eds., ASCE, 140–148.

Elgar, S., Freilich, M., and Guza, R. (1990). "Recurrence in truncated Boussinesq models for nonlinear waves in shallow water." *Journal of Geophysical Research: Oceans (1978–2012)*, 95(C7), 11547–11556.

Elgar, S., Gallagher, E. L., and Guza, R. (2001). "Nearshore sandbar migration." *Journal of Geophysical Research: Oceans (1978–2012)*, 106(C6), 11623–11627.

Feddersen, F. and Veron, F. (2005). "Wind effects on shoaling wave shape." *Journal of Physical Oceanography*, 35(7).

Fredsøe, J. and Deigaard, R. (1992). *Mechanics of coastal sediment transport*, Vol. 3. World scientific.

Freeman, A. M., Jose, F., Roberts, H. H., and Stone, G. W. (2015). "Storm induced hydrodynamics and sediment transport in a coastal Louisiana lake." *Estuarine, Coastal and Shelf Science*, 161, 65–75.

Freilich, M. H. and Guza, R. T. (1984). "Nonlinear effects on shoaling surface gravity waves." *Philosophical Transactions of the Royal Society of London. Series A, Mathematical and Physical Sciences*, 311(1515), 1–41.

Groeneweg, J. and Klopman, G. (1998). "Changes of the mean velocity profiles in the combined wave–current motion described in a glm formulation." *Journal of Fluid Mechanics*, 370, 271–296.

Grzegorzewski, A. S., Cialone, M. A., and Wamsley, T. V. (2011). "Interaction of barrier islands and storms: implications for flood risk reduction in Louisiana and Mississippi." *Journal of Coastal Research*, 156–164.

Hansen, J. B. and Svendsen, I. A. (1974). "Laboratory generation of waves of constant form." *Coastal Engineering Proceedings*, 1(14).

Hoefel, F. and Elgar, S. (2003). "Wave-induced sediment transport and sandbar migration." *Science*, 299(5614), 1885–1887.

Horstman, E., Dohmen-Janssen, C., Bouma, T., and Hulscher, S. (2015). "Tidal-scale flow routing and sedimentation in mangrove forests: combining field data and numerical modelling." *Geomorphology*, 228, 244–262.

Horstman, E., Dohmen-Janssen, C., and Hulscher, S. (2013). "Modeling tidal dynamics in a mangrove creek catchment in Delft3D." *The Proceedings of Coastal Sediments 2013*, World Scientific.

Houser, C., Hapke, C., and Hamilton, S. (2008). "Controls on coastal dune morphology, shoreline erosion and barrier island response to extreme storms." *Geomorphology*, 100(3), 223–240.

Hu, K., Chen, Q., and Kimball, S. K. (2012). "Consistency in hurricane surface wind forecasting: an improved parametric model." *Natural Hazards*, 61(3), 1029–1050.

Hu, K., Chen, Q., and Wang, H. (2015). "A numerical study of vegetation impact on reducing storm surge by wetlands in a semi-enclosed estuary." *Coastal Engineering*, 95, 66–76.

Hughes, Z., Weathers, D., Georgiou, I., FitzGerald, D., and Kulp, M. (2012). *Barrier island morphology model technical report (Appendix D-3). In: Louisiana's Comprehensive Master Plan for a Sustainable Coast, Louisiana*. Coastal Protection and Restoration Authority.

Jeffreys, H. (1925). "On the formation of water waves by wind." *Proceedings of the Royal Society of London. Series A*, 107(742), 189–206.

Kaihatu, J. M. (2009). "Application of a nonlinear frequency domain wave current interaction model to shallow water recurrence effects in random waves." *Ocean Modelling*, 26(34), 190 – 205.

Kaihatu, J. M. and Kirby, J. T. (1995). "Nonlinear transformation of waves in finite water depth." *Physics of Fluids (1994-present)*, 7(8), 1903–1914.

Kaihatu, J. M., Veeramony, J., Edwards, K. L., and Kirby, J. T. (2007). "Asymptotic behavior of frequency and wave number spectra of nearshore shoaling and breaking waves." *Journal of Geophysical Research: Oceans (1978–2012)*, 112(C6).

Keen, T. R., Bentley, S. J., Vaughan, W. C., and Blain, C. A. (2004). "The generation and preservation of multiple hurricane beds in the northern Gulf of Mexico." *Marine Geology*, 210(1), 79–105.

Kennedy, A. B., Gravois, U., Zachry, B., Luettich, R., Whipple, T., Weaver, R., Fleming, F., Chen, Q., and Avissar, R. (2010). "Rapidly installed temporary gauging for hurricane waves and surge, and application to Hurricane Gustav." *Continental Shelf Research*, 30(16), 1743–1752.

Kesel, R. H. (1988). "The decline in the suspended load of the lower Mississippi River and its influence on adjacent wetlands." *Environmental Geology and Water Sciences*, 11(3), 271–281.

Kesel, R. H. (1989). "The role of the Mississippi River in wetland loss in southeastern Louisiana, USA." *Environmental Geology and Water Sciences*, 13(3), 183–193.

Kesel, R. H., Yodis, E. G., and McCraw, D. J. (1992). "An approximation of the sediment budget of the lower Mississippi River prior to major human modification.." *Earth Surface Processes and Landforms*, 17(7), 711–722.

Kharif, C., Giovanangeli, J.-P., Touboul, J., Grare, L., and Pelinovsky, E. (2008). "Influence of wind on extreme wave events: experimental and numerical approaches." *Journal of Fluid Mechanics*, 594, 209–247.

Kirby, J. T. (2003). "Boussinesq models and applications to nearshore wave propagation, surfzone processes and wave-induced currents." *Advances in Coastal Modeling*, 67, 1–41.

Kirby, J. T., Wei, G., Chen, Q., Kennedy, A. B., and Dalrymple, R. A. (1998). "FUNWAVE 1.0, fully nonlinear Boussinesq wave model documentation and users manual." *Report No. CACR-98-06*, Center for Applied Coastal Research, University of Delaware.

Kuiper, S. (2010). "Cross-shore morphological response on chaland headland due to Hurricanes Gustav and Ike." M.S. thesis, Delft University of Technology.

Lapetina, A. and Sheng, Y. P. (2015). "Simulating complex storm surge dynamics: Three-dimensionality, vegetation effect, and onshore sediment transport." *Journal of Geophysical Research: Oceans*, 120(11), 7363–7380.

Leadon, M. (2015). "Beach slope and sediment-grain-size trends as a basis for input parameters for the sbeach erosion model." *Journal of Coastal Research*, 31(6), 1375–1388.

Liu, K., Chen, Q., Hu, K., and Xu, K. (2015). "Numerical simulation of sediment deposition and erosion on Louisiana coast during Hurricane Gustav." *The Proceedings of the Coastal Sediments 2015*, World Scientific.

Madsen, A. and Schaffer, H. A. (1999). "A review of Boussinesq-type equations for surface gravity waves." *Advances in Coastal and Ocean Engineering*, 5, 1–94.

Madsen, O. S., Poon, Y.-K., and Graber, H. C. (1988). "Spectral wave attenuation by bottom friction: theory." *Coastal Engineering Proceedings*, 1(21).

Madsen, P. and Sørensen, O. (1993). "Bound waves and triad interactions in shallow water." *Ocean Engineering*, 20(4), 359–388.

Madsen, P. A., Murray, R., and Sørensen, O. R. (1991). "A new form of the Boussinesq equations with improved linear dispersion characteristics." *Coastal Engineering*, 15(4), 371–388.

McGee, B. D., Goree, B. B., Tollett, R. W., Woodward, B. K., and Kress, W. H. (2006). "Hurricane Rita surge data, southwestern Louisiana and southeastern Texas, September to November 2005." U.S. Geological Survey Data Series 220. (Available online at http://pubs.water.usgs.gov/ds220.)

McKee, K. L. and Cherry, J. A. (2009). "Hurricane Katrina sediment slowed elevation loss in subsiding brackish marshes of the Mississippi River Delta." *Wetlands*, 29(1), 2–15.

Mei, C. and Unluata, U. (1972). *Harmonic generation in shallow water waves*. R. E. Meyer, ed., Academic, New York.

Mitsch, W. and Gosselink, J. (1993). *Wetlands, 2nd*. Van Nostrand Reinhold, New York, USA.

Morgan, J. P., Nichols, L. G., and Wright, M. (1958). *Morphological effects of Hurricane Audrey on the Louisiana coast*. Coastal Studies Institute. Louisiana State University.

Morton, R. A. and Barras, J. A. (2011). "Hurricane impacts on coastal wetlands: a half-century record of storm-generated features from southern Louisiana." *Journal of Coastal Research*, 27(6A), 27–43.

Morton, R. A. and Sallenger Jr, A. H. (2003). "Morphological impacts of extreme storms on sandy beaches and barriers." *Journal of Coastal Research*, 560–573.

Mossa, J. (1996). "Sediment dynamics in the lowermost Mississippi River." *Engineering Geology*, 45(1), 457–479.

Mulligan, R. P., Walsh, J. P., and Wadman, H. M. (2014). "Storm surge and surface waves in a shallow lagoonal estuary during the crossing of a hurricane." *Journal of Waterway, Port, Coastal, and Ocean Engineering*, 141(4), A5014001.

Nyman, J., Crozier, C., and DeLaune, R. (1995). "Roles and patterns of hurricane sedimentation in an estuarine marsh landscape." *Estuarine, Coastal and Shelf Science*, 40(6), 665–679.

Partheniades, E. (1965). "Erosion and deposition of cohesive soils." *Journal of the Hydraulics Division*, 91(1), 105–139.

Penland, S., Boyd, R., and Suter, J. R. (1988). "Transgressive depositional systems of the Mississippi Delta Plain: a model for barrier shoreline and shelf sand development." *Journal of Sedimentary Re-*

search, 58(6), 932–949.

Phillips, N. A. (1957). "A coordinate system having some special advantages for numerical forecasting." *Journal of Meteorology*, 14(2), 184–185.

Reed, D. J. (1989). "Patterns of sediment deposition in subsiding coastal salt marshes, Terrebonne Bay, Louisiana: the role of winter storms." *Estuaries*, 12(4), 222–227.

Rejmanek, M., Sasser, C. E., and Peterson, G. W. (1988). "Hurricane-induced sediment deposition in a Gulf Coast marsh." *Estuarine, Coastal and Shelf Science*, 27(2), 217–222.

Richardson, J. and Zaki, W. (1954). "Sedimentation and fluidization." *Transaction Institution of Chemical Engineers*, 32, 35.

Ritchie, W. and Penland, S. (1988). "Rapid dune changes associated with overwash processes on the deltaic coast of south Louisiana." *Marine Geology*, 81(1), 97–122.

Roberts, H., Huh, O., Hsu, S., Rouse, L., and Rickman, D. (1987). "Impact of cold-front passages on geomorphic evolution and sediment dynamics of the complex Louisiana coast." *Coastal Sediments (1987)*.

Roth, D. (2010). *Louisiana Hurricane History*. National Weather Service.

Sallenger Jr, A. H. (2000). "Storm impact scale for barrier islands." *Journal of Coastal Research*, 890–895.

Sasser, C. E., Visser, J. M., Mouton, E., Linscombe, J., and Hartley, S. (2008). "Vegetation types in coastal Louisiana in 2007." *U.S. Geological Survey Open-File Report 2008-1224*.

Smith, J. E., Bentley, S. J., Snedden, G. A., and White, C. (2015). "What role do hurricanes play in sediment delivery to subsiding river deltas?." *Scientific reports*, 5.

Stelling, G. S. and Van Kester, J. A. T. M. (1994). "On the approximation of horizontal gradients in sigma co-ordinates for bathymetry with steep bottom slopes." *International Journal for Numerical Methods in Fluids*, 18(10), 915–935.

Stone, G. W. and McBride, R. A. (1998). "Louisiana barrier islands and their importance in wetland protection: forecasting shoreline change and subsequent response of wave climate." *Journal of Coastal Research*, 900–915.

Stone, G. W., Zhang, X., and Sheremet, A. (2005). "The role of barrier islands, muddy shelf and reefs in mitigating the wave field along coastal Louisiana." *Journal of Coastal Research*, 40–55.

Stumpf, R. P. (1983). "The process of sedimentation on the surface of a salt marsh." *Estuarine, Coastal and Shelf Science*, 17(5), 495–508.

Temmerman, S., Bouma, T., Govers, G., Wang, Z., De Vries, M., and Herman, P. (2005). "Impact of vegetation on flow routing and sedimentation patterns: Three dimensional modeling for a tidal marsh."

Journal of Geophysical Research: Earth Surface (20032012), 110(F4).

Turner, R. E., Baustian, J. J., Swenson, E. M., and Spicer, J. S. (2006). "Wetland sedimentation from Hurricanes Katrina and Rita." *Science*, 314(5798), 449–452.

Tweel, A. W. and Turner, R. E. (2012). "Landscape-scale analysis of wetland sediment deposition from four tropical cyclone events." *PloS One*, 7(11), e50528.

Tweel, A. W. and Turner, R. E. (2014). "Contribution of tropical cyclones to the sediment budget for coastal wetlands in Louisiana, USA." *Landscape ecology*, 29(6), 1083–1094.

Uittenbogaard, R. (2003). "Modelling turbulence in vegetated aquatic flows." *International workshop on RIParian FORest vegetated channels: hydraulic, morphological and ecological aspects*, 20–22.

van de Plassche, O., Erkens, G., van Vliet, F., Brandsma, J., van der Borg, K., and de Jong, A. F. (2006). "Salt-marsh erosion associated with hurricane landfall in southern New England in the fifteenth and seventeenth centuries." *Geology*, 34(10), 829–832.

Van der Wegen, M. and Roelvink, J. (2008). "Long-term morphodynamic evolution of a tidal embayment using a two-dimensional, process-based model." *Journal of Geophysical Research: Oceans*, 113(C3).

van der Westhuysen, A. J., Zijlema, M., and Battjes, J. A. (2007). "Nonlinear saturation-based whitecapping dissipation in SWAN for deep and shallow water." *Coastal Engineering*, 54(2), 151–170.

van Rijn, L. C. (1993). *Principles of sediment transport in rivers, estuaries and coastal seas*, Vol. 1006. Aqua publications Amsterdam.

Vatvani, D., Zweers, N., Ormondt, M. v., Smale, A., Vries, H. d., and Makin, V. (2012). "Storm surge and wave simulations in the Gulf of Mexico using a consistent drag relation for atmospheric and storm surge models." *Natural Hazards and Earth System Science*, 12(7), 2399–2410.

Visser, J. (2007). "Hydrologic characteristics of louisiana's coastal wetland vegetation. literature summary for URS group, inc.." Louisiana State University.

Walstra, D., Roelvink, J., and Groeneweg, J. (2001). "Calculation of wave-driven currents in a 3d mean flow model." *Coastal Engineering Conference*, Vol. 2, 1050–1063.

Wamsley, T. V., Cialone, M. A., Smith, J. M., Ebersole, B. A., and Grzegorzewski, A. S. (2009). "Influence of landscape restoration and degradation on storm surge and waves in southern Louisiana." *Natural Hazards*, 51(1), 207–224.

Wang, P., Kirby, J. H., Haber, J. D., Horwitz, M. H., Knorr, P. O., and Krock, J. R. (2006). "Morphological and sedimentological impacts of Hurricane Ivan and immediate poststorm beach recovery along the northwestern Florida barrier-island coasts." *Journal of Coastal Research*, 1382–1402.

Warner, J. C., Butman, B., and Dalyander, P. S. (2008). "Storm-driven sediment transport in massachusetts bay." *Continental Shelf Research*, 28(2), 257–282.

Wegen, M. (2013). "Numerical modeling of the impact of sea level rise on tidal basin morphodynamics." *Journal of Geophysical Research: Earth Surface*, 118(2), 447–460.

Williams, S., Arsenault, M., Buczkowski, B., Reid, J., Flocks, J., Kulp, M., Penland, S., and Jenkins, C. (2006). "Surficial sediment character of the Louisiana offshore continental shelf region: a GIS compilation." *U.S. Geological Survey Open-File Report 2006-1195*.

Wright, L., Sherwood, C., and Sternberg, R. (1997). "Field measurements of fairweather bottom boundary layer processes and sediment suspension on the Louisiana inner continental shelf." *Marine Geology*, 140(3), 329–345.

Xie, Z. (2014). "Numerical modelling of wind effects on breaking solitary waves." *European Journal of Mechanics-B/Fluids*, 43, 135–147.

Xu, K., Harris, C. K., Hetland, R. D., and Kaihatu, J. M. (2011). "Dispersal of Mississippi and Atchafalaya sediment on the Texas-Louisiana shelf: Model estimates for the year 1993." *Continental Shelf Research*, 31(15), 1558–1575.

Xu, K., Mickey, R. C., Chen, Q., Harris, C. K., Hetland, R. D., Hu, K., and Wang, J. (2016). "Shelf sediment transport during hurricanes Katrina and Rita." *Computers & Geosciences*, 90, 24–39.

Yan, S. and Ma, Q. (2011). "Improved model for air pressure due to wind on 2d freak waves in finite depth." *European Journal of Mechanics-B/Fluids*, 30(1), 1–11.

APPENDIX: PERMISSION LETTER

From: Ke Liu [mailto:kliu14@lsu.edu]
Sent: Thursday, April 28, 2016 11:29 AM
To: PERMISSIONS <permissions@asce.org>
Subject: request for copyright permission

Dear Sir/Lady,

I am a Ph.D. student at Louisiana State University, and I am writing to ask the copyright permission to use one paper that was published in the Journal of Waterway, Port, Coastal and Ocean Engineering for my degree dissertation. Specifically, I need a letter that provides permissions according to the dissertation manual: "All previously copyright material included in the document must be web viewable and permission to use the material on the web must be included in the letter of permission."

The published paper is:

Liu, K., Chen, Q., and Kaihatu, J. (2015). "Modeling Wind Effects on Shallow Water Waves." *J. Waterway, Port, Coastal, Ocean Eng.*, 10.1061/(ASCE)WW.1943-5460.0000314, 04015012.

An acknowledgement of the ASCE will be explicitly stated in my dissertation.

Thank you!

Ke Liu

Coastal Engineering Laboratory,
Dept. Civil and Environmental Engineering,
Louisiana State University,
Baton Rouge, LA 70803

From: PERMISSIONS <permissions@asce.org>
Sent: Thursday, April 28, 2016 10:31:18 AM
To: Ke Liu
Subject: RE: request for copyright permission

Dear Ke Liu:

Thank you for your permission request. Permission is granted for you to reuse your paper "Modeling Wind Effects on Shallow Water Waves." in your dissertation, under the condition that the paper makes up less than 25% of your new work.

A full credit line must be added to the material being reprinted. For reuse in non-ASCE publications, add the words "With permission from ASCE" to your source citation. For Intranet posting, add the following additional notice: "This material may be downloaded for personal use only. Any other use requires prior permission of the American Society of Civil Engineers."

Each license is unique, covering only the terms and conditions specified in it. Even if you have obtained a license for certain ASCE copyrighted content, you will need to obtain another license if you plan to reuse that content outside the terms of the existing license. For example: If you already have a license to reuse a figure in a journal, you still need a new license to use the same figure in a magazine. You need separate license for each edition.

Authors may post the final draft of their work on open, unrestricted Internet sites or deposit it in an institutional repository when the draft contains a link to the bibliographic record of the published version in the ASCE Library or Civil Engineering Database. "Final draft" means the version submitted to ASCE after peer review and prior to copyediting or other ASCE production activities; it does not include the copyedited version, the page proof, or a PDF of the published version.

For more information on how an author may reuse their own material, please view:
http://ascelibrary.org/page/informationforasceauthorsreusingyourownmaterial

Regards,

Joann

Joann Fogleson
Manager, Product and Subscription Services
American Society of Civil Engineers
1801 Alexander Bell Drive
Reston, VA 20191

PERMISSIONS@asce.org

703-295-6112

E-mail: jfogleson@asce.org

Internet: www.asce.org/pubs | www.ascelibrary.org | http://ascelibrary.org/page/rightsrequests

VITA

Ke Liu came from Loudi in Hunan Province, China. In the fall of 2004, he was enrolled into Sichuan University, located in Chengdu, China. He received his Bachelor in Biomedical Engineering in 2008. Thereafter, he worked as a data engineer and studied computational mathematics. As his interests in modeling grew, he determined to pursue a higher degree in numerical modeling and entered the Ph.D. program in engineering science in the College of Engineering at Louisiana State University in the fall of 2010. In the past six years, he was devoted to the study of nearshore hydrodynamics, wave mechanics, and sediment transport. He developed a modeling system for the hurricane-induced sediment transport on Louisiana coast and investigated the sediment redistribution during Hurricane Gustav (2008). He has published two peer-reviewed papers and has another in preparation now. Presently, he is a candidate for the degree of Doctor of Philosophy at Louisiana State University.